
Theses and Dissertations

Spring 2017

Development and evaluation of a nanometer-scale hemocompatible and antithrombotic coating technology for commercially available intracranial stents and flow diverters

Anna Louise Schumacher
University of Iowa

Follow this and additional works at: <https://ir.uiowa.edu/etd>



Part of the [Biomedical Engineering and Bioengineering Commons](#)

Copyright © 2017 Anna Louise Schumacher

This dissertation is available at Iowa Research Online: <https://ir.uiowa.edu/etd/6851>

Recommended Citation

Schumacher, Anna Louise. "Development and evaluation of a nanometer-scale hemocompatible and antithrombotic coating technology for commercially available intracranial stents and flow diverters." PhD (Doctor of Philosophy) thesis, University of Iowa, 2017.

<https://doi.org/10.17077/etd.50a0-roi2>

Follow this and additional works at: <https://ir.uiowa.edu/etd>



Part of the [Biomedical Engineering and Bioengineering Commons](#)

**DEVELOPMENT AND EVALUATION OF A NANOMETER-SCALE
HEMOCOMPATIBLE AND ANTITHROMBOTIC COATING TECHNOLOGY
FOR COMMERCIALLY AVAILABLE INTRACRANIAL STENTS AND FLOW
DIVERTERS**

by

Anna Louise Schumacher

A thesis submitted in partial fulfillment
of the requirements for the Doctor of Philosophy
degree in Biomedical Engineering in the
Graduate College of
The University of Iowa
May 2017

Thesis Supervisors: Professor M.L. Raghavan
Associate Professor David M. Hasan

Copyright by

ANNA LOUISE SCHUMACHER

2017

All Rights Reserved

Graduate College
The University of Iowa
Iowa City, Iowa

CERTIFICATE OF APPROVAL

PH.D. THESIS

This is to certify that the Ph.D. thesis of

Anna Louise Schumacher

has been approved by the Examining Committee for
the thesis requirement for the Doctor of Philosophy degree
in Biomedical Engineering at the May 2017 graduation.

Thesis Committee:

M.L. Raghavan, Thesis Supervisor

David M. Hasan, Thesis Supervisor

Ned B. Bowden

Aliasger K. Salem

Aju S. Jugessur

*To my parents, who taught me that no dream is too big –
To Tyler – who has walked on the road less traveled with me and not looked back.*

Two roads diverged in a yellow wood,
And sorry I could not travel both
And be one traveler, long I stood
And looked down one as far I could
To where it bent in the undergrowth;

Then took the other, as just as fair,
And having perhaps the better claim,
Because it was grassy and wanted wear;
Though as for that the passing there
Had worn them really about the same,

And both that morning equally lay
In leaves no step had trodden black.
Oh, I kept the first for another day!
Yet knowing how way leads on to way,
I doubted if I should ever come back.

I shall be telling this with a sigh
Somewhere ages and ages hence;
Two roads diverged in a wood, and I –
I took the one less traveled by,
And that has made all the difference.

Robert Frost
The Road Not Taken

ACKNOWLEDGEMENTS

I would like to thank my Ph.D. advisors Dr. M.L. Raghavan and Dr. David Hasan for your combined guidance and support – thank you for offering me a great chance, as well as honing my development as a research scientist and engineer. I feel very blessed and honored to have been mentored by you both.

I would also like to thank my committee members. Each of you has contributed significantly to this work – thank you for the many discussions, insights, and ideas. This work is the culmination of all these things – thank you for your collaboration and enthusiasm.

Thank you to Chad Gilmer for your expertise and insight. I owe much to the early mornings and late nights we spent coating devices and discussing the project in the chemistry lab – thank you for your unwavering enthusiasm. Additionally, thank you to Keerthi Atluri for your insights in the project, shared through many long discussions, and for your help in the development of not only the CAT assay, but also the in-vitro Modified Chandler Loop. This work was truly a team effort and could not have been accomplished without your individual help. I feel blessed to have spent so much time in the company of such brilliant scientists and friends.

Thank you to Dr. Howard Dittrich, Co-Founder and President of Advanced Endovascular Therapeutics Inc., for your tireless support of this technology and for your mentorship – it has been a true blessing. Thank you to Dr. Joun Lee, Chemical Research Engineer at the University of Iowa, for your expertise in the acquisition and analysis of the XPS data reported herein, and for the countless hours you spent mentoring me on these aspects – I will be forever grateful for your help, kindness, and friendship.

Thank you to the University of Iowa Central Microscopy Research Facility for the training and support I received on the Hitachi S-4800 SEM instrument, the SP8 STED Super Resolution Microscope for confocal imaging, and the Kratos Axis Ultra XPS instrument. Thank you to the University of Iowa Optical Science and Technology Center for the training I received on the PE-ALD, ellipsometer, and the CNC wafer dicer. Thank you to the Salem and Bowden labs for use of your lab spaces throughout this project.

I would also like to thank Dr. Alexander Mukasyan, Professor of Chemical Engineering and Director of the Laboratory of Advanced Electron Microscopy at the University of Notre Dame, for your help in the acquisition of the FIB/SEM images of the aluminum oxide coated flow diverter. Thank you to Dr. John Widness, Physician and Professor of Pediatrics and Neonatology at the University of Iowa, and the Widness Lab for use of your Sysmex XE-2100 Human Blood Cell Counter and for the scheduling flexibility. Thank you to Dr. Steven Lentz, Dr. Sanjana Dayal, and Sean Gu, M.D./Ph.D. student in the Lentz Lab, for your shared insight into human coagulation and for your help with the Activated Protein C assay. I would also like to thank Dr. Monica Hinds and the Oregon National Primate Research Center for your help with the ex-vivo primate shunt experiments. Finally thank you to Dr. Ryan Dorfman and Dr. Ashley McLaren at Haematologic Technologies Inc. for your shared expertise and help in adapting the in-house CAT assay protocol for your facility, and for performing CAT assay testing of flow diverters coated with our technology therein. Thank you to Dr. Rick Haasch at the University of Illinois at Urbana-Champaign Materials Research Lab for acquiring some XPS data on coated silicon wafers and flow diverting devices when our Kratos XPS instrument was broken.

Thank you to my fellow BioMOST lab members for your friendship and support. I owe much to my growth as a research scientist and engineer to the many hours spent discussing physics theories and biomedical device design in the lab. I will forever cherish my time spent in graduate school in the company of such talented engineers and great friends.

Finally thank you to my parents for teaching me that no dream is too big – to you my deepest gratitude goes. I would also like to thank my husband Tyler for your enthusiasm and support of this journey – there is no one I would rather continue my walk on the road less traveled with.

ABSTRACT

An intracranial aneurysm is a local dilation of an artery in the cerebral circulation. While the etiology of intracranial aneurysms is unknown, they likely result from a combination of factors including the weakening and degeneration of the collagen fibers and the internal elastic lamina comprising the arterial wall, as well as hemodynamic-associated stress resulting from blood pulsation inside the aneurysm sac. Intracranial aneurysm rupture leads to a devastating sequela, as 50% of patients die. In the U.S. alone there are approximately 30,000 cases of subarachnoid hemorrhage annually, a prevalence which has pushed practitioners to aggressively treat the aneurysm disease. Traditionally, intracranial aneurysms were managed with open craniotomy and microsurgical clipping; however, these treatment modalities carry relatively high morbidity and mortality depending upon the aneurysm location and surgical experience. In 2002 the International Subarachnoid Hemorrhage Aneurysm Trial established the superiority of the endovascular coiling of intracranial aneurysms compared to microsurgical clipping. This trial led to a paradigm shift in treating intracranial aneurysms with marked use of intracranial stenting, including devices used to assist endovascular coiling and stand-alone flow diverting devices. However, the placement of intracranial devices in the cerebral circulation mandates the adjunctive application of dual anti-platelet pharmaceuticals to minimize thromboembolic events, despite being associated with increased patient risk. This dissertation proposes a novel multilayer, nanometer-scale coating technology suitable for commercially available intracranial stents and flow diverting devices to minimize the use of dual anti-platelet therapy in the elective setting and expand the use of intracranial devices in the acute setting of ruptured intracranial aneurysms. A combination of qualitative and quantitative chemical characterization techniques was used to assess the composition, uniformity, and thickness of each coating layer on commercially available flow diverting devices; overall the coating was found to be relatively uniform and conformal to the device wires. Furthermore, in-vitro and in-vivo testing on commercially available intracranial devices suggest some hemocompatible and antithrombotic properties. Finally, the proposed coating technology can be modified for use as a platform for the attachment of FDA-approved molecules. With further optimization and testing this technology has the potential to minimize the adjunctive use of dual-antiplatelet therapy in the endovascular treatment of intracranial aneurysms.

PUBLIC ABSTRACT

An intracranial aneurysm is a local dilation of a blood vessel in the brain. While the etiology of intracranial aneurysms is unknown, they likely result from a combination of factors including the weakening of structural components within the blood vessel wall, as well as stress resulting from blood pulsation inside the dilated aneurysm sac. The problem with intracranial aneurysms is they can rupture, leading to hemorrhage, brain damage, and death. Approximately 30,000 cases of intracranial aneurysm rupture occur annually in the U.S. However, there is no FDA-approved device to treat these brain bleeds since all current devices require the concurrent use of blood-thinning medications, which will only exacerbate the bleeding in these patients. Furthermore, patients with unruptured intracranial aneurysms that can be treated with current medical devices are required to take blood-thinning medications long-term, a risky pharmaceutical regimen that is not always well-tolerated. This dissertation proposes a biomaterial coating suitable for commercially available brain medical devices that helps make their surfaces less reactive in the body, the goal being to lessen or else eliminate the need for concurrent blood-thinning medications. Such a coating technology would give ruptured aneurysm patients an additional mode of treatment and lessen the current treatment risk for unruptured aneurysm patients. In addition to proposing a novel chemical formulation for a biocompatible coating, this dissertation evaluates the proposed technology through benchtop and animal tests; finally, the adaptability of the technology to incorporate FDA-approved molecules in its blood contacting layer and its performance thereafter was assessed by benchtop tests. The proposed technology was found to be a promising coating for commercially available brain medical devices, with some demonstrated increase in coated device biocompatibility.

TABLE OF CONTENTS

LIST OF TABLES.....	xi
LIST OF FIGURES	xii
Chapter 1	1
Intracranial Aneurysms and Their Endovascular Treatment	1
Motivation for Developing an Antithrombotic Intracranial Device Coating.....	3
A Review of Hemocompatible Surface Modification and Coating Strategies for Intravascular Stents ³²	6
Introduction.....	6
Surface Modifications	6
Passive Inorganic Coatings	7
Bioactive Coatings.....	8
Micro- and Nano-Structured Surfaces.....	9
Summary	9
Objectives.....	11
Chapter 2	13
Specific Aim #1: Development of the Nanometer-Scale Hemocompatible and Antithrombotic Coating Chemistry and Deposition Technique Suitable for Commercially Available Intracranial Devices	13
Coating Chemistry and Deposition Technique	16
Chapter 3	24
Specific Aim #2: Characterize the Developed Coating Chemistry and Assess its Hemocompatible and Antithrombotic Functionality	24
Characterization of the Al ₂ O ₃ Layer.....	24
Characterization of the APTES Layer	32
Characterization of the TCT Layer	34
Characterization of the hTM Layer	36
In-vitro Assessment of Hemocompatibility and Antithrombotic Functionality	40
The Coagulation Cascade.....	41
The Calibrated Automated Thrombogram (CAT) In-Vitro Assay	46
In-Vitro CAT Assay Assessment of Coating Technology Thrombogenicity.....	49

Third-Party In-Vitro Assessment of Coating Technology Thrombogenicity	58
In-Vitro Evaluation of Coating Technology Shelf Life	61
In-Vivo Survival Study in a Porcine Model	69
Ex-Vivo Evaluation of Coating Technology Thrombogenicity in a Primate Shunt Model.....	71
Chapter 4	75
Specific Aim #3: Develop and Evaluate the Coating Technology as a Platform for the Attachment of FDA-Approved Molecules	75
Development of the Coating Technology as a Platform for the Attachment of Heparin ..	77
Heparin Attachment in MES Buffer and Characterization by XPS	78
Heparin Attachment in Sodium Carbonate-Sodium Bicarbonate Buffer and Characterization by XPS	83
Development of the Coating Technology as a Platform for the Attachment of Phosphorylcholine (PC).....	87
o-PA Attachment in Citric Acid and Characterization via XPS	88
o-PA Attachment in a Sodium Bicarbonate Buffer and Characterization via XPS	90
o-PA Attachment via a Modified Coupling Protocol and Associated XPS Characterization	91
o-PA Attachment in DI Water and Characterization by XPS	93
Development of the Coating Technology as a Platform for the Attachment of Methoxy-poly(ethylene glycol) (mPEG).....	98
mPEG Attachment in Methanol and Characterization by XPS	99
mPEG Attachment in Deionized (DI) Water and Characterization by XPS	101
Third-Party In-Vitro Thrombogenicity Assessment of the Coating Technology as a Platform for the Attachment of FDA-approved Molecules	109
Chapter 5	115
Failed Experiments.....	115
The Protein C Activation Assay: A Static In-Vitro Thrombogenicity Test	115
The Modified Chandler Loop: A Dynamic In-Vitro Thrombogenicity Test	119
Static In-Vitro Platelet Adhesion: A Method for Qualitative Assessment.....	122
Chapter 6	132
Discussion	132
Conclusion.....	140

References	141
Appendix A.....	150
Methodology for Evaluating Intracranial Flow Diverting Device Stiffness: Uniaxial Extension.....	150
Methodology for Computing Intracranial Device-Associated Friction in Microsheath ...	152

LIST OF TABLES

Table 1: Summary of Intravascular Stent Surface Modification and Coating Strategies. ...	10
Table 2: Shelf life study blood donor demographic Information and associated platelet-rich plasma (PRP) platelet counts.....	63

LIST OF FIGURES

Figure 1: (A) Schematic of an intracranial stent used for stent-assisted coiling of an intracranial aneurysm (from www.neurosurgery-blog.com) (B) Schematic of a flow diverting device used to treat an intracranial aneurysm (from www.europapress.es).....	2
Figure 2: Schematic illustration of the developed hemocompatible and antithrombotic coating technology for intracranial devices.	14
Figure 3: The key design attributes of the developed coating chemistry and deposition technique for intracranial devices.	15
Figure 4: (A) SEM image of commercial flow diverting device #1 prior to ultrasonic cleaning with the established protocol. (B) The same device after ultrasonic cleaning....	20
Figure 5: Schematic of the APTES silanization chemical reaction used to functionalize the PE-ALD deposited Al_2O_3 layer on a stent or flow diverter device.	21
Figure 6: Schematic of the TCT coupler chemical reaction used to functionalize the APTES layer on a stent or flow diverter device.	21
Figure 7: Schematic of the hTM protein reaction that couples to the TCT layer on a stent or flow diverter device.	22
Figure 8: A schematic of the structure of human thrombomodulin (hTM), originally printed in Suzuki et al. ⁴⁹	22
Figure 9: (A) SEM image of an uncoated commercial flow diverting device #1. (B) SEM image of a commercial flow diverting device #1 coated with 300 cycles of PE-ALD deposited Al_2O_3	25
Figure 10: (A) Schematic of the flow diverting device #1 orientation on the SEM stage during image acquisition. (B) Acquired SEM image of an uncoated commercial flow diverting device #1. (C) Acquired SEM image of a commercial flow diverting	

device #1 spray coated with PLGA 50:50 in DCM (2% w/v solution), with glycerol and PEG 200 as surfactants.	26
Figure 11: The acquired XPS survey scan on an uncoated commercial flow diverting device #1.	28
Figure 12: The XPS elemental intensity maps acquired for the component metals of an uncoated commercial flow diverting device #1.	29
Figure 13: The acquired XPS survey scan on a commercial flow diverting device #1 coated with 300 cycles of PE-ALD deposited Al ₂ O ₃	30
Figure 14: The XPS elemental intensity maps acquired for a flow diverting device #1 coated with 300 cycles of PE-ALD deposited Al ₂ O ₃	30
Figure 15: (A) SEM image of the FIB rectangular etch on a single wire of a commercial flow diverting device #2 coated with 300 cycles of PE-ALD deposited Al ₂ O ₃ and platinum (Pt), the white box denotes the approximate location of the SEM cross-sectional image shown to the right. (B) SEM cross-sectional image of a portion of the FIB etch.	31
Figure 16: The acquired XPS survey scan on a commercial flow diverting device #1 coated with 300 cycles of PE-ALD deposited Al ₂ O ₃ and the silane APTES.	33
Figure 17: The XPS elemental intensity maps acquired for a commercial flow diverting device #1 coated with 300 cycles of PE-ALD deposited Al ₂ O ₃ and the silane APTES.	33
Figure 18: The acquired XPS survey scan on a commercial flow diverting device #1 coated with 300 cycles of PE-ALD deposited Al ₂ O ₃ , the silane APTES, and the TCT coupler.	34
Figure 19: The XPS elemental intensity maps acquired for a commercial flow diverting device #1 coated with 300 cycles of PE-ALD deposited Al ₂ O ₃ , the silane APTES, and the TCT coupler.	35

Figure 20: (A) SEM image of a commercial flow diverting device #5 coated with 300 cycles of PE-ALD deposited Al₂O₃, the silane APTES, and the TCT coupler at 400X magnification. (B) The same device imaged at 1000X magnification. 36

Figure 21: The acquired XPS survey scan on a commercial flow diverting device #1 coated with 300 cycles PE-ALD deposited Al₂O₃, the silane APTES, the coupler TCT, and the bioactive hTM..... 37

Figure 22: (A) The acquired XPS core level scan for nitrogen taken on a commercial flow diverting device #1 coated with 300 cycles PE-ALD deposited Al₂O₃, the silane APTES, the coupler TCT, and the bioactive hTM. (B) The acquired XPS core level scan for nitrogen taken on a commercial flow diverting device #1 coated with 300 cycles PE-ALD deposited Al₂O₃, the silane APTES, and the coupler TCT. 38

Figure 23: Confocal images (all at 10X magnification) of the (A) exterior and (B) interior of a TCT coated commercial flow diverting device #1. (C) The exterior and (D) interior of a hTM coated #1 flow diverting device. (E) The autofluorescent capability of an uncoated #1 device. 39

Figure 24: Thrombin generation scheme originally printed in Hemker and Beguin.¹⁷ Lines with open arrow heads indicate a chemical conversion; lines with black arrow heads indicate activation of a proenzyme; dotted lines with open arrow heads indicate an activating action and dotted lines with black arrow heads indicate an inhibitory action..... 41

Figure 25: The coagulation cascade. Green lines depict the thrombin’s roles as a reaction catalyst. Red lines depict the primary regulatory mechanisms that keep coagulation in check. Figure attributed to Wikimedia Commons and distributed under a CC-BY 3.0 License. 43

Figure 26: Thrombin generation time course in recalcified, activated plasma. Four major parameters are identified. Peak Height refers to peak thrombin concentration. Figure attributed to Berry and Chan’s book Haemostasis: Methods and Protocols.⁷¹ 47

Figure 27: Constituents of the 96-well plate run in the in-house CAT assay. LLDPE refers to Linear Low-Density Polyethylene; hTM refers to the human recombinant thrombomodulin purchased from Sigma-Aldrich; TCT stent refers to device coated with every layer in the developed coating technology except the hTM layer; hTM stent refers to a device coated with every layer. 51

Figure 28: An example of the organization of the raw fluorescent signal intensity data outputted from the SpectraMax M5 fluorometer..... 53

Figure 29: An example of the organization of the raw fluorescent signal intensity data required for CAT assay data analysis..... 53

Figure 30: Comparison plot between the known and computed thrombin calibrator concentrations used in the in-house CAT assay. The thrombin calibrator concentrations were computed via the data analysis method outlined by Hemker and Kremers.⁶⁹ 55

Figure 31: The average free thrombin generation time-courses, or thrombograms, associated with the unknown samples run in the in-house CAT assay..... 57

Figure 32: The peak thrombin concentration associated with the thrombogram of each sample run in the in-house CAT assay..... 58

Figure 33: The peak thrombin concentration associated with the thrombogram of each sample tested by a third-party commercial vendor. The hTM coated commercial flow diverting device #1 in this test was shipped on ice. 59

Figure 34: The peak thrombin concentration associated with the thrombogram of each sample tested by the third-party commercial vendor, relative to a similar flow diverting device coated with a competitive technology. The hTM and hTM+APC coated commercial #1 flow diverting devices in this test were shipped at room temperature..... 60

Figure 35: The peak thrombin concentration associated with the thrombogram of each sample tested by the third-party commercial vendor. The TCT coated commercial #1 flow diverting devices in this test were shipped at room temperature.... 61

Figure 36: (A) A highly undulated free thrombin concentration integral for a bare commercial flow diverting device #3 piece, and respective Hemker model fit, observed for Time 0 of the shelf life study. (B) A moderately undulated free thrombin concentration integral for a hTM coated commercial flow diverting device #3 piece, and respective Hemker model fit, also observed for Time 0 of the shelf life study. 64

Figure 37: Comparison plot between the peak thrombin concentration computed by numerical differentiation and by the 2013 Hemker et al. model in the shelf life study.... 66

Figure 38: The peak thrombin concentrations computed via the Hemker et al. 2013 model⁶⁹ for (A) each sample tested in the shelf life CAT assay performed immediately post coating (Time 0), (B) each sample tested in the shelf life CAT assay performed one week post coating, (C) each sample tested in the shelf life CAT assay performed two weeks post coating, (D) each sample tested in the shelf life CAT assay performed five weeks post coating, (E) each sample tested in the shelf life CAT assay performed eight weeks post coating, and (F) each sample tested in the shelf life CAT assay performed 33 weeks post coating..... 68

Figure 39: Figure 8: (A) Fibrin accumulation for each commercial flow diverting device #2 deployed in a primate AV shunt for an hour long perfusion period. The black circles indicate the fibrin accumulation for each individual device, while the gray bars indicate the average. (B) Fibrin accumulation for each commercial flow diverting device #5 deployed in a different primate AV shunt for a 45-minute perfusion period. The black circles indicate the fibrin accumulation for each individual device, while the gray bars indicate the average. (C) The corresponding average platelet accumulation for each #2 device deployed in the primate shunt and shown in panel A. (D) The corresponding average platelet accumulation for each #5 device deployed in the primate shunt and shown in panel B..... 73

Figure 40: A schematic of how heparin binds to the silane APTES layer in the developed coating technology.	78
Figure 41: The acquired XPS survey scan on a 1 cm x 1 cm p-doped silicon wafer coated with 300 cycles PE-ALD deposited Al ₂ O ₃ , the silane APTES, and heparin with the coupling reaction done in MES buffer.	79
Figure 42: The acquired XPS survey scan on a 1 cm x 1 cm p-doped silicon wafer coated with 300 cycles PE-ALD deposited Al ₂ O ₃ and the silane APTES.....	80
Figure 43: (A) The acquired XPS core level scan for nitrogen taken on a 1 cm x 1 cm p-doped silicon wafer coated with 300 cycles PE-ALD deposited Al ₂ O ₃ , the silane APTES, and heparin with the coupling reaction done in MES buffer. (B) The acquired XPS core level scan for nitrogen taken on a 1 cm x 1 cm p-doped silicon wafer coated with 300 cycles PE-ALD deposited Al ₂ O ₃ and the silane APTES.....	81
Figure 44: (A) The acquired XPS survey scan on a commercial flow diverting device #5 piece coated with 300 cycles PE-ALD deposited Al ₂ O ₃ , the silane APTES, and heparin with the coupling reaction done in MES buffer. (B) The acquired XPS core level scan for nitrogen on the same device.	82
Figure 45: The acquired XPS survey scan on a 1 cm x 1 cm p-doped silicon wafer coated with 300 cycles PE-ALD deposited Al ₂ O ₃ , the silane APTES, and heparin with the coupling reaction done in sodium carbonate-sodium bicarbonate buffer.....	84
Figure 46: The acquired XPS core level scan for nitrogen taken on a 1 cm x 1 cm p-doped silicon wafer coated with 300 cycles PE-ALD deposited Al ₂ O ₃ , the silane APTES, and heparin with the coupling reaction done in sodium carbonate-sodium bicarbonate buffer.....	85
Figure 47: (A) The acquired XPS survey scan on a commercial flow diverting device #5 piece coated with 300 cycles PE-ALD deposited Al ₂ O ₃ , the silane APTES, and heparin with the coupling reaction done in sodium carbonate-bicarbonate buffer. (B) The acquired XPS core level scan for nitrogen on the same device.	86

Figure 48: The acquired XPS survey scan on a bare commercial flow diverting #5 device.....	87
Figure 49: The acquired XPS survey scan on a 1 cm x 1 cm p-doped silicon wafer coated with 300 cycles PE-ALD deposited Al ₂ O ₃ , the silane APTES, the coupler TCT, and o-PA with the coupling reaction done in citric acid buffer.....	89
Figure 50: The acquired XPS survey scan on a 1 cm x 1 cm p-doped silicon wafer coated with 300 cycles PE-ALD deposited Al ₂ O ₃ , the silane APTES, the coupler TCT, and o-PA with the coupling reaction done in a sodium bicarbonate buffer.....	91
Figure 51: The acquired XPS survey scan on a 1 cm x 1 cm p-doped silicon wafer coated with 300 cycles PE-ALD deposited Al ₂ O ₃ , the silane APTES, and o-PA with the coupling reaction done in a MES buffer.....	92
Figure 52: The acquired XPS survey scan on a 1 cm x 1 cm p-doped silicon wafer coated with 300 cycles PE-ALD deposited Al ₂ O ₃ , the silane APTES, the coupler TCT, and o-PA with the coupling reaction done in deionized water.....	94
Figure 53: The acquired XPS core level scan for phosphorus taken on a 1 cm x 1 cm p-doped silicon wafer coated with 300 cycles PE-ALD deposited Al ₂ O ₃ , the silane APTES, the coupler TCT, and o-PA with the coupling reaction done in deionized water..	95
Figure 54: A schematic of how o-PA binds to the coupler TCT layer in the developed coating technology.	95
Figure 55: The acquired XPS survey scan on a commercial flow diverting device #5 piece coated with 300 cycles PE-ALD deposited Al ₂ O ₃ , the silane APTES, the coupler TCT, and o-PA with the coupling reaction done in deionized water.....	96
Figure 56: (A) The acquired XPS core level scan for nitrogen on a commercial flow diverting device #5 piece coated with 300 cycles PE-ALD deposited Al ₂ O ₃ , the silane APTES, the coupler TCT, and o-PA with the coupling reaction done in deionized water. (B) The acquired XPS core level scan for nitrogen on a commercial flow diverting	

device #5 piece coated with 300 cycles PE-ALD deposited Al ₂ O ₃ , the silane APTES, and the coupler TCT.	97
Figure 57: (A) The acquired XPS survey scan on a 1 cm x 1 cm p-doped silicon wafer coated with 300 cycles PE-ALD deposited Al ₂ O ₃ , the silane APTES, the coupler TCT and mPEG with average molecular weight of 5000 dissolved in methanol at 10 mg/mL. (B) The acquired XPS survey scan on a 1 cm x 1 cm p-doped silicon wafer coated with 300 cycles PE-ALD deposited Al ₂ O ₃ , the silane APTES, and the coupler TCT.	100
Figure 58: (A) The acquired XPS survey scan on a commercial flow diverting device #5 piece coated with 300 cycles PE-ALD deposited Al ₂ O ₃ , the silane APTES, the coupler TCT, and mPEG with average molecular weight of 13000 dissolved in deionized water at 60 mg/mL. (B) The acquired XPS survey scan on a flow diverting device #5 piece coated with 300 cycles PE-ALD deposited Al ₂ O ₃ , the silane APTES, and the coupler TCT.	102
Figure 59: (A) The acquired XPS core level scan for nitrogen on a commercial flow diverting device #5 piece coated with 300 cycles PE-ALD deposited Al ₂ O ₃ , the silane APTES, the coupler TCT, and mPEG with average molecular weight of 13000 dissolved in deionized water at 60 mg/mL. (B) The acquired XPS core level scan for nitrogen on a commercial flow diverting device #5 piece coated with 300 cycles PE-ALD deposited Al ₂ O ₃ , the silane APTES, and the coupler TCT.	104
Figure 60: (A)The acquired XPS survey scan on a commercial flow diverting device #5 piece coated with 300 cycles PE-ALD deposited Al ₂ O ₃ , the silane APTES, the coupler TCT, and mPEG with average molecular weight of 13000 dissolved in deionized water at 100 mg/mL. (B) The acquired XPS survey scan on a commercial flow diverting device #5 piece coated with 300 cycles PE-ALD deposited Al ₂ O ₃ , the silane APTES, and the coupler TCT.	106
Figure 61: (A) The acquired XPS core level scan for nitrogen on a commercial flow diverting device #5 piece coated with 300 cycles PE-ALD deposited Al ₂ O ₃ , the silane	

APTES, the coupler TCT, and mPEG with average molecular weight of 13000 dissolved in deionized water at 100 mg/mL. (B) The acquired XPS core level scan for nitrogen on a commercial flow diverting device #5 piece coated with 300 cycles PE-ALD deposited Al₂O₃, the silane APTES, and the coupler TCT. 108

Figure 62: A schematic of how mPEG binds to the coupler TCT layer of the developed coating technology. 109

Figure 63: The peak thrombin concentration associated with the thrombogram of each sample tested in the preliminary CAT assay by Haematologic Technologies Inc. three days post coating deposition. 111

Figure 64: The peak thrombin concentration associated with the thrombogram of each sample tested in the preliminary CAT assay by Haematologic Technologies Inc. one week post coating deposition. 112

Figure 65: The peak thrombin concentration associated with the thrombogram of each developed coating chemistry platform in the CAT assay by Haematologic Technologies Inc. three days post coating deposition..... 113

Figure 66: The regenerated absorbance versus time raw data for the bare and hTM coated commercial stent-assisted coiling #6 devices tested in the Activated Protein C assay. The raw data was regenerated using the recorded absorbance rates over the measurement time period, due to difficulty experienced in exporting the raw data from the microplate reader. 117

Figure 67: The hTM standard curve associate with the Activated Protein C assay. The measured absorbance rates for the bare and hTM coated commercial stent-assisted coiling #6 devices were linearly interpolated on this curve to determine the amount of active hTM conjugated to the coated devices. 118

Figure 68: The Modified Chandler Loop as described by Tepe et al.¹⁰⁷ 119

Figure 69: A multifunctional wheel designed in PTC Creo® to hold a Modified Chandler Loop, close it, and connect it to a motor shaft. The interior hole is

designed to fit the motor shaft, while the flange on top provides both radial and longitudinal compression to close the tubing ends.....	120
Figure 70: Photo of the Modified Chandler Loop built in-house at the University of Iowa.....	121
Figure 71: Platelet fragments observed by SEM on a bare, p-doped silicon wafer sample incubated for one hour in static human blood plasma containing approximately 1.03×10^8 platelets. No intact platelets were observed on this wafer sample, nor were they observed on any of the other coated or glass wafers tested in this platelet incubation experiment.	125
Figure 72: (A) SEM image of adhered platelets, observed on a bare, p-doped silicon wafer sample incubated for 2.5 hours in 100 μ L of static human blood plasma containing approximately 4.7×10^6 platelets. (B) SEM image of adhered platelets observed on a second bare, p-doped silicon wafer also incubated for 2.5 hours in 100 μ L of static human blood plasma containing approximately 4.7×10^6 platelets.	127
Figure 73: (A) SEM image of adhered platelets, observed on a bare, p-doped silicon wafer sample incubated for 3 hours in 100 μ L of static human blood plasma containing approximately 5.4×10^6 platelets. (B) SEM image of adhered platelets, observed on a bare, p-doped silicon wafer sample incubated for 3 hours in 1 mL of static human blood plasma containing approximately 0.54×10^8 platelets. (C) SEM image of adhered platelets, characteristic of those observed on bare, p-doped silicon wafers incubated for 2 hours in 100 μ L of static human blood plasma containing approximately 2.2×10^6 platelets.....	129
Figure 74: Representative SEM image of a bare commercial flow diverting device #1 wire. A device piece approximately 4.75 x 4 mm in size was incubated for three hours in 140 μ L static human blood plasma containing approximately 3.9×10^6 platelets. Neither intact platelets nor platelet fragments were observed on this device.	131

Figure A1: A commercial flow diverting device #1 clamped in the MTS uniaxial extension tester 151

Figure A2: The force-device diameter data from a commercial flow diverting device #1 stretched by approximately 170% in the MTS extension tester (n=3, Initial Test1-Test3) then re-positioned in the clamps and stretched by approximately 170% again (n=3, Moved Test1-Test3). The force-diameter data from the same device first compressed from an initial zero position and then stretched by the MTS extension tester (n=3, CompExt Initial Test1-Test3) and re-positioned in the clamps, compressed, then stretched is also shown (n=3, CompExt Moved Test1-Test3) 152

Figure A3: The configuration of the commercial microsheaths used in assessing the MTS extension tester load cell sensitivity. Configuration 1 allows for the device to be pulled through a single bend in the sheath. Configuration 2 allows for the device to be pulled through a highly tortuous sheath. Configuration 3 allows for the device to be pulled through a straight sheath. The device is pulled a total of six inches in all configurations. 153

Figure A4: The force-machine extension data associated with pulling a commercial flow diverting device #2 through six inches of each of the three microsheat configurations shown in Figure A3. Data for pulling the device at slow (0.5 mm/s), medium (4 mm/s), and fast (16 mm/s) speeds is shown. 154

PREFACE

The technology discussed herein is protected through a pending nonprovisional patent. Advanced Endovascular Therapeutics, Incorporated (AET) has been formed around this intellectual property; the author possess equity in AET.

CHAPTER 1

Intracranial Aneurysms and Their Endovascular Treatment

An intracranial aneurysm is a local dilation of a blood vessel in the brain.¹ While the etiology of intracranial aneurysms is unknown, they likely result from a combination of factors including the weakening and degeneration of the collagen fibers and the internal elastic lamina of the arterial wall, as well as hemodynamic-associated stress resulting from blood pulsation inside the aneurysm sac.¹ The problem with intracranial aneurysms is that they can rupture, leading to subarachnoid hemorrhage (SAH), brain damage, and death (in approximately 50% of patients).² Approximately 30,000 cases of SAH occur annually in the U.S.¹

Since the early 1990s there has been a push to treat intracranial aneurysms with endovascular methods and devices as a result of the devastating outcome of SAH.³ The traditional treatment modality for intracranial aneurysms, called microsurgical clipping, involves performing a craniotomy on the patient and placing a metal clip across the aneurysm neck in an effort to isolate it from the rest of the cerebral circulation.³ However, in 2002 the International Subarachnoid Hemorrhage Aneurysm Trial (ISAT) showed superiority of endovascular coiling of intracranial aneurysms compared to microsurgical clipping.⁴ This trial has changed the paradigm of intracranial aneurysm treatment, and changed the landscape of how these aneurysms are clinically managed; initially, intracranial aneurysms were managed with coiling alone, however, as more complex aneurysms were treated endovascularly, the need for adjunctive devices like intracranial stents and flow diverters has become evident.³

The first intracranial stent to gain FDA approval for use in the U.S. was the Neuroform™ in 2002.⁵ This device is shown in Figure 1A, it is a metallic wire mesh and its design is representative of other intracranial stents on the U.S. market today.

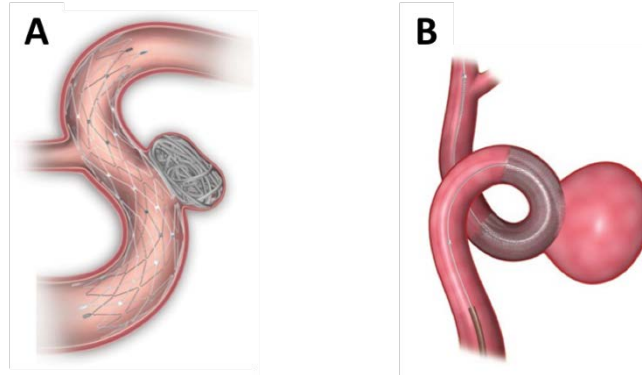


Figure 1: (A) Schematic of an intracranial stent used for stent-assisted coiling of an intracranial aneurysm (from www.neurosurgery-blog.com) (B) Schematic of a flow diverting device used to treat an intracranial aneurysm (from www.europapress.es).

All intracranial stents are deployed from a microcatheter across the neck of the intracranial aneurysm. This catheter is inserted into the patient's femoral artery via a small incision in the groin and is navigated by a neuroradiologist to the intracranial aneurysm, using x-ray angiography, at which time the stent is deployed. Once deployed, these stents expand in place to conform to the inside of the artery. Next a second microcatheter is placed through the intracranial stent wire mesh and into the aneurysm sac. This microcatheter is used to deploy metal coils (or embolization coils) into the aneurysm sac, as shown in Figure 1A. The embolization coils slow incoming blood into the aneurysm, and thereby promote thrombus formation. The resulting coil-clot mass impedes blood flow over time and is therefore thought to protect the aneurysm from rupture.^{6,7} The intracranial stent functions as a rigid barrier to hold the embolic coils within the aneurysm sac; the rigidity is, in part, due to the fact that these devices are laser-cut from solid metal tubes. This entire procedure is known as stent-supported coil embolization. In contrast to intracranial stents are intracranial flow diverting devices, shown in Figure 1B; the first intracranial flow diverting device to gain FDA approval for use in the U.S. was the Pipeline™ device in 2011.⁸ Like intracranial stents, intracranial flow diverting devices are deployed by navigating the associated delivery microcatheter to the neck of the intracranial aneurysm using x-ray angiography; once deployed, the individual wires comprising the device are able to freely move relative to one another, enabling the expansion of the device inside of the artery. Intracranial flow diverting devices are much more mesh-dense than intracranial stents and thereby slow incoming blood into the aneurysm efficiently and without the use of embolization coils, ultimately promoting thrombus formation inside the aneurysm sac. Over time this thrombus

impedes blood flow into the aneurysm sac and is therefore thought to protect the aneurysm from rupture.^{9,10} However both intracranial stents and flow diverting devices are indicated for use only when the anti-platelet drugs aspirin and clopidogrel are systemically administered (known as dual anti-platelet therapy, or DAPT) both pre- and post-device placement.^{5,8} DAPT now constitutes the standard of care for the elective endovascular treatment of intracranial aneurysms despite its association with increased patient risk.¹¹⁻¹³

Motivation for Developing an Antithrombotic Intracranial Device Coating

The primary motivation for developing a hemocompatible and antithrombotic coating for intracranial stents and flow diverting devices is that thromboembolic complications are not insignificant in intracranial aneurysm patients treated endovascularly. Two large multicenter retrospective studies published in the literature indicate that thromboembolic complications occur in 4.7% of intracranial aneurysm patients treated with the Pipeline™ flow diverting device (manufactured by the company Medtronic Inc.) and DAPT,¹⁰ and in 7.1% of patients treated with stent-supported coil embolization and DAPT.⁷ According to the CURE clinical study, combined aspirin and clopidogrel use in patients is associated with an increase in major or life-threatening bleeding events (3.7%) compared to patients taking a placebo and aspirin (2.7%); other bleeding events reported more frequently in patients on DAPT in this study were epistaxis, hematuria, and bruising.¹³ Therefore an antithrombotic coating suitable for intracranial stents and flow diverting devices would at least minimize or at best eliminate the need for endovascularly treated intracranial aneurysm patients to receive DAPT, decreasing or eliminating the associated patient risks. Finally, such a coating would increase intracranial stent indications for use to include patients suffering from acute SAH.

While development of a hemocompatible and antithrombotic coating for intracranial stents and flow diverting devices has many benefits, it is not without challenges. Chief among these challenges is lack of a good deposition technique that still maintains the flexibility of the underlying device. Spraying and dipping techniques for coating deposition, techniques traditionally used to manufacture drug-eluting cardiovascular stents,¹⁴ tend to fill the mesh interstices of intracranial stents and flow diverters and thereby increase overall device stiffness. Increased device stiffness

ultimately hinders intracranial device deployment, since both intracranial stents and flow diverters are required to conform to tortuous cerebral blood vessels; additionally, increased device stiffness facilitates cracking of the surface coating.

A second challenge to the development of a coating for an intracranial device is the in-vitro assessment of the coating's hemocompatibility and thrombogenicity. This is because all the in-vitro coagulation assays reported in the literature and used for clinical screening of coagulation protein defects examine the rate of clot formation.¹⁵ However a clot forms early in the coagulation cascade; therefore the rate of clot formation does not sufficiently describe the dynamic coagulation cascade.¹⁶ Since the coagulation cascade terminates with the generation of thrombin, which functions in part to stabilize the fibrin clot, the rate of thrombin generation more sufficiently describes overall thrombogenicity.¹⁶ Thrombin generation assays in platelet-rich plasma (PRP) have been published in the literature and, despite the usefulness of such assays, their application has been limited largely because of technical issues.¹⁷ Traditionally these assays measured thrombin generation by sub-sampling a clotting plasma sample, a labor and time-intensive methodology.¹⁷ However recent advances have enabled thrombin to be fluorescently tagged with a slow-binding substrate, facilitating a continuous and sensitive measurement of thrombin generation in clotting plasma over time.¹⁸ Furthermore advances in software and instrumentation have contributed to the automation of large portions of the current fluorescence assay workflow, allowing for reproducible data collection outside of specialized labs.¹⁹ Therefore using a fluorogenic assay to measure thrombin generation in clotting plasma exposed to a coated intracranial device is a feasible way to measure the thrombogenicity of the coating, though similar testing has been reported only once in the literature.²⁰

Finally, since the developed coating technology contains the naturally derived bioactive and antithrombotic agent human glycoprotein thrombomodulin (hTM), challenges inherently associated with bioactive components are introduced. To understand these challenges it should first be noted that bioactive coatings for stents in and of themselves are not novel; in fact, many bioactive coatings have been developed for drug-eluting cardiovascular stents.^{14, 21, 22} It is from this literature that three primary challenges with bioactive coatings are outlined: first such coatings are difficult to sterilize, second they are prone to degradation, and third it is often difficult to orient the bioactive agent in order to maintain functionality.^{14, 21, 22} Despite the associated

challenges, preliminary in-vitro and in-vivo data discussed herein has indicated that the inclusion of a bioactive agent in the developed coating chemistry improves coated device thrombogenicity above and beyond passive hemocompatible coatings.

Other groups have reported on the development of hemocompatible surface coatings for renal or cardiovascular stents or stent grafts and their use in the neurovascular space^{23,24}, or else reported on the use of commercially available coated cardiovascular stents in the cerebrovasculature in the literature.²⁵⁻²⁷ One other group has reported on heparin and albumin coatings for the commercially available Acandis Acclino® stent-assisted coiling device.²⁸ We are the first group to develop a coating technology compatible with both commercially available intracranial flow diverting devices and stents, characterize the technology's chemical composition and uniformity post deposition, and conduct in-vivo testing.

The idea of developing hemocompatible surface coatings to improve the long-term performance of vascular implants has been around for some time, though advances have been recently made. In 2016 Hynninen et al.²⁹ reported on a solution-based method to modify the biofunctionality of stainless steel using silane-polyethylene glycol layers and concluded that the coating has the potential to significantly reduce non-specific surface biofouling by proteins and bacteria. Also in 2016, Santos et al.³⁰ reported on a technique to create plasma-activated coatings for stainless steel cardiovascular stents with the capacity for surface passivating protein-binding and low thrombogenicity in-vitro. Likewise in 2014 Leslie et al.³¹ reported on a surface coating for medical grade tubing and catheters with the potential to prevent thrombotic occlusion and biofouling. However translation of these technologies to intracranial devices has not been done; likewise, their long-term functionality in-vitro and in-vivo has not been reported. A review of other hemocompatible surface modification and coating strategies for intravascular stents used for treating coronary and peripheral arterial disease was written by myself and published in the Winter 2015 *SurFACTS in Biomaterials* newsletter, a technical newsletter for the Surfaces in Biomaterials Foundation. It is reproduced here since it provides a comprehensive review of the literature on hemocompatible surface coatings and modifications for intravascular stents.

A Review of Hemocompatible Surface Modification and Coating Strategies for Intravascular Stents³²

Introduction

Intravascular stents were first introduced in the 1980s and used exclusively to treat coronary and peripheral arterial disease, which are characterized by progressive narrowing of an artery due to the accumulation of fatty lesions.¹⁴ The intravascular stent was designed to enlarge the lumen of the diseased artery, providing permanent mechanical arterial wall support, in addition to serving as a scaffold for healthy endothelial cell growth.¹⁴ Yet these devices are not without complication; approximately 25% of patients treated with intravascular stents experience either recurrent stenosis or late-stage thrombosis and require additional intervention.³³ For the past decade or so, intravascular stents have also been used in the cerebral circulation to support embolization coil placement in the treatment of cerebral aneurysms, which are local dilations of a brain artery; additionally, they have been used to treat cerebral artery atherosclerosis and stenosis.^{34, 35} While these cerebral stents differ in function, material composition, and design from their cardiovascular counterparts they still pose risks to the patient, like increased potential for thrombotic embolization and stroke.³⁴ Likewise, the limitations of the intravascular stent in both the cardiovascular and cerebral circulations has led to the investigation of new stent materials, designs, surface modifications and coatings to mitigate thrombosis-related risks and increase device hemocompatibility. This review outlines the scope of the strategies that have been employed for intravascular stent surface modification and coating as they have progressed from bioinert to bioactive, and ultimately biomimetic.

Surface Modifications

Because thrombus formation and embolization are the most substantive risks of intravascular stents, scientists' earliest attempts to improve stent hemocompatibility were to modify the stent surface directly. This choice was made because initiation of the coagulation cascade requires the adsorption of plasma proteins, tissue, and complement factors to the biomaterial surface, the speed of which is governed by surface characteristics. Thus changes in surface composition, morphology, charge, wettability, and roughness elicited by cleaning, polishing, and etching methods can affect protein

and factor adsorption.^{36, 37} Yet the influence of these surface characteristics on device hemocompatibility remains ambiguous and cannot be generalized across materials.²² For instance, uncharged hydrophilic surfaces generally promote low surface-blood interaction, yet the highly hydrophobic material of expanded polytetrafluorethylene has been shown to have high hemocompatibility.²² Thus, it has been difficult for scientists to identify generic surface characteristics that promote hemocompatibility independent of bulk material.

Passive Inorganic Coatings

Scientists have also investigated coating intravascular stents with passive inorganic films, the goal of which is to act as an inert barrier between the bulk stent material and the bloodstream or vascular tissue.¹⁴ Notable such coatings are gold, silicon carbon (SiC), diamond-like carbon (DLC), and titanium-nitride-oxide.

Typical deposition techniques for these coatings are plating – for gold – and plasma enhanced chemical vapor deposition (PECVD) for SiC, DLC, and titanium-nitride-oxide deposition.³³ PECVD is a process whereby thin, uniform films can be deposited on a substrate in a vacuum chamber.³³ It works by using electrical energy to generate plasma in a vacuum chamber.³³ The plasma then transfers energy to a mixture of gaseous precursors, transforming them to radicals, ions, and other highly energetic species.³³ Depending upon the interaction of the precursor mixture with the substrate, either etching or deposition occurs on the substrate surface.³³ In this manner thin and conformal films can be deposited at relatively low temperatures.³³

Gold was initially tested as a passive, inorganic intravascular stent coating because it is a well-known inert material with dental applications.²¹ Yet a clinical study called NUGGET, done on commercially available cardiovascular stents coated with gold indicated a recurrent stenosis rate of 37.7%, which was higher than the associated rate for bare metal stents among patients at six-month follow-up.³³ Likewise, SiC was an initially attractive coating to scientists due to its high hardness, chemical inertness, and smooth surface finish on scanning electron microscopy (SEM), yet it is also brittle and may crack.³⁸ Further, the TENISS and TRUST trials, which were large multicenter trials studying SiC coated cardiovascular stents, indicated no improvement in clinical outcome in patients treated with SiC coated stents compared to bare metal stents.³⁹ DLC was also an initially attractive coating because it is an inert hydrocarbon³³ that has been

shown to exhibit a smooth surface on SEM,³⁸ yet several large clinical trials have independently concluded that DLC coated cardiovascular stents do not significantly reduce recurrent stenosis rates compared to bare metal stents and therefore are not clinically beneficial.³³ Scientists chose to investigate the hemocompatibility of titanium-nitride-oxide stent coatings because titanium-nitride-oxide is chemically inert and cannot transfer electrons to plasma proteins.³³ Unlike SiC and DLC, titanium-nitride-oxide coating on cardiovascular stents has demonstrated clinical benefits. The TiNOX clinical trial, which compared 45 patients possessing de novo atherosclerotic lesions treated with titanium-nitride-oxide coated stents and 47 patients treated with bare metal stents, found that at 30 days no stent thrombosis had occurred in either group.³³ However, more studies are required to see if this finding can be corroborated.

Bioactive Coatings

The strategy of bioactive coatings is to immobilize an active pharmacological agent on the intravascular stent surface in order to aid regulation of coagulation, the complement system, or inflammation processes.²¹ In other words, bioactive coatings seek to mimic the endothelial cell microenvironment. The earliest attempts at this came in the 1990s and sought to control the coagulation cascade through the immobilization of heparin.²¹ Later researchers investigated the immobilization of direct thrombin inhibitors, in addition to the immobilization of other anticoagulant molecules like human thrombomodulin (hTM) and nitric oxide (NO).²¹ Nevertheless, the heparin bioactive coating is the oldest and most widely used on intravascular stents.²¹ Initially discovered in 1961 as an anticoagulant drug, heparin was later found to interact with antithrombin, which accelerates the binding of thrombin and inhibits amplification of the coagulation cascade.²¹ The heparin coating strategies range from physical adsorption to covalent side-on or end-on immobilization.²¹ Direct thrombin inhibitors have also been investigated, as they are anticoagulant molecules that directly block thrombin active sites and therefore inhibit coagulation.²¹ Hirudin, naturally derived from snake venom, is one such thrombin inhibitor that has successfully been covalently immobilized to create a surface with anticoagulant properties.⁴⁰ Other synthetic thrombin inhibitors like D-Phe-Pro-Arg-chloromethylketone⁴¹ and an amidine derivative⁴² have been covalently immobilized to foreign surfaces with positive anticoagulant and anti-inflammatory effects. Additionally researchers have tried inhibiting the coagulation cascade via other

anticoagulant molecules like hTM and NO. Particularly hTM functions as an endothelial cell surface glycoprotein promoting protein C activation, which in turn acts as an anticoagulant.⁴³ Akashi et al.⁴⁴ reported the successful immobilization of hTM on a foreign surface in 1992 and, since then, hTM has been immobilized by other researchers.⁴⁵ NO has been shown to be a modulator of vascular tone and permeability, in addition to inhibiting leukocyte adhesion and platelet activation.²¹ Likewise several research groups have reported both NO-eluting and NO-generating coating designs on polymer and metal substrates with promising results.^{46,47} Yet two primary challenges exist for all bioactive coatings: 1) properly orienting the pharmacologic agent within the coating and 2) protection of the pharmacologic agent from the physiological degradation process. Likewise, how to sterilize such coated materials and their limited shelf stability are technical challenges.²²

Micro- and Nano-Structured Surfaces

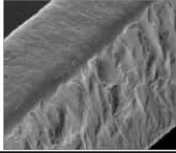
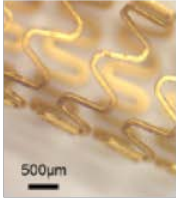
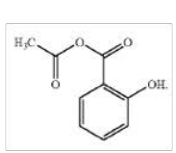
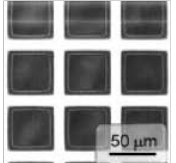
Recent advances in both micro- and nanotechnology have enabled researchers to modify intravascular stent surface characteristics on the micro and nano-scales in order to promote endothelial cell adhesion and proliferation, as well as inhibit the adhesion of platelets and plasma proteins.¹⁴ The interest in this area has grown because it has been hypothesized that endothelial cells grow in-vivo on a micro- and nano-patterned basement membrane; thus, the potential for biomimicry has fueled interest.¹⁴ While 2D micro- and nano-structured features have been created using many fabrication techniques – photolithography, focused-ion-beam lithography, nanoimprint lithography, physical vapor deposition, chemical etching, among others – integrating these small-scale features onto 3D biomaterials remains a challenge.¹⁴ Additionally the mechanisms underlying the interactions between vascular cells and the structured surface are not yet well understood.¹⁴ Future investigations should continue to study how feature dimension and geometry affect the adhesion, proliferation, and migration of vascular cells.¹⁴

Summary

To mitigate thrombosis-related risks and increase intravascular stent hemocompatibility researchers have investigated and employed various stent surface

modifications and coatings ranging from bioinert, to bioactive, and biomimetic. These strategies are summarized in Table 1.

Table 1: Summary of Intravascular Stent Surface Modification and Coating Strategies.

	Modification or Coating	Merits	Demerits	References
	Surface Modification	<ol style="list-style-type: none"> 1. Relatively easy to create 2. Durable 3. Sterilizable 	<ol style="list-style-type: none"> 1. Influence on hemocompatibility is difficult to generalize 	Werner et al. ²²
	Passive Inorganic Coating	<ol style="list-style-type: none"> 1. Created via common film and coating deposition techniques 2. Sterilizable 	<ol style="list-style-type: none"> 1. Long-term hemocompatibility results have lacked promise 	Nazneen et al. ¹⁴ Sydow-Plum et al. ³³
	Bioactive Coating	<ol style="list-style-type: none"> 1. More closely mimics endothelial cell micro-environment 	<ol style="list-style-type: none"> 1. Prone to degradation; limited stability 2. Difficult to orient active agent to maintain functionality 3. Difficult to sterilize 	Qi et al. ²¹ Werner et al. ²²
	Micro- and Nano-Structured Surface	<ol style="list-style-type: none"> 1. Most closely mimics endothelial cell micro-environment 	<ol style="list-style-type: none"> 1. Interactions between structured surface and vascular cells are poorly understood 	Nazneen et al. ¹⁴

While attempts to change the macro stent surface characteristics have been inconclusive, the titanium-nitride-oxide coating remains the most promising passive, inorganic coating. Bioactive coatings are also promising; however more work needs to be done to address the limitations. An alternate strategy is to create a micro- and nano-structured stent surface that mimics the in-vivo basement membrane. This could even be combined with current bioactive coatings, though further studies are needed to elucidate the mechanisms driving the interaction between vascular cells and the structured surface.

Objectives

Given the state of the literature on hemocompatible and antithrombotic coatings in general and intracranial device coatings in specific, there remains an express need for the development and evaluation of an antithrombotic coating that can be applied to commercially available intracranial devices to at least lessen or at best eliminate the risky DAPT standard of care associated with their placement, as well as expand their use to patients suffering from acute SAH. Medical device companies have already recognized this need in the market and the associated impact it could have on the lives of patients. In 2015, medical device giant Medtronic Inc. published on a nanometer-scale coating they developed for their intracranial Pipeline™ Flex flow diverting device called Shield Technology™ that could be an effective coating technology to mitigate thrombogenic complications.²⁰ Additionally, a clinical trial assessing the incidences of stroke and neurological adversities or death associated with Medtronic's Shield Technology™ in the UK has been conducted (the final data collection date was December 2016) and the results should be released soon.⁴⁸ Additionally, Medtronic has recently reported on the antithrombotic properties of their Shield Technology™, and that it may provide increased lubricity to neuroradiologists during device deployment.²⁰ Likewise, several research groups have recognized the impact surface-modified intracranial stents could have on aneurysm patients, and have published on using either the Cordis Bx Velocity™ coronary stent with Hepacoat™ in the canine²⁵ and human cerebral circulations²⁶, or else on in-vitro thrombogenicity testing of heparin or human serum albumin surface coatings for the Acandis Acclino® stent-assisted coiling device.²⁸ Other groups have reported on the development of hemocompatible surface coatings for renal or cardiovascular stents or stent grafts and their use in the neurovascular space^{23, 24}, or else reported on the use of commercially available sirolimus-eluting cardiovascular stents in the canine cerebrovasculature.²⁷ However, no research group has published on coating chemistries or techniques that would be suitable for the complex geometries associated with commercial intracranial flow diverting devices. There is therefore interest in developing a competitive nanometer-scale antithrombotic coating technology for intracranial devices.

Fundamentally, a hemocompatible and antithrombotic coating technology suitable for *both* intracranial stents and flow diverting devices has the potential to revolutionize the endovascular treatment of intracranial aneurysms by minimizing the

patient risk associated with dual anti-platelet therapy in the elective setting, as well as expanding the use of intracranial stents and flow diverters to include ruptured intracranial aneurysms. Specifically the purpose of such a coating technology is four fold: 1) minimize the incidence of thromboembolic events in intracranial aneurysm patients treated electively with intracranial stents and flow diverters, 2) allow for the discontinuation of dual anti-platelet therapy in patients treated electively with intracranial stents or flow diverters if emergent surgery is needed in the immediate post-operative period, 3) minimize thromboembolic events in patients non-compliant with dual anti-platelet therapy following intracranial stent or flow diverter placement surgery and 4) expand the use of commercially available intracranial stents and flow diverters to include the treatment of patients with acute SAH in conjunction with systemic aspirin use. Therefore, a novel nanometer-scale antithrombotic coating for commercially available intracranial stents and flow diverters was developed and evaluated via the following three specific aims:

1. Specific Aim #1 is to develop the deposition technique and chemistry to create a nanometer-scale hemocompatible and antithrombotic coating for commercially available intracranial stents and flow diverters.
2. Specific Aim #2 is to characterize the developed coating chemistry and assess its hemocompatible and antithrombotic functionality.
3. Specific Aim #3 is to further develop and evaluate the coating technology as a platform for the attachment of FDA-approved molecules.

CHAPTER 2

Specific Aim #1: Development of the Nanometer-Scale Hemocompatible and Antithrombotic Coating Chemistry and Deposition Technique Suitable for Commercially Available Intracranial Devices

The primary motivation for developing a nanometer-scale hemocompatible and antithrombotic coating for intracranial stents and flow diverting devices is the fact that thromboembolic complications are not insignificant in intracranial aneurysm patients treated endovascularly. In fact, the literature suggests that approximately 5% of patients treated with the Pipeline™ flow diverting device and dual anti-platelet therapy (DAPT), and 7% of patients treated with intracranial stents for stent-assisted coiling and DAPT experience thromboembolic complications.^{7, 10} Furthermore DAPT is associated with increased patient risk, despite being the current standard of care.¹¹⁻¹³ Therefore such a coating would at least minimize or at best eliminate the need for endovascularly treated intracranial aneurysm patients to receive DAPT, decreasing or eliminating the associated patient risks; such a coating would also increase intracranial device indications for use to include patients suffering from acute SAH – in short, a coating technology like this has the potential to revolutionize the endovascular treatment of intracranial aneurysms.

Several research groups have recognized the revolutionizing impact surface-modified intracranial stents, in particular, could have on aneurysm patients and have published promising results using the Cordis Bx Velocity™ coronary stent with Hepacoat™ in the human cerebral circulation, or else on the improved in-vitro thrombogenicity of heparin and human serum albumin surface coatings for the Acandis Acclino® stent-assisted coiling device.^{26, 28} Likewise, medical device companies have also recognized the large societal and market impact a hemocompatible and antithrombotic technology holds. In 2015 medical device giant Medtronic Inc. published on a nanometer-scale coating they developed for their intracranial Pipeline™ Flex flow diverting device called Shield Technology™ that could be an effective coating technology to mitigate thrombogenic complications.²⁰ Since then other medical device companies have become interested in developing a competitive nanometer-scale antithrombotic coating.

Given the potential for great societal impact, and given the healthy commercial interest in technologies like these, a novel nanometer-scale hemocompatible and antithrombotic coating chemistry and deposition technique suitable for commercially available intracranial stents and flow diverting devices was developed. A schematic of the developed coating chemistry is shown as Figure 2.

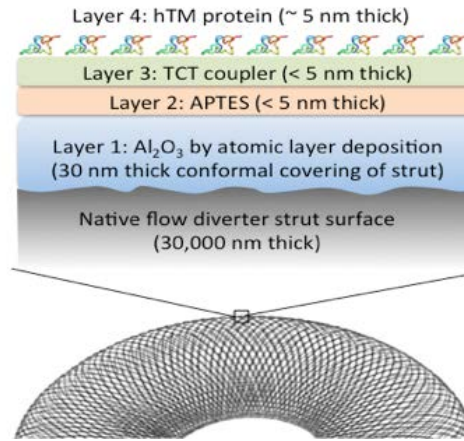


Figure 2: Schematic illustration of the developed hemocompatible and antithrombotic coating technology for intracranial devices.

The developed coating deposition technique works by covalently bonding molecules sequentially to an intracranial device surface rather than relying on physical adsorption, which is characteristic of spraying and dipping techniques. This chemical bonding is in part facilitated by a microfabrication and thin film deposition technique known as atomic layer deposition (ALD). Additionally the developed coating deposition technique and chemistry facilitates the conjugation of human glycoprotein thrombomodulin (hTM) to the chemically bound molecules on the device surface; hTM actively disrupts coagulation since it functions as a protein cofactor in the thrombin-catalyzed activation of protein C and therefore is a natural antithrombotic agent.⁴⁹ Preliminary in-vitro and in-vivo studies indicate that layers 1, 2, and 3 in the developed coating technology, shown in Figure 2, is passively hemocompatible, meaning that while they do not actively disrupt the human coagulation cascade their combined thrombogenicity is improved over uncoated devices. Additionally, preliminary in-vitro and in-vivo studies have indicated that the bioactive antithrombotic coating component, hTM, is functional when immobilized on a device surface.

In summary, a very thin covalently-bound, multilayer surface coating technology containing the naturally derived bioactive and antithrombotic agent hTM was developed.

Inclusion of hTM in this coating chemistry was a targeted effort to actively disrupt the human coagulation cascade. Furthermore, because commercially available intracranial devices are often deployed in tortuous vasculature, it is important that any coating layers deposited on their surface do not inhibit the underlying device mechanics during both catheter loading and vessel deployment; therefore, a targeted effort was made to develop a nanometer-scale coating, conformal to individual device wires, to minimize any adverse impact of the coating layers on device biomechanics and to maximize coating durability. A summary of the key design attributes associated with the developed coating technology and deposition technique are summarized in Figure 3.

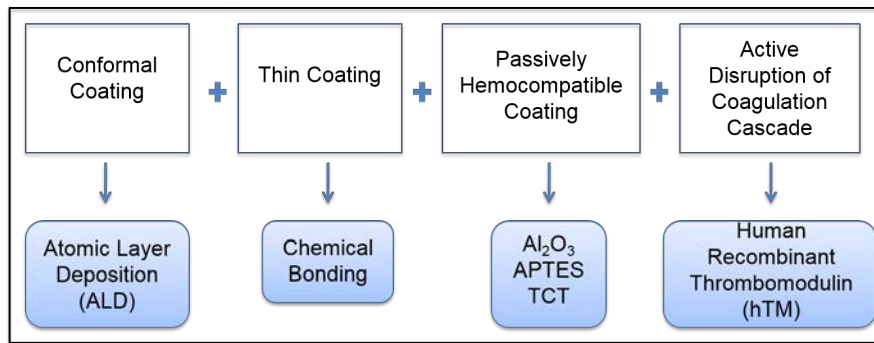


Figure 3: The key design attributes of the developed coating chemistry and deposition technique for intracranial devices.

It should also be noted that while the individual steps in the developed coating chemistry, shown in Figure 2, and deposition technique are not in and of themselves novel, their combination and application to intracranial stents and flow diverters is. In particular, the thin film deposition technique of ALD, used in the developed coating deposition to chemically bond a layer of aluminum oxide on the intracranial stent or flow diverter surface, has been used as a technique to coat cardiovascular stents in the past. In fact, in 2014 Zhong et al.⁵⁰ published work that used ALD to bond aluminum oxide to a stainless steel cardiovascular stent surface. Zhong et al. further modified the aluminum oxide layer by 3-aminopropyl-triethoxy-silane (APTES), which is also done in the developed coating deposition; however the group sequentially attached 2-metacryloyloxyethyl phosphorylcholine (MPC) to the APTES layer – a striking difference from the developed coating deposition.⁵⁰ Instead, our coating deposition protocol attaches 2,4,6-trichloro-1,3,5-triazine (TCT) to the APTES layer, which acts as a coupler for the bioactive agent hTM; using TCT as a means to attach hTM was an idea taken from work reported by Yeh and Lin in 2009.⁵¹ Even using hTM as a bioactive surface

agent to inhibit thrombus formation is not novel. In 1992 hTM was first immobilized by Dr. M. Akashi;⁴⁴ thereafter, hTM surface modifications have been proposed by many other research groups.^{21, 52} To reiterate, the implication of all of this is that while the individual steps in the developed coating deposition technique are not in and of themselves novel, their sequential deposition on a intracranial stent or flow diverter surface is. Furthermore by chemically bonding molecules in layers to an intracranial device allows for a thin (<50 nm), relatively conformal coating to the individual device wires that likely leaves the underlying device mechanics uninhibited. These attributes, in combination with the attachment of what initial in-vitro and in-vivo testing indicates to be functional hTM, make the developed coating unique. More details on these topics will be addressed herein.

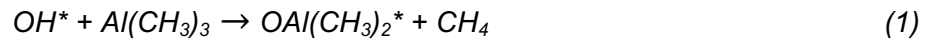
Coating Chemistry and Deposition Technique

The deposition method for this developed coating technology is a layer-by-layer technique and is succinctly outlined in Figure 2. From Figure 2 it can be seen that that aluminum oxide is initially deposited on the intracranial stent or flow diverter surface. This layer provides a uniform oxide surface, on which each subsequent layer is deposited. This is especially important in the case of flow diverting devices, which can be composed of wires made from two or more metal alloys. With such devices, coating deposition would require functionalization of each wire type separately – a challenge. Deposition of the aluminum oxide layer therefore provides a uniform oxide surface that can be functionalized in a consistent manner, regardless of the material composition of the underlying device.

As the first layer in the developed multi-layer coating, aluminum oxide is the foundation on which each subsequent layer is deposited. As a result, it is vital that it is deposited in a thin and conformal manner relative to the underlying stent or diverter wires. If this layer is too thick, or else non-conformal, addition of each subsequent layer will only increase coating thickness or the degree of non-conformality, leading to increased device stiffness. In the nanofabrication field, thin film conformality is the ability of a film to coat substrate nanopores, even those with high aspect ratios, with consistent thickness.⁵³ Such a change in device mechanics would compromise the ability of, or in the worst case prevent, the device from being loaded into its deployment catheter, promoting cracking and chipping of the deposited coating in the process; it may also

negatively impact apposition of the device against the vessel wall once deployed. To avoid these problems, atomic layer deposition (ALD) is used in the developed technology to deposit the aluminum oxide layer. ALD is a technique for depositing thin, conformal films on 2D and 3D substrate geometries and was originally developed in the 1970's for manufacturing thin film electroluminescent displays.⁵⁰ Since then it has been used extensively in the semiconductor industry as a means to fabricate integrated circuits.⁵⁰ ALD is able to achieve highly conformal film deposition due to the fact that it utilizes two surface reactions to deposit a binary compound film; in other words, film growth occurs by sequentially exposing the substrate to two individual gaseous precursors, and purging the ALD chamber between exposure steps to remove active source gas.⁵⁴ The sequential precursor exposure steps are self-limiting surface reactions.⁵⁵

The ALD process begins by placing a substrate in the ALD chamber and evacuating it. Next the chamber is pumped with the first gaseous precursor, trimethylaluminum (TMA).^{55, 56} TMA reacts with the substrate according to the scheme shown in Equation 1^{55, 56}:

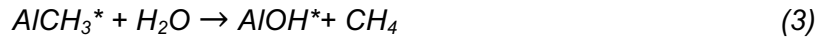


In Equation 1 the asterisks denote the surface species, also note that metallic surfaces are naturally oxidized by hydroxyl groups due to lattice imperfection, as well as the natural surface adsorption of water by van der Waals forces.⁵⁰ Next argon gas is used to purge the chamber of TMA and reaction by-products; oxygen plasma is then pumped in.⁵⁶ The oxygen plasma reacts with the substrate in a combustion-like process yielding primarily –OH groups on the substrate surface, but also a very small concentration of surface carbonates, as confirmed by in-situ Attenuated Total Reflection Fourier Transform Infrared Spectroscopy (ATR-FTIR).⁵⁷ The carbonates are short-term reaction intermediates and decompose according to the series reaction when exposed to prolonged oxygen plasma, as shown in Equation 2.⁵⁷



Pseudofirst-order kinetics govern how the surface methyl ligands, shown in Equation 1, combust to yield surface –OH groups and Al₂O₃ (forming CO, CO₂, and H₂O reaction products).⁵⁷ Additionally a second reaction mechanism is possible during the oxygen

plasma exposure step and is shown in Equation 3. This mechanism is initiated upon formation of H₂O in a chamber, which is a product of combustion⁵⁸:



In Equation 3 the asterisks denote the surface species. Note that this secondary reaction can only occur when –CH₃ groups are present on the surface and therefore becomes insignificant when most –CH₃ groups are reacted away by the combustion-driven reaction mechanism.⁵⁸ It should be noted that a third reaction mechanism is possible during the oxygen plasma exposure step and is one that generates higher order hydrocarbon (C₂H_x) reaction products, which have been observed by mass spectroscopy. Furthermore, first principles density functional theory calculations suggest that this mechanism is favored over the combustion reaction mechanism.⁵⁸ Together, these three reaction mechanisms are thought to explain the primary surface reactions that occur in the oxygen plasma exposure step; nevertheless, additional reaction mechanisms cannot be excluded. The reader is directed to Heil et al.⁵⁸ for more information on this point. Next the chamber is purged of oxygen plasma, again by argon gas, and the ALD cycle is complete.⁵⁶ Following this the chamber is again pumped with TMA and the entire cycle is repeated.

The use of oxygen plasma in the ALD cycle is characteristic of plasma enhanced-ALD (PE-ALD), which enables lower chamber temperatures to be used, relative to and distinct from thermal ALD processes.⁵⁶ This is because oxygen plasma is a more reactive oxidant than H₂O, or the oxidant used in thermal ALD processes; thus, the surface reactions in PE-ALD are less reliant on thermal activation.⁵⁸

Alternatively exposing an initially oxidized substrate surface to two, individual gaseous precursors and purging in-between allows each surface reaction to be driven to completion each cycle.⁵⁵ This is because an individual precursor will adsorb and subsequently desorb from substrate surface areas in which the reaction has reached completion, and instead proceed to react with un-reacted surface areas.⁵⁵ This yields uniform and pinhole-free film deposition, including the device interior and areas between crossed wires.⁵⁵ Repetition of the two self-limiting surface reactions allows for near linear growth of aluminum oxide with the number of PE-ALD cycles.⁵⁵ Aluminum oxide cycle growth has been characterized by both spectroscopic ellipsometry and quartz crystal microbalance measurements and found to be between 1.1-1.2 angstroms per

ALD cycle.⁵⁵ Notwithstanding, aluminum oxide cycle growth is temperature dependent and decreases with temperatures between 177-300°C.⁵⁵

Deposition of aluminum oxide on an intracranial stent or flow diverter surface is done in this coating protocol with the OpAL PE-ALD Instrument (manufactured by Oxford Instruments) at the University of Iowa Microfabrication Facility (UIMF) in an ISO 5 (Class 100) clean room. The PE-ALD process with oxygen plasma, previously described, is the aluminum oxide deposition method. In this protocol, the ALD chamber temperature is kept constant at 200°C and the ALD cycle number is set to 300. Choice of 300 cycles of aluminum oxide deposition in this protocol was, in some sense, arbitrary. Depositing an oxide coating in the tens of nanometers thick on intracranial devices seemed like a reasonable starting point, with the intent to optimize this thickness at a later time, if necessary. The PE-ALD process begins when the chamber reaches a base pressure of 10 mTorr. This base pressure was suggested by Oxford Instruments based on the capacity of the vacuum pump installed with the UIMF PE-ALD instrument.

Prior to placement of the stent or diverter in the PE-ALD chamber, the device is ultrasonically cleaned in a Branson Sonicator. This is done under a chemical hood in the UIMF ISO 5 clean room. Sonicators use ultrasound waves to produce cavitation bubbles. When these bubbles burst close to the device surface local high pressure results, leading to an instantaneous and local temperature increase.⁵⁹ The combination of the local high pressure and temperature removes surface contaminants at the cost of etching the surface.⁵⁹ The sonication cleaning protocol followed is to submerge the device in the solvents acetone, isopropyl alcohol, methanol, and de-ionized (DI) water and sonicate in each for four minutes. The device is then submerged in acetone again and immediately dried under a stream of ultra-high purity (99.999%) nitrogen gas for three minutes. Validation of this cleaning protocol was done qualitatively, via scanning electron microscopy (or SEM) imaging. Figure 4 shows commercial flow diverting device #1 before (Figure 4A) and after ultrasonic cleaning with the aforementioned protocol (Figure 4B).

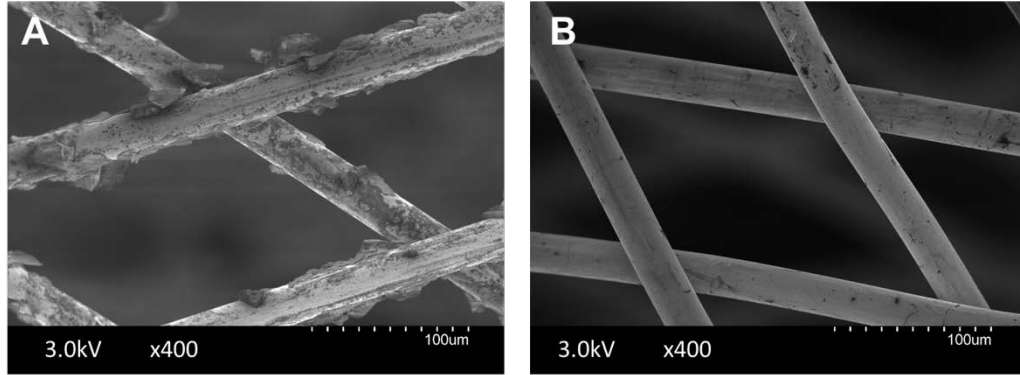


Figure 4: (A) SEM image of commercial flow diverting device #1 prior to ultrasonic cleaning with the established protocol. (B) The same device after ultrasonic cleaning.

The aluminum oxide cycle growth rate for the OpAL PE-ALD instrument in the UIMF has been determined with spectroscopic ellipsometry (M-2000 instrument, J.A. Woollam Co.) thickness measurements on 10 individually coated one centimeter square p-doped silicon wafers exposed to 300 PE-ALD cycles; measurements were taken at 10 discrete locations per wafer. Spectroscopic ellipsometry is an optical technique for thin film measurement.⁶⁰ This data indicates that the aluminum oxide growth rate is ~ 0.106 nm per cycle at 200°C ; the aluminum oxide layer thickness on these wafers was found to be 31.86 ± 0.26 nm. Researchers at the UIMF have also independently tested the aluminum oxide growth rate characteristic of this instrument across a range of cycles; spectroscopic ellipsometry thickness measurements on individual silicon wafers exposed to 100, 200, and 300 PE-ALD cycles suggest an instrument aluminum oxide growth rate of ~ 0.09 nm per cycle at 200°C .

After deposition of the aluminum oxide (Al_2O_3) layer on the intracranial stent or flow diverter surface the coating process proceeds by silanization of the Al_2O_3 layer with an amino-terminated silane, called 3-aminopropyl-triethoxysilane or APTES, as shown in Figure 2. Silanization of a metal oxide is not novel; therefore reaction parameters like temperature, time, and silane concentration were adapted from Ploetz et al.⁶¹ Specifically toluene is heated to 65°C in an oil bath. Next the APTES is added to the toluene to yield a 1% v/v solution. After the device is cleaned via the established ultrasonic cleaning protocol, it is placed in this mixture and allowed to react for 20 minutes (while stirring). A schematic of the silanization chemical reaction is shown in Figure 5.

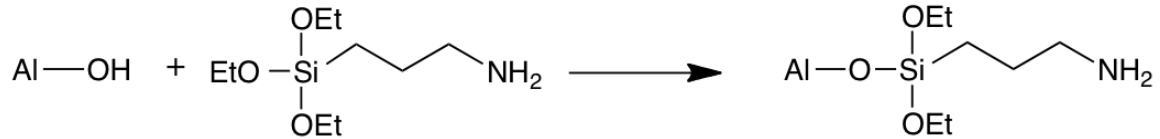


Figure 5: Schematic of the APTES silanization chemical reaction used to functionalize the PE-ALD deposited Al_2O_3 layer on a stent or flow diverter device.

Upon reaction for 20 minutes, the device is removed from the toluene-APTES solution and rinsed with toluene three times, to dilute the silanization surface reaction, and finally rinsed with methanol three times to remove toluene residue. The device is then dried under a stream of ultra-high purity (99.999%) nitrogen gas for five minutes. Ultimately this reaction procedure provides an activated device surface; in other words, a device surface with free amino groups for subsequent functionalization (as shown in Figure 5).

The silanized device surface is further functionalized by TCT, which provides surface $-\text{Cl}$ groups that act as coupling agents to attach the hTM. Using TCT to attach hTM is not novel and was first reported by Yeh and Lin in 2009 on a nitinol substrate.⁵¹ Therefore reaction parameters like temperature, time, and TCT concentration were adapted from Yeh and Lin.⁵¹ Specifically a schlenk flask is put under flowing nitrogen gas overnight. Next a 0.27M solution of TCT-toluene solution is made and nitrogen gas is allowed to bubble through for 20 minutes. This toluene-TCT solution is added to the schlenk flask, still under nitrogen purge, and heated to 70°C in an oil bath. The device, clean and dry from the silanization step, is added to schlenk flask and allowed to react for 4 hours and 15 minutes (while stirring). A schematic of the TCT chemical reaction is shown in Figure 6.

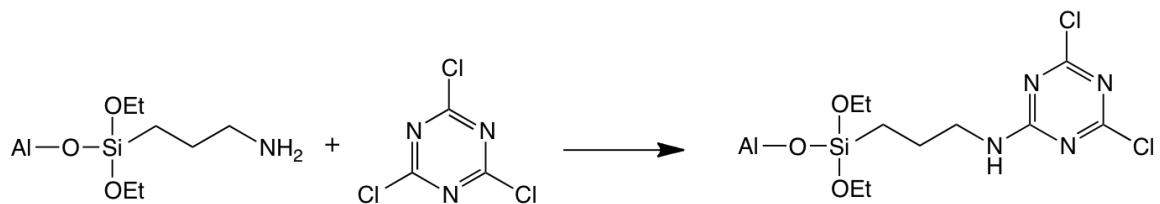


Figure 6: Schematic of the TCT coupler chemical reaction used to functionalize the APTES layer on a stent or flow diverter device.

Upon reaction for 4 hours, 15 minutes the device is removed from the toluene-TCT solution and rinsed with toluene three times, to dilute the TCT surface reaction, and finally rinsed with methanol three times to remove toluene residue. The device is then

dried under a stream of ultra-high purity (99.999%) nitrogen gas for five minutes and placed in a clean, plastic test tube.

Immobilization of the hTM protein to the TCT-activated device surface is then done by following the generic protocol outlined by Yeh and Lin.⁵¹ This protocol consists of dissolving the hTM in PBS solution and reacting with the device at 4°C for 24 hours. A schematic of the hTM protein reaction is shown in Figure 7.



Figure 7: Schematic of the hTM protein reaction that couples to the TCT layer on a stent or flow diverter device.

The hTM protein used in this protocol is human recombinant, contains only the extracellular domain, and is purchased from Sigma Aldrich. The decision to use recombinant hTM containing only the extracellular domain is based on the fact that hTM binds thrombin in the extracellular domain. In a 1987 paper K. Suzuki et al.⁴⁹ showed that hTM likely binds thrombin in its EGF-like extracellular domain, containing amino acid residues 227-462. The structure of hTM is shown in Figure 8.

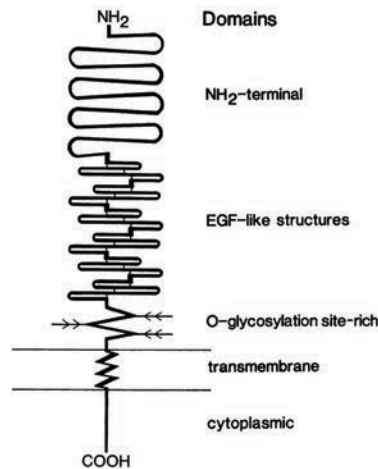


Figure 8: A schematic of the structure of human thrombomodulin (hTM), originally printed in Suzuki et al.⁴⁹

It was chosen to dissolve 10 ug hTM in 500 µL 1X DPBS (Dulbecco's 1X DPBS without calcium and magnesium chloride), yielding a 0.02 mg/mL concentration of hTM. Using this particular concentration of hTM in solution was motivated by the high cost of purchasing 10 ug of hTM from Sigma (\$265 for 10 ug of hTM), and also because it was

found that 500 μL was the smallest volume that would completely submerge a 20 mm device (with diameter < 4.2 mm) when reacted in a straight (non-bent) configuration. Thus the 0.02 mg/mL concentration of hTM is the most concentrated protein solution possible for a mid-length device, given the monetary constraints. The specific protocol followed to carry out the protein reaction is to first UV sterilize the device in a standard cell culture hood for 15 minutes. Next the 0.02 mg/mL solution of hTM is made by dissolving 10 μg lyophilized hTM in 500 μL DPBS in a 1 mL plastic vial, followed by gently mixing with a pipette to dissolve. Under the sterile cell culture hood, the sterilized device is placed in the hTM solution in a straight configuration and kept at 4°C for 24 hours. Upon completion of the reaction, the device is removed from the hTM solution in the sterile cell culture hood, rinsed with DPBS, and allowed to air-dry for 15 minutes.

Special consideration must be made for devices both 30 mm in length or longer, and devices 20 mm in length but with diameters greater than 4.2 mm. This is because these devices are either too long or too wide, respectively, to be fully submerged in the 500 μL of 0.02 mg/mL hTM solution. In the case of devices 20 mm in length with diameters greater than 4.2 mm, the hTM solution was diluted two-fold and the devices were allowed to react for two days (at 4°C) in a straight configuration within a 1 mL plastic vial. In the case of devices 30 mm in length or longer, the hTM solution was diluted four-fold and the devices were coiled within individual wells of a 24-well plate; these devices were allowed to react for two days (at 4°C). All devices were then sent to a third-party company for in-vitro and in-vivo functionality testing, results of these tests are pending.

In 2002 Niimi et al. published on the thermal and storage stability of recombinant hTM used as the Japanese reference standard.⁶² The group found that the relative activity of the hTM standards stored at 40°C for 10 weeks did not differ significantly from their respective initial activity.⁶² However, temperature and storage-dependent losses were noted for samples stored for 10 weeks at 60°C , 70°C , and 80°C .⁶²

CHAPTER 3

Specific Aim #2: Characterize the Developed Coating Chemistry and Assess its Hemocompatible and Antithrombotic Functionality

A novel nanometer-scale hemocompatible and antithrombotic coating chemistry and deposition technique for commercially available intracranial stents and flow diverting devices was developed as part of specific aim #1, the details of which are outlined in Chapter 2. To further develop this coating technology, and ultimately optimize its hemocompatible and antithrombotic functionality, it becomes imperative to probe each individual coating layer (outlined in Figure 2) and assess composition, uniformity, and thickness. To this end, a combination of qualitative and quantitative chemical characterization techniques were used; specifically, SEM imaging, X-Ray Photoelectron Spectroscopy (XPS), spectroscopic ellipsometry, focused-ion beam (FIB) milling, and confocal microscopy imaging. Additionally, to assess the hemocompatibility and thrombogenicity of the developed coating technology, in-vitro testing using the Calibrated Automated Thrombogram (CAT) Assay and in-vivo testing using porcine and primate models were performed. To gain more insight into the longitudinal stability of the bioactive component hTM, a longitudinal evaluation of the thrombogenicity of hTM coated devices via the CAT Assay after storage on the shelf at ambient temperature and pressure was performed.

Characterization of the Al₂O₃ Layer

To provide qualitative insights into the conformality of the coating technology's initial Al₂O₃ layer, at a macroscopic scale relative to the individual wires of a commercially available intracranial stent or flow diverting device, SEM imaging was used. In SEM imaging an electron gun generates electrons, which are focused into a beam, and accelerates them to an energy in the typical range of 0.1-30 keV toward a specimen of interest.⁶³ When the electron beam interacts with the specimen (to a depth of approximately 1 μ m) many types of signals containing information about the specimen's surface topography and composition are generated, the most common of which are secondary electron and backscattered electron signals.⁶³ For instance, by rastering the electron beam across the specimen and collecting the number of secondary electrons emitted (or low energy electrons ejected from the k-shell of

specimen atoms by inelastic scattering interactions with the electron beam) an image depicting the topography of the surface is created.⁶³ In contrast, rastering the electron beam and collecting the number of backscattered electrons (or high energy electrons originating from the electron beam but ultimately reflected away due to elastic scattering interactions with the specimen atoms) generates images with contrast indicative of chemical composition, since heavy elements backscatter electrons more strongly than lighter elements; strong topographic contrast can also be generated by using a directionally-dependent backscatter electron detector.⁶³ In other words, contrast in a SEM image is the result of spatial changes in signal intensity (or detected electrons) from the beam-specimen interaction as a result of either changes in specimen surface topography or chemical composition.⁶³ It should also be noted that image magnification in SEM is the ratio between the length of the raster on the viewing screen and the corresponding length on the specimen; when increased magnification is desired, the scan coils deflect the electron beam across a smaller distance on the sample.⁶³ Furthermore, the image sharpness and feature visibility in SEM are dependent upon the electron probe size, current, and convergence angle on the sample, as well as the electron beam accelerating voltage.

For the SEM imaging of the coating technology's initial Al_2O_3 layer, the Hitachi S-4800 instrument (Hitachi, Tokyo Japan) in the University of Iowa's Central Microscopy Research Facilities (CMRF) was used – a mixture of backscattered and secondary electrons were detected in this case to create images with strong topographic contrast using an accelerating electron beam voltage of 3.0 kV. Specifically, SEM imaging was done on an uncoated commercial flow diverting device #1, and also on a commercial flow diverting device #1 coated with 300 cycles of PE-ALD deposited Al_2O_3 – the acquired images are shown in Figure 9.

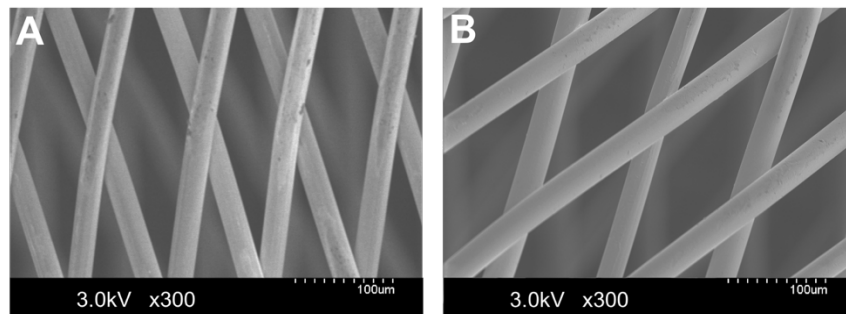


Figure 9: (A) SEM image of an uncoated commercial flow diverting device #1. (B) SEM image of a commercial flow diverting device #1 coated with 300 cycles of PE-ALD deposited Al_2O_3 .

Figure 9B shows that, at least qualitatively, the PE-ALD deposition of aluminum oxide does not significantly change the wire thickness of commercial flow diverting device #1, nor does it significantly alter the device's mesh size; in other words, it appears that the aluminum oxide coating is macroscopically conformal to the device #1 wires. Furthermore, Figure 9B reveals that the deposited Al_2O_3 coating seems to cover device #1 wire surface scratches and smooth the wire surface. This is in direct contrast to a coating of copolymer poly(lactic-co-glycolic acid) or PLGA, that was sprayed on a commercial flow diverting device #1, and lacked conformality to the device wires. Specifically, this coating formulation consisted of PLGA 50:50 (PLGA comprised of 50% lactic acid and 50% glycolic acid) dissolved in dichloromethane (DCM) in a 2% w/v solution. Glycerol and polyethylene glycol 200 (PEG, with an average molecular weight of 200) were used as surfactants. This formulation was then sprayed on a flow diverting device #1 via a nebulizer. SEM images of the spray-coated device and an uncoated, bare device #1 were acquired and are shown in Figure 10.

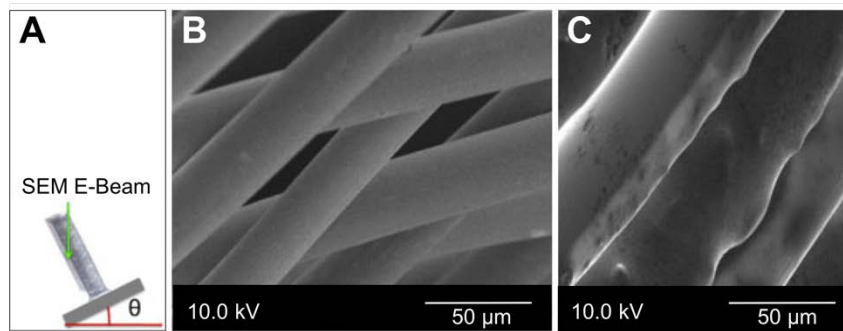


Figure 10: (A) Schematic of the flow diverting device #1 orientation on the SEM stage during image acquisition. (B) Acquired SEM image of an uncoated commercial flow diverting device #1. (C) Acquired SEM image of a commercial flow diverting device #1 spray coated with PLGA 50:50 in DCM (2% w/v solution), with glycerol and PEG 200 as surfactants.

Figure 10C reveals that the PLGA spray coating significantly alters the wire thickness of the commercial flow diverting device #1, in addition to decreasing the device's mesh size; in other words, it appears that the PLGA spray-coating is not conformal to the device wires, at least in the macroscopic sense. Manual manipulations of devices coated in this manner indicated increased device stiffness; hence work on optimizing this spray-coating formulation was stopped in favor of pursuing the layer-by-layer coating technology outlined in Figure 2 and discussed herein.

To assess the chemical composition and uniformity of the coating technology's initial Al_2O_3 layer, X-Ray Photoelectron Spectroscopy (XPS) was used. XPS was first

developed in the mid-1960s by Dr. Kai Siegbahn at the University of Uppsala, Sweden; in 1981 Dr. Siegbahn was awarded the Nobel Prize in Physics for his development of XPS.⁶⁴ In XPS, analysis of the sample surface is accomplished by irradiating it with monoenergetic x-rays in vacuum, which cause surface electrons (from the top 10 nm) to be emitted as a result of the photoelectric effect.⁶⁴ Analysis of the kinetic energies of the detected electrons enables calculation of the corresponding electron binding energies. Since each element has a unique set of binding energies, XPS can be used to identify elements on the sample surface, as well as determine their relative concentration.⁶⁴ Furthermore, the chemical state of a sample's surface elements can be determined through XPS by identifying characteristic shifts in binding energy.⁶⁴ With XPS it is also possible to generate intensity maps of the elemental composition of the sample surface. This is done by directing the irradiating x-rays through an aperture and limiting the detection electron spectrometer to output only the signal from electrons detected within an energy range characteristic of an element of interest.⁶⁴ Elemental intensity maps like these give a sense for the uniformity of surface elements on a sample.

In order to use XPS to assess the chemical composition and uniformity of the coating technology's initial Al₂O₃ layer, XPS data on the chemical composition of an uncoated device was first acquired to give insight into the underlying device composition – this was done on an uncoated commercial flow diverting device #1 using the Kratos Axis Ultra instrument (Kratos Analytical, UK) in the University of Iowa's CMRF. Specifically, a monochromated Al K α source was used with a pass energy of 160 eV to interrogate the uncoated device #1 surface and to acquire the survey scan, shown as Figure 11. After Figure 11 was calibrated relative to the carbon 1s (C 1s) peak, the relative atomic concentrations (At%) were calculated from the peak areas and the atomic sensitivity factors provided by the manufacturer, shown as inserts within Figure 11.

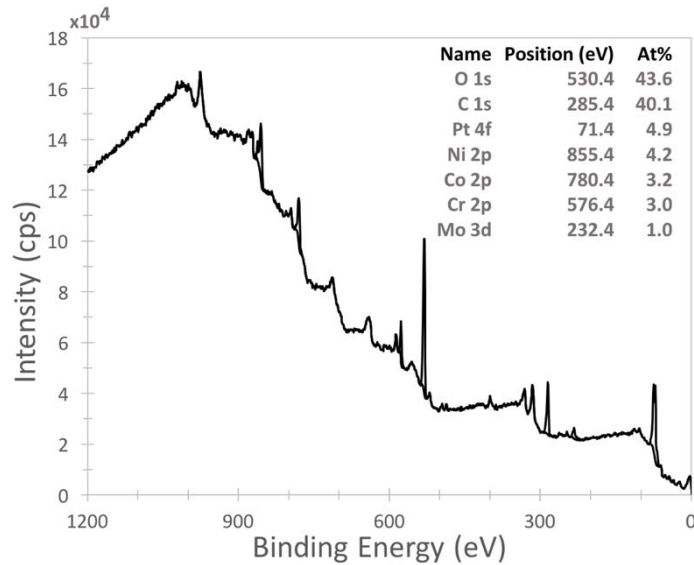


Figure 11: The acquired XPS survey scan on an uncoated commercial flow diverting device #1.

Figure 11 indicates that the metals present – and their electronic states – in an uncoated flow diverting device #1 are nickel (Ni 2p), platinum (Pt 4f), cobalt (Co 2p), chromium (Cr 2p), and molybdenum (Mo 3d). Since the Al K α beam source sampling area was 300x700 square microns in this acquisition and all those subsequent, the beam will interact with both the device wires and the area between wires (since the commercial flow diverting device #1 wire diameter is approximately 30 microns); thus, all XPS scans on these devices will detect some background carbon and oxygen electrons from the areas between device wires. Nevertheless, these results support information released by the device manufacturer, who state that device #1 is a bimetallic design consisting of 25% platinum-tungsten and 75% cobalt-chromium – though the specific alloy compositions of each is not publically available.⁶⁵ To assess the uniformity of the elemental composition of the commercial flow diverting device #1, XPS elemental intensity maps were acquired for the component metals (cobalt (Co 2p), chromium (Cr 2p), nickel (Ni 2p), platinum (Pt 4f) and tungsten (W 4f)) and are shown as Figure 12.

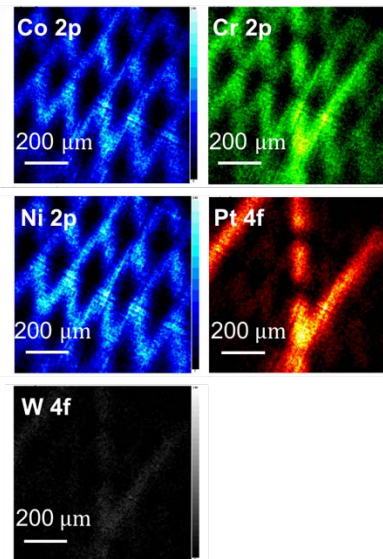


Figure 12: The XPS elemental intensity maps acquired for the component metals of an uncoated commercial flow diverting device #1.

Figure 12 indicates that cobalt, chromium, and nickel seem to be prevalent across the entire #1 device surface, while platinum and tungsten comprise only certain wires of the device. This also supports the literature on device #1 composition provided by the manufacturer, but further suggests that nickel is alloyed with both platinum-tungsten and cobalt-chromium.⁶⁵ With information on the underlying device composition at hand, XPS was next used to assess the chemical composition and uniformity of the coating technology's initial Al₂O₃ layer. Again the monochromated Al K α source was used with a pass energy of 160 eV to interrogate a commercial flow diverting device #1 surface coated with 300 cycles of PE-ALD deposited Al₂O₃ to acquire the survey scan, shown as Figure 13 with the relative atomic concentrations (At%) shown as a figure insert.

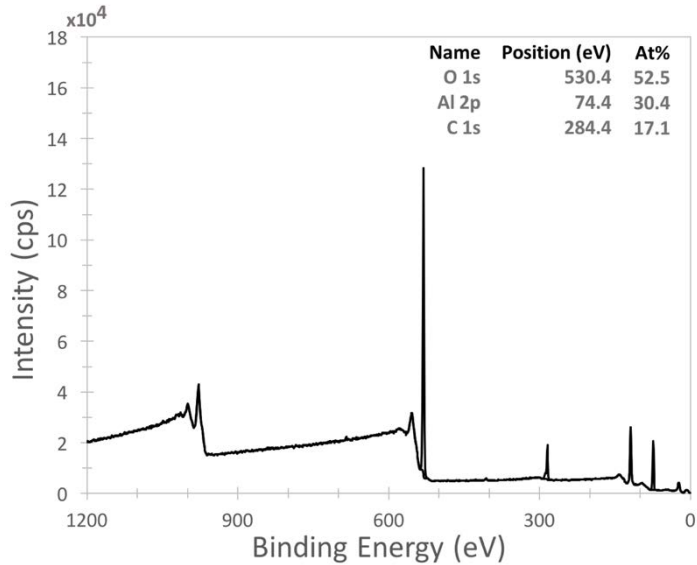


Figure 13: The acquired XPS survey scan on a commercial flow diverting device #1 coated with 300 cycles of PE-ALD deposited Al_2O_3 .

Figure 13 indicates that aluminum (Al) and oxygen (O), characteristic of Al_2O_3 , are the primary surface elements on the PE-ALD coated flow diverting device #1. Since none of the energy peaks characteristic of the metals comprising the underlying device show up in Figure 13, it can be deduced that the Al_2O_3 coating deposited by PE-ALD is thicker than 10 nm, or the approximate maximal depth that XPS can detect electrons from. To supplement this data, XPS elemental intensity maps were acquired for this Al_2O_3 coated device #1 and are shown in Figure 14.

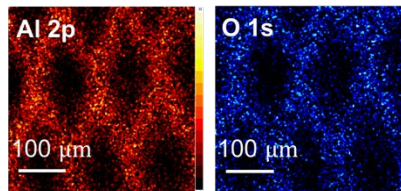


Figure 14: The XPS elemental intensity maps acquired for a flow diverting device #1 coated with 300 cycles of PE-ALD deposited Al_2O_3 .

Figure 14 indicates that the initial PE-ALD deposited Al_2O_3 layer of the developed coating technology is uniform across the device #1 surface. This indication is supported by the lack of defects noted in the SEM image (Figure 9B) of a different PE-ALD coated device #1.

In addition, focused ion beam (FIB) milling was used to etch through the initial PE-ALD deposited Al_2O_3 layer on a flow diverter device to further evaluate the uniformity

of the Al_2O_3 layer thickness. The FIB technique, most widely used in the material sciences and the semiconductor industry, uses a finely focused ion beam (usually gallium, or Ga^+) to create nanostructured surfaces; more recently FIB milling has been used to erode biological material to expose subsurface structures.⁶⁶ In general, FIB generates and directs a stream of high-energy ions from a massive element like Ga^+ onto a sample.⁶⁷ Collisions of the heavy ions with the sample surface atoms can result in the release of these atoms from the surface, a process called sputtering or milling.⁶⁷ Alternatively the interaction of the heavy ion beam with the sample can result in a transfer of energy and associated release of secondary electrons that could be detected to form an image, or else the deposition of atoms or molecules into the sample surface from a gaseous layer above the sample.⁶⁷ In this case, the sputtering capability of FIB was utilized to etch through the deposited Al_2O_3 layer on a commercial flow diverting device #2. However, since the etching process is destructive, platinum metal was initially deposited – through both electron beam and ion beam processes – on top of the deposited Al_2O_3 layer to help preserve its integrity during etching; next a rectangular etch was made by FIB on a single device wire at 5.0 kV accelerating voltage, cutting through both the platinum and Al_2O_3 layers. To visualize the cross-section, and the uniformity of the Al_2O_3 layer therein, SEM imaging was used. The SEM images of the rectangular wire etch and the corresponding Al_2O_3 layer cross-section are shown in Figure 15. It should be noted that while I coated this commercial flow diverting device #2 at the University of Iowa, the FIB and SEM imaging were both done by a specialist in the Laboratory of Advanced Electron Microscopy at the University of Notre Dame using a Helios Dual Beam FIB system (FEI, USA).

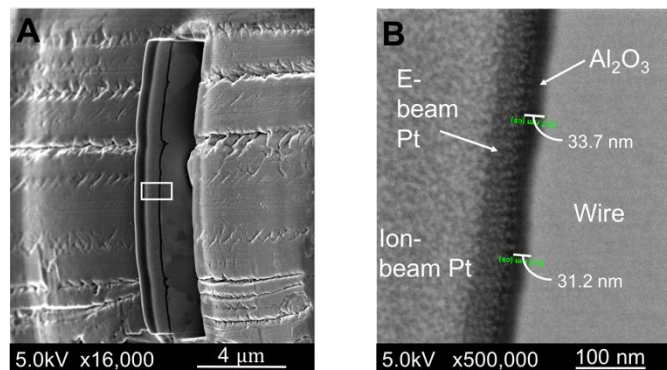


Figure 15: (A) SEM image of the FIB rectangular etch on a single wire of a commercial flow diverting device #2 coated with 300 cycles of PE-ALD deposited Al_2O_3 and platinum (Pt), the white box denotes the approximate location of the SEM cross-sectional image shown to the right. (B) SEM cross-sectional image of a portion of the FIB etch.

The SEM cross-sectional image shown as Figure 15B indicates that the Al_2O_3 coating is conformal to the device #2 wire in the small exposed area; additionally, the Al_2O_3 layer is uniformly deposited without holes in this particular area of the device. An image-processing software was used to measure the Al_2O_3 layer thickness from the SEM image in Figure 15B; as indicated therein, the two thickness measurements made by the specialist at University of Notre Dame were 33.7 nm and 31.2 nm. I obtained Al_2O_3 layer thickness measurements on an M-2000 spectroscopic ellipsometer (J.A. Woollam Co., USA) at 10 discrete locations on p-doped silicon wafers coated with 300 cycles of Al_2O_3 ($n=10$) deposited by PE-ALD. The Al_2O_3 layers on these wafers were found to be 31.86 ± 0.26 nm, which are similar to the 33.7 nm and 31.2 nm layer thickness measurements determined on the Al_2O_3 coated device #2 via FIB milling and SEM image acquisition and analysis. Finding the initial coating technology's Al_2O_3 layer to be approximately 30 nm thick is further supported by the XPS data (Figures 13 and 14) which indicate the Al_2O_3 layer to be at least 10 nm thick.

Characterization of the APTES Layer

XPS was next used to assess the chemical composition and uniformity of the coating technology's APTES layer, which acts as an intermediary layer for the attachment of the coupler TCT and ultimately hTM. To acquire the survey scan, a monochromated Al $K\alpha$ source was used with a pass energy of 160 eV to interrogate a commercial flow diverting device #1 surface coated with 300 cycles of PE-ALD deposited Al_2O_3 and the silane APTES, shown as Figure 16 with the relative atomic concentrations (At%) shown as a figure insert.

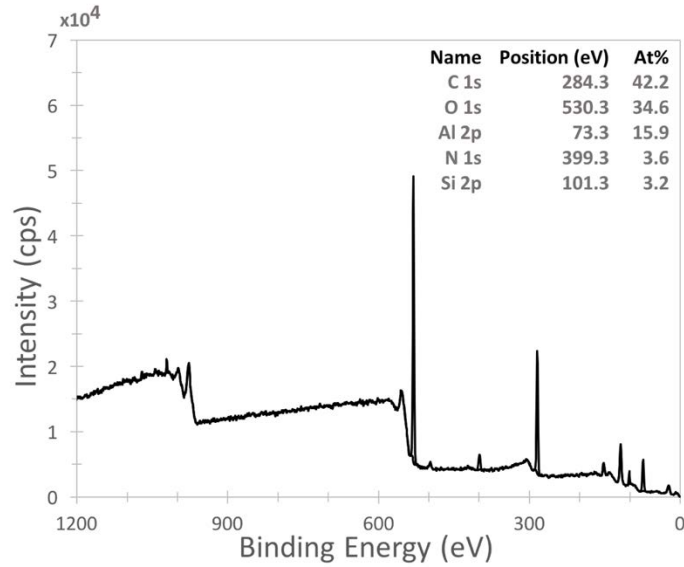


Figure 16: The acquired XPS survey scan on a commercial flow diverting device #1 coated with 300 cycles of PE-ALD deposited Al_2O_3 and the silane APTES.

Figure 16 indicates that silicon (Si) and nitrogen (N), characteristic of APTES, are present on the device #1 surface; furthermore, electrons from the Al_2O_3 layer are still detected. Together this indicates that the APTES layer is thin; specifically, it is less than 10 nm thick. To supplement this data, XPS elemental intensity maps were generated and are shown in Figure 17.

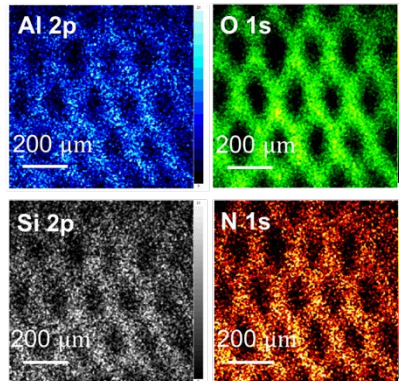


Figure 17: The XPS elemental intensity maps acquired for a commercial flow diverting device #1 coated with 300 cycles of PE-ALD deposited Al_2O_3 and the silane APTES.

Like the elemental maps for the aluminum oxide layer, the elemental maps shown in Figure 17 indicate that the silane layer is uniform across the device #1 surface. Furthermore Figure 17 indicates that the APTES layer is thin since the signal from the underlying aluminum oxide layer is strong.

Characterization of the TCT Layer

Like the Al_2O_3 and APTES layers, XPS was used to assess the chemical composition and uniformity of the coating technology's TCT layer, which acts as a coupler layer for hTM. To acquire the associated survey scan, a monochromated Al $K\alpha$ source was used with a pass energy of 160 eV to interrogate a commercial flow diverting device #1 surface coated with 300 cycles of PE-ALD deposited Al_2O_3 , the silane APTES, and TCT. This survey scan is shown as Figure 18, with the relative atomic concentrations (At%) shown as a figure insert.

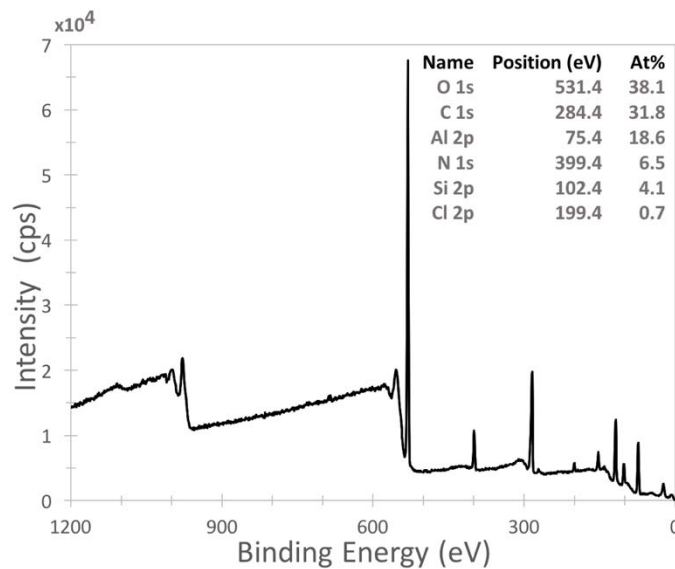


Figure 18: The acquired XPS survey scan on a commercial flow diverting device #1 coated with 300 cycles of PE-ALD deposited Al_2O_3 , the silane APTES, and the TCT coupler.

Figure 18 indicates that chlorine (Cl) and nitrogen (N), characteristic of TCT, are present on the device surface; furthermore, electrons from both the Al_2O_3 and APTES layers are detected. This indicates that the combined APTES and TCT layer is thin since electrons from both the Al_2O_3 layer and APTES layer are still detected; specifically, it is less than 10 nm thick. This finding is consistent with ellipsometry thickness measurements of the combined APTES and TCT layer I took using an M-2000 spectroscopic ellipsometer at 10 discrete locations on p-doped silicon wafers coated with 300 cycles of Al_2O_3 deposited by PE-ALD, APTES, and TCT (n=10). The combined layer was found to be 1.59 ± 0.14 nm thick. To supplement this data, XPS elemental intensity maps were generated for the TCT coated device #1 and are shown in Figure 19.

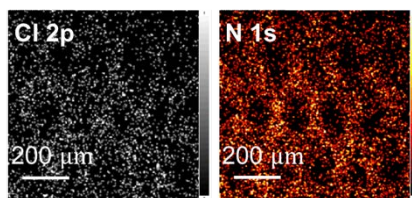


Figure 19: The XPS elemental intensity maps acquired for a commercial flow diverting device #1 coated with 300 cycles of PE-ALD deposited Al_2O_3 , the silane APTES, and the TCT coupler.

The XPS elemental maps in Figure 19 indicate a uniform distribution of TCT on the device #1 surface. However, when comparing these chlorine and nitrogen signals to the silicon and nitrogen signals characteristic of the APTES layer, shown in Figure 17, the chlorine and nitrogen signals from the TCT layer are weaker and more diffuse. While it should be noted that the abundances of chlorine and nitrogen and the TCT molecule is low relative to carbon and hydrogen and therefore a more diffuse signal is theoretically warranted, a diffuse signal may also indicate that the attachment of TCT to APTES in this coating technology could be optimized. Nevertheless, it is known that the XPS $\text{Al K}\alpha$ beam source degrades chlorine, so this is likely an additional contributor to the decreased chlorine signal intensity alone.⁶⁴

Since the TCT layer is the last layer deposited prior to the attachment of the bioactive component hTM, SEM imaging of this layer was done to provide qualitative insights into the layer uniformity, since this will likely impact hTM attachment. To perform the imaging, the Hitachi S-4800 instrument in the University of Iowa's CMRF was used; in this case, a mix of backscattered and secondary electrons were detected to create images with strong topographic contrast. An accelerating electron beam voltage of 1.0 kV was used for acquisition since this voltage produced images with optimal contrast given the addition of the Al_2O_3 , APTES, and TCT coating layers, which when combined act as insulators between the interaction of the SEM electron beam and the metallic wires of the underlying device. Specifically, SEM imaging was done on a commercial flow diverting device #5 coated with 300 cycles of PE-ALD deposited Al_2O_3 , the silane APTES, and the coupler TCT – the acquired images are shown as Figure 20.

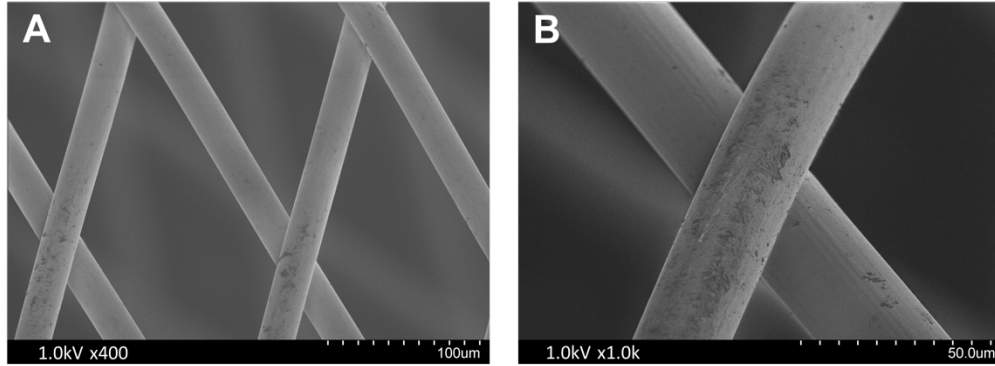


Figure 20: (A) SEM image of a commercial flow diverting device #5 coated with 300 cycles of PE-ALD deposited Al_2O_3 , the silane APTES, and the TCT coupler at 400X magnification. (B) The same device imaged at 1000X magnification.

Figures 20A and 20B indicate that the coating technology's TCT layer is not completely uniform; rather, it is possible for localized defects to exist. As a result, it is possible for these localized defects to impact the attachment of the bioactive hTM.

Characterization of the hTM Layer

As done with the Al_2O_3 , APTES, and TCT layers, XPS was used to assess the chemical composition and uniformity of the coating technology's bioactive hTM layer. To acquire the survey scan, a monochromated Al $K\alpha$ source was used with a pass energy of 160 eV to interrogate a commercial flow diverting device #1 surface coated with 300 cycles of PE-ALD deposited Al_2O_3 , the silane APTES, the coupler TCT, and hTM. This survey scan is shown as Figure 21 with the relative atomic concentrations (At%) shown as a figure insert.

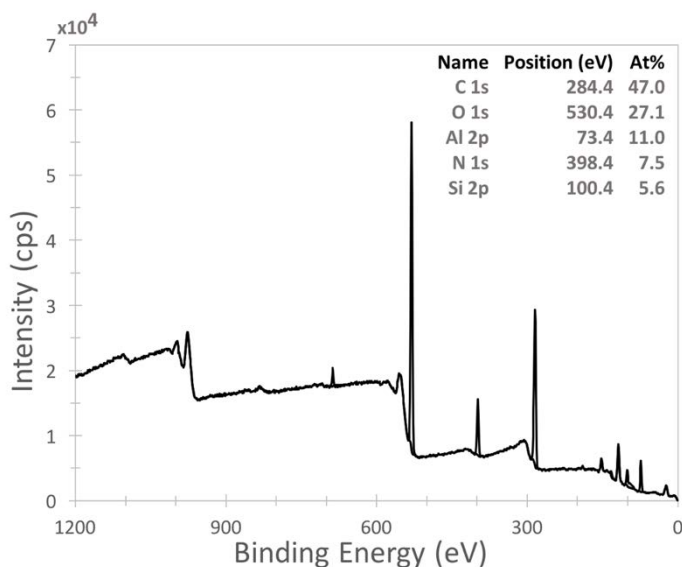


Figure 21: The acquired XPS survey scan on a commercial flow diverting device #1 coated with 300 cycles PE-ALD deposited Al_2O_3 , the silane APTES, the coupler TCT, and the bioactive hTM.

The decreased signal intensity of the aluminum peak in Figure 21 (or Al 2p with At = 11.0%), as compared to the aluminum peak in the TCT layer survey scan (Figure 18, Al 2p At = 18.6%) suggests the presence of some kind of overlayer; however, since the hTM layer contains no characteristic elements, or elements not found in any of the underlying layers, it is impossible to verify the presence of hTM on the coated device #1 surface from the XPS survey scan alone. As a result, XPS core level data was acquired for the element nitrogen, shown as Figure 22A, and compared to the core level nitrogen scan acquired on a TCT coated device #1, shown as Figure 22B – this is because, in theory, the nitrogen binding chemistry will change at the device surface with the attachment of hTM. Specifically, these core level scans were taken with a pass energy of 20 eV using the same monochromated Al $K\alpha$ source. After the scan peaks were subtracted from the baseline signal, they were assumed to have Gaussian line shapes and were resolved into individual components by a non-linear least squares procedure.

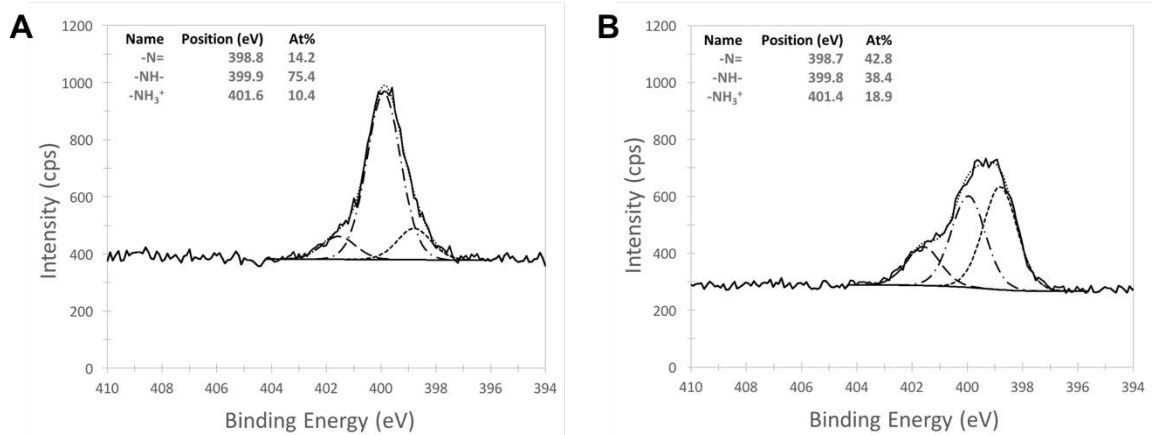


Figure 22: (A) The acquired XPS core level scan for nitrogen taken on a commercial flow diverting device #1 coated with 300 cycles PE-ALD deposited Al_2O_3 , the silane APTES, the coupler TCT, and the bioactive hTM. (B) The acquired XPS core level scan for nitrogen taken on a commercial flow diverting device #1 coated with 300 cycles PE-ALD deposited Al_2O_3 , the silane APTES, and the coupler TCT.

Figure 22 indicates that the nitrogen binding chemistry changes for the hTM coated device #1; specifically, Figure 22A indicates that the number of $-\text{NH}$ bonds doubles for the hTM coated device (75.4% vs. 38.4% in Figure 22B), which is consistent with surface attached protein; likewise, the number of $-\text{N}=\text{}$ bonds, characteristic nitrogen binding chemistry of the TCT molecule, decreases by more than half for the hTM coated device (14.2% vs. 42.8% in Figure 22B). Together this information indicates that some hTM protein is covalently attached, or conjugated, to the device surface. Because the hTM layer contains no characteristic elements, XPS elemental intensity maps were not acquired for the hTM coated device #1.

Nevertheless, to further assess the conjugation of hTM to the TCT layer, confocal microscope imaging of a hTM-fluorophore labeled commercial flow diverting device #1 was performed using the Alexa Fluor 488 5-TFP fluorophore, purchased from Sigma-Aldrich. In confocal imaging, the out-of-focus light emerging from above and below the microscope's focal plane is removed, increasing both axial and lateral image resolution – in this imaging modality the focal plane can also be easily changed, allowing for images to be acquired throughout the thickness direction of 3D objects.⁶⁸ As a result, confocal imaging was chosen to assess the conjugation of hTM to the TCT layer, both inside and outside, of a commercial flow diverting device #1. Since a fluorophore specific to hTM could not be found, a non-specific fluorophore, or Alexa Fluor 488 5-TFP, was used for the imaging; in particular, Alexa Fluor 488 5-TFP non-specifically reacts with the primary amines of biomolecules. Given this, a TCT coated device #1 was exposed to the same

fluorophore as a control. For the fluorophore-labeling reaction, 1 mg fluorophore was first dissolved in 500 μl dried dimethylformamide (DMF), protected from light. Both TCT and hTM coated device pieces (approximately 6 mm in length) were then placed into individual wells of a flat-bottom 96 well microplate and incubated in 250 μl of fluorophore-dried DMF solution in the dark for one hour at room temperature. A microplate shaker, set at moderate speed, was used to stir the fluorophore-dried DMF solutions during the incubation period. Afterward the device pieces were transferred to sterile plastic test tubes and washed with dried DMF three times; they were then dried under nitrogen stream and imaged with confocal microscopy while oriented horizontally. The acquired confocal images are shown as Figures 23A-23D. The autofluorescent-capability of a bare commercial flow diverting device #1 was also tested and is shown in Figure 23E. All confocal imaging was done at 10X magnification on a SP8 STED Super Resolution Microscope (Leica, USA) housed within the University of Iowa's CMRF. To acquire images of the interior device surfaces of both the control (Figure 23B) and hTM labeled (Figure 23D) devices, the focal plane of the SP8 microscope was changed such that images were acquired throughout the entire wire diameter (approximately 30 μm) of the wire mesh closest to the laser source.

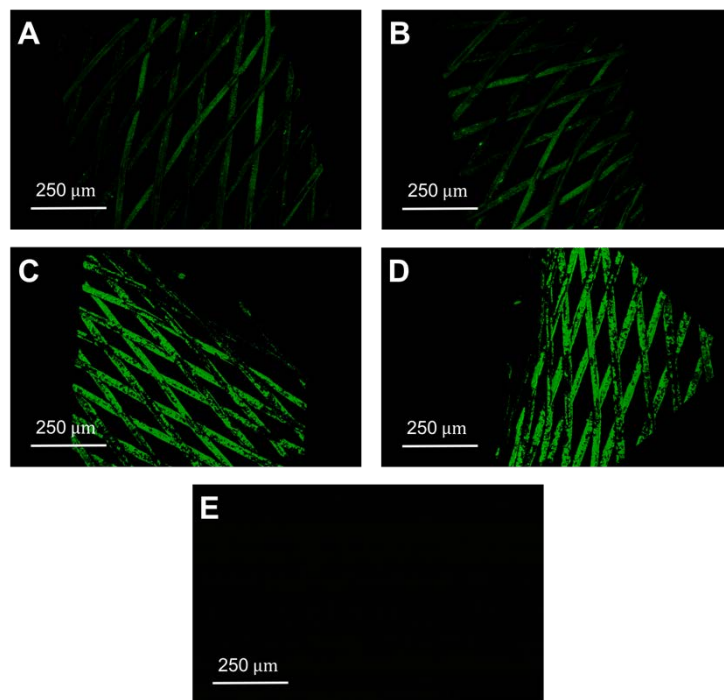


Figure 23: Confocal images (all at 10X magnification) of the (A) exterior and (B) interior of a TCT coated commercial flow diverting device #1. (C) The exterior and (D) interior of a hTM coated #1 flow diverting device. (E) The autofluorescent capability of an uncoated #1 device.

These confocal images indicate substantive hTM immobilization on both the interior (Figure 23D) and exterior surfaces (Figure 23C) of the hTM labeled device #1. The relatively diminished and inconsistent fluorescent signal associated with the TCT labeled device #1 (Figures 23A and 23B) is likely the result of the fluorophore reacting with either unreacted APTES or TCT on the coated device surface. Furthermore, uncoated #1 flow diverting devices exhibit no auto-fluorescence (Figure 23E). Collectively this data suggests that the developed coating technology allows for a relatively uniform conjugation of hTM on a TCT functionalized flow diverting device #1 surface, despite localized defects that may be present in this underlying TCT layer.

In-vitro Assessment of Hemocompatibility and Antithrombotic Functionality

To assess the hemocompatibility and antithrombotic functionality of the developed coating technology, the Calibrated Automated Thrombogram (CAT) Assay was used to measure in-vitro thrombin generation; this assay was originally developed by Hemker et al.¹⁷ and is currently purveyed by Thrombinoscope (Maastricht, Netherlands). This assay utilizes a fluorogenic substrate specific to thrombin; in particular, this substrate is added to a mixture of re-calcified human platelet-rich plasma (PRP) and the drug (or in this case, device) of interest; when cleaved by thrombin, the substrate fluoresces. The resulting signal can be measured by a 390 nm excitation/460 nm emission filter set on a microplate reader; this time-varying fluorescence data can then be mathematically converted to individual thrombin generation time courses.⁶⁹ The CAT assay protocol used to assess the developed coating technology was adapted from that given by Thrombinoscope for testing soluble drugs.⁷⁰ Using this assay to evaluate biomedical device thrombogenicity in-vitro is a new idea. In fact, Medtronic published using this assay to measure thrombin generation in clotting plasma exposed to coated intracranial devices in 2015²⁰; to the best of our knowledge, we are only the second group to report using the CAT assay to evaluate the hemocompatible and antithrombotic functionality of coated intracranial devices. Nevertheless, to understand why the CAT assay was chosen for the in-vitro evaluation of this developed coating technology, one first must understand how coagulation is initiated and controlled in-vivo.

The Coagulation Cascade

The coagulation cascade is an enzymatic cascade of proenzyme activations ultimately leading to the conversion of prothrombin to thrombin.⁷¹ Thrombin, in turn, converts fibrinogen to fibrin, a polymer which forms the clot.⁷¹ Fibrin is then cross-linked and stabilized by the active form of factor XIII, or factor XIIIa.⁷¹ Specifically, the coagulation cascade begins in-vivo when an injured blood vessel wall exposes blood to cells underneath the endothelial layer, or cells expressing tissue factor (TF) on their cell membranes.¹⁷ Next, the expressed TF complexes with factors VII and VIIa (TF-VIIa) and this complex activates factor IX to factor IXa and factor X to factor Xa.¹⁷ Once activated, factor Xa converts prothrombin to thrombin.¹⁷ Initially, only a small amount of thrombin is generated, as its generation is ultimately suppressed by tissue factor pathway inhibitor (TFPI). This suppression occurs because TFPI can complex with factor Xa (Xa-TFPI), which inhibits the action of the TF-VIIa complex and, ultimately, the generation of more factor Xa. In addition to TFPI, thrombin is also inactivated by antithrombin (AT) when thrombin complexes with AT to form the T-AT complex and, to a lesser extent, by alpha2-macroglobulin (alpha2M) forming the T-alpha2M complex. The thrombin generation scheme can be seen in Figure 24, which was originally printed in Hemker and Beguin's 1995 article in the journal *Thrombosis and Haemostasis*.¹⁷

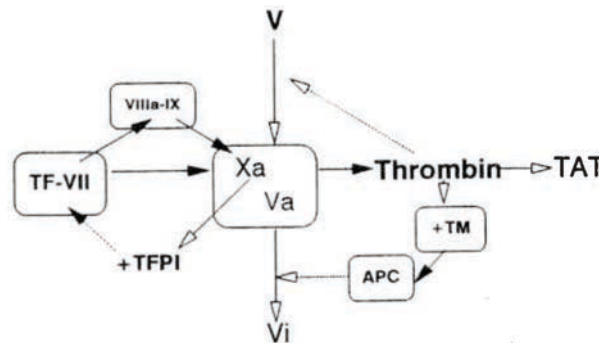


Figure 24: Thrombin generation scheme originally printed in Hemker and Beguin.¹⁷ Lines with open arrow heads indicate a chemical conversion; lines with black arrow heads indicate activation of a proenzyme; dotted lines with open arrow heads indicate an activating action and dotted lines with black arrow heads indicate an inhibitory action.

It should be noted that factor IX is activated to factor IXa by the TF-VIIa complex; as a result, when it complexes with factor VIIIa (IXa-VIIIa) it forms an alternative factor X activator not impacted by TFPI, but rather by the activation and inactivation of factor VIII.¹⁷ This is called the Jossen Reinforcement Loop and likely is the pathway whereby, at

low TF levels, the precocious arrest of factor Xa generation via TFPI is prevented.¹⁷ The conversion velocity of prothrombin to thrombin is modulated by factors V and VIII, as shown in Figure 24. Factors Va and VIIIa enhance the proteolytic activities of factors Xa and IXa, respectively, by approximately one thousand fold.¹⁷ However the generation and degradation of factors Va and VIIIa is governed by thrombin, so too is the activation and inactivation of factors Va and VIIIa.¹⁷ Factor V is activated by meizothrombin at a phospholipid cell membrane, whereas factor VIIIa is kept in solution by von Willebrand factor and activated by free thrombin in solution.¹⁷ Activated protein C, and its cofactor protein S, inactivate factors Va and VIII, leading to the down-regulation of the blood coagulation cascade.¹⁷ Protein C is activated when its inactive form and thrombin bind to the cell surface glycoprotein thrombomodulin.¹⁷

For in-vitro testing purposes, one can think of the coagulation cascade as having two separate initiation pathways, the intrinsic and extrinsic pathways. The division of coagulation initiation into two pathways originates from in-vitro laboratory testing that measured clotting times after initiation by glass (intrinsic pathway) or by a mixture of TF and phospholipid cofactors (extrinsic pathway).¹⁶ The extrinsic pathway is the primary pathway by which a clot forms in-vivo and is previously described.¹⁶ In contrast, the intrinsic pathway begins when kallikrein activates factor XII to factor XIIa, which in turn activates factor XI to factor XIa.¹⁶ Factor XIa activates factor IX and ultimately activates factor X.¹⁶ While the intrinsic pathway plays only a minor role in the formation of fibrin in-vivo (in the sense that patients with prekallikrein and factor XII deficiencies do not have bleeding disorders), it is involved in inflammation processes.¹⁶ The pathway common to both, or the common pathway, begins with the conversion of prothrombin to thrombin and ends with the stabilization of the fibrin clot by factor XIIIa.¹⁶ A schematic of the entire coagulation cascade is shown in Figure 25. The green lines in Figure 25 depict thrombin's many roles as a reaction catalyst, whereas the red lines depict the primary regulatory mechanisms that keep coagulation in check.

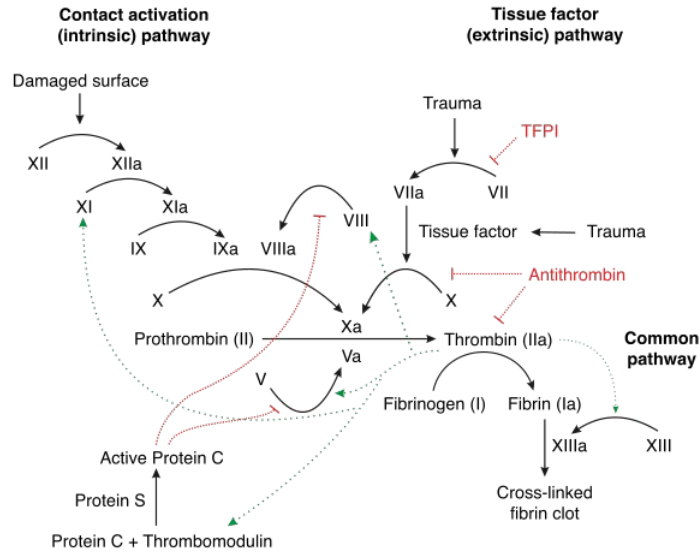


Figure 25: The coagulation cascade. Green lines depict the thrombin's roles as a reaction catalyst. Red lines depict the primary regulatory mechanisms that keep coagulation in check. Figure attributed to Wikimedia Commons and distributed under a CC-BY 3.0 License.

Coagulation is also mediated by a complex interaction with platelets. After vessel injury, and a brief period of arteriolar vasoconstriction, platelets begin to adhere to the injured endothelium and promote the aggregation of more platelets to the injury site, with the intent to produce a platelet plug to stop the bleeding.⁷² First platelets activate and adhere to the sub-endothelial collagen exposed by vessel damage.⁷² The platelets are able to adhere due to collagen-specific receptors on their surface.⁷² Platelet adhesion is strengthened by von Willebrand factor (vWF), which is released by the damaged endothelial cells and from the platelets themselves, and acts to form additional links between collagen and the platelet surface receptors.⁷² The adhered and active platelets then begin to recruit additional platelets to the injury site, ultimately forming an aggregate. They do so by releasing the contents of their alpha granules into the blood plasma, which include factors like ADP, serotonin, platelet-activating factor, vWF and thromboxane A₂.⁷² The release of these factors activates additional platelets and stimulates a G_q-linked protein receptor cascade that increases the concentration of calcium in the cytosol of platelets.⁷² The increased calcium level in platelets ultimately activates phospholipase A₂, which modifies platelet integrin membrane glycoprotein IIb/IIIa to bind fibrinogen.⁷² The fibrinogen crosslinks with glycoprotein IIb/IIIa and facilitates platelet aggregation.⁷² Upon activation, platelets also change shape from discoid to a spiny formation, which aids in platelet aggregation.⁷² It should also be noted that release of the platelet alpha granule contents into the blood plasma leads to a high

local concentration of procoagulant proteins, like fibrinogen and factors V, VIII, XI, and XIII, all of which support fibrin formation and stabilization.⁷² Finally because activated platelets contain the contractile proteins actin and myosin they are able to bind to fibrin strands in the clot and help draw them closer together, aiding in clot contraction and facilitating the movement of the injured tissue edges back together.¹⁶

It is vital that coagulation is controlled to ensure that blood clots will only form where needed. One control mechanism is the hepatic clearance of activated coagulation factors.⁷³ Additionally several coagulation inhibitors natively exist in blood plasma like AT, protein C, and TFPI, as shown in Figure 21. Specifically AT complexes with thrombin and blocks its active site; additionally it inhibits factors IXa, Xa, and XIa.⁷³ Protein C inhibits coagulation in its active form, activated protein C (APC), which is generated by the thrombin-thrombomodulin complex.⁷³ APC and its cofactor protein S degrade factors Va and VIIIa so that they no longer facilitate thrombin generation and factor Xa formation.⁷³ TFPI can complex with factor Xa (Xa-TFPI), which inhibits the action of the TF-VIIa complex and, ultimately, the generation of more factor Xa.¹⁷ It should also be noted that healthy endothelia cells promote anti-coagulation. For one, healthy endothelia facilitate APC formation by allowing the cell membrane glycoprotein thrombomodulin to complex with thrombin and activate protein C.⁷³ Healthy endothelia also secrete prostacyclin and nitric oxide, both of which are inhibitors of platelet activation and aggregation.⁷³ Furthermore tissue plasminogen activator (T-PA) is secreted by healthy endothelia.⁷³ T-PA is a catalyst for the cleavage of plasminogen to plasmin which cleaves fibrin and thereby inhibits excessive fibrin formation.⁷³

Knowing how the coagulation cascade works to produce and stabilize a fibrin clot can help guide a scientist or clinician to develop in-vitro methods to assess coagulation. In general, all the in-vitro coagulation assays that have been reported in the literature and used for clinical screening of coagulation protein defects examine the rate of clot formation.¹⁵ This means that they all initiate coagulation, thrombin generation, and ultimately fibrin clot formation. As a result soluble proteins are generated that are detected by either increased impedance or decreased optical clarity, based on the measurement instrumentation used.¹⁵ Any defect in the clotting process will manifest itself as a time delay in clot formation; this also means that the addition of any inhibitory antibody or anticoagulant will also effect the clot formation time.¹⁵ The three most common in-vitro assays to measure the rate of clot formation are the activated partial

thromboplastin time (aPTT), the prothrombin time (PT), and the thrombin clotting time (ThCT).¹⁵ The aPTT assay only assesses the functionality of the intrinsic and common coagulation pathway proteins; to perform this assay, equal parts of a negatively charged surface, a phospholipid mixture, and patient citrated-blood plasma are incubated.¹⁵ Calcium chloride is added, in a concentration of 30 mM, to recalcify the citrated plasma and the time to clot formation is then measured.¹⁵ In contrast, the PT assay only assesses the functionality of the extrinsic and common coagulation pathway proteins.¹⁵ In this assay either tissue-derived or recombinant TF is incubated with phospholipids and patient citrated-plasma.¹⁵ The plasma is then recalcified by adding calcium chloride (to a concentration of 30 mM) and the time to clot formation is measured.¹⁵ In contrast to the aPTT and PT assays, the ThCT assay directly measures the conversion of fibrinogen (soluble) to fibrin (insoluble). In the ThCT assay an excess of thrombin is added to patient citrated plasma and the clotting time is measured.¹⁵ It is important to realize that the aPTT and PT assays have different sensitivities for detection of coagulation abnormalities depending upon the factor tested, the commercial reagents used in the assay, as well as the measurement equipment used.¹⁵ Since the ThCT assay only measures the conversion of fibrinogen to fibrin, it is generally accepted that clotting times outside the 95% confidence interval of clotting times collected for a population of at least 20 donors suggests reduced fibrinogen levels, abnormal fibrinogen function, or the presence of a thrombin inhibitor.¹⁵ Rotational viscometry can also be used to measure time to clot formation; in fact the methodology, called the thromboelastography (or TEG), is not new and was pioneered by Hartert in 1948.¹⁹ Specifically the TEG measures the torque applied to a stationary pin (connected to a torsion wire) by whole blood or plasma in a heated viscometer during oscillating rotation.¹⁹ The torque measured is minimal in an unclotted sample, but increases during clot formation due to increased sample viscosity and clot-mediated bridge formation between the pin and the cup walls; this torque is increasingly transferred to the pin.¹⁹ There is currently insufficient evidence to prefer using TEG over other standard coagulation tests; particularly TEG estimates of fibrinogen have shown moderate to poor correlation to those observed in PT assays.¹⁹

The Calibrated Automated Thrombogram (CAT) In-Vitro Assay

Another metric that can be used to assess in-vitro coagulation is the amount of thrombin generated in a sample. This is because the traditional in-vitro assays that assess clot formation do not measure the sample's full thrombin generation capacity, since fibrin clots form early in the thrombin generation process when approximately 95% of thrombin has yet to form.¹⁹ Determining the extent of plasma's thrombin generation capacity is important; this is because thrombin is pivotal in the coagulation cascade and functionally can both amplify and dampen it.¹⁹ Specifically thrombin can amplify the cascade since it catalyzes the conversion of fibrinogen to fibrin, promotes increased thrombin formation through activation of factors XI, V, and VIII, promotes clot stabilization by activation of anti-fibrinolytic factors, activates damaged endothelia to synthesize factors like vWF and tissue plasminogen activator, as well as acts as a platelet activator.¹⁹ In contrast, thrombin can function to dampen the cascade when it complexes with hTM; this complex activates protein C, a prominent anticoagulant.¹⁹ Because of thrombin's vital role in the cascade, it is thought to be a metric predictive of a patient's thrombosis risk. In fact, thrombin generation assays in platelet-poor plasma (PPP) are sensitive to all clotting factor deficiencies, except for factor XIII; furthermore, they are sensitive to all anticoagulant drugs tested.¹⁸ They are also sensitive to a lack of AT, as well as resistance to proteins C, S, and APC, which manifest as increased thrombin generation.¹⁷ Thrombin generation assays in platelet-rich plasma (PRP) are sensitive to vWF, anti-platelet drugs, and agents that increase platelet reactivity.¹⁷ Despite the usefulness of such assays, their application has been limited mostly due to technical issues. This is because these assays traditionally measured thrombin generation by sub-sampling a clotting plasma sample, a labor and time-intensive methodology.¹⁷ However recent advances have enabled thrombin to be fluorescently tagged with a slow-binding substrate, facilitating a continuous and sensitive measurement of thrombin generation in clotting plasma over time.¹⁸ Furthermore, advances in software and instrumentation have contributed to the automation of large portions of the current assay workflow and allow for reproducible data collection outside of specialized labs.¹⁹

There are currently two commercially available fluorogenic thrombin generation assays – the Calibrated Automated Thrombogram (or CAT) developed by Hemker et al.¹⁸ and marketed by Thrombinoscope, a Stago Group Company based in Maastricht,

Netherlands and the Technothrombin TGA method marketed by Technoclone in Vienna, Austria.⁷⁴ While these assays differ in their technical details, both utilize a fluorogenic substrate specific to thrombin that is added to recalcified plasma (either PRP or PPP). When the substrate is cleaved by thrombin it fluoresces and the resulting signal is measured by a 390 nm excitation/460 nm emission filter set on a microplate reader; thus, thrombin generation is correlated to the signal intensity of a specific fluorophore.¹⁸ This signal takes the shape of a skewed-bell shape profile because native AT and alpha2M in the plasma inhibit thrombin formation and so the concentration of active thrombin eventually falls to a basal equilibrium level.⁷¹ Several important parameters can be measured from the free thrombin time course curve, which are lag time, peak thrombin concentration, time until peak thrombin concentration, and the endogenous thrombin potential (ETP). Lag time is taken as the time to first detectable free thrombin measurement.⁷¹ Peak thrombin is the maximum concentration of free thrombin generated over the course of the experiment; time to peak thrombin generation is the time from the first detectable free thrombin until the peak thrombin activity.⁷¹ ETP is the area under the free thrombin time curve.⁷¹ All of these parameters are shown in Figure 26.

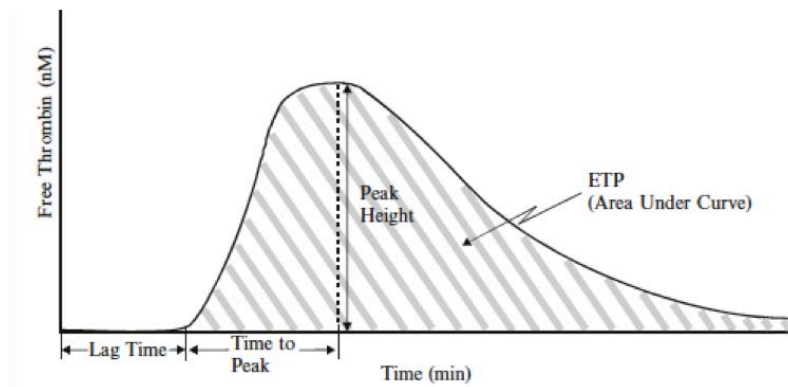


Figure 26: Thrombin generation time course in recalcified, activated plasma. Four major parameters are identified. Peak Height refers to peak thrombin concentration. Figure attributed to Berry and Chan's book *Haemostasis: Methods and Protocols*.⁷¹

The Technothrombin TGA and CAT assays have one important difference and that is that the CAT assay uses an internal standard to generate the free thrombin time course; in other words, the CAT assay allows for computation of free thrombin activity as a function of time by comparing the fluorescent signal of a thrombin generating sample to that from a known and stable concentration of thrombin that is measured simultaneously in a parallel plasma sample.¹⁸ Producing a constant and stable

fluorescent signal from a known thrombin concentration is not trivial; this is because thrombin is readily inactivated in plasma by AT and alpha2M, thus it cannot be used for calibration.⁶⁹ Instead the stable complex of thrombin-alpha2M is used as a calibrator in the CAT assay.⁶⁹ Furthermore because the fluorescent signal produced by the thrombin-alpha2M complex differs when incubated in buffer and plasma, the CAT assay carries out calibration by incubating the thrombin-alpha2M complex in the same plasma that is used to test the thrombin generating sample.⁶⁹ The use of an internal calibration standard is important in fluorogenic thrombin generation assays because the rate of fluorescent signal increase is not linearly related to the amount of thrombin produced in these tests. The reason for this is three-fold, first the fluorogenic substrate is consumed throughout the experiment so that as the reaction proceeds the velocity of fluorophore formation per unit substrate decreases (substrate consumption).⁶⁹ Second, the absorbance of either emission or excitation light by plasma elements prevents the equal excitation and capture of light from deeper in the assay liquid, meaning that fluorescence intensity is not linearly related with fluorophore concentration (inner filter effect).⁶⁹ Finally while it is known that alpha2M inhibits physiologic thrombin function it does not inhibit the thrombin-mediated cleavage of the substrate to its fluorogenic state, resulting in residual fluorescent signal that has no physiological relevance (alpha2M effect); this means that only the fluorescent signal from free thrombin (i.e. thrombin not bound to alpha2M) has physiological relevance.⁶⁹ Thus, the CAT assay uses its internal calibration standard as a means to adjust the free thrombin signal from a thrombin generating sample to account for discrepancies caused by substrate consumption, the inner filter effect, and the alpha2M effect. As a result, the CAT assay is superior in methodology to the Technothrombin TGA assay; hence it was chosen as the fluorogenic thrombin generation assay to test the developed coating technology.

Because no other research group at the University of Iowa has performed the CAT assay (past or present), the methodology and data analysis for the assay had to be determined independently. Specifically the assay methodology was pieced together from information contained in the *Thrombogram Guide*, a CAT methodology and software guide produced and distributed by Thrombinoscope⁷⁰ and is similar to the methodology published by Medtronic²⁰. To facilitate ease of use, the thrombin calibrator (or known amount of thrombin, our purchased calibrators have activity equivalent to 700 nM human thrombin), fluorescent substrate and buffer (including CaCl₂), and PRP reagent (or the recombinant TF trigger used to initiate thrombin generation in PRP) were

all purchased as part of a kit through Thrombinoscope, as were 50 Immulon 2HB 96-well microplates (U-bottom). The assay data analysis was done using the strategies outlined in H.C. Hemker and R. Kremers' 2013 paper *Data Management in Thrombin Generation*.⁶⁹

In-Vitro CAT Assay Assessment of Coating Technology Thrombogenicity

The developed CAT Assay protocol can be broken down into the three generic steps of PRP preparation, preparation of the test microplate, and collection of the associated kinetic fluorescence intensity measurements from a fluorometer. The PRP preparation step begins by collecting human whole blood into 3.2% sodium citrate using a 20 gauge needle (commensurate with the standard hospital blood collection procedure).⁷⁰ Within 30 minutes of blood collection the whole blood sample should be centrifuged in a swinging-bucket centrifuge to separate the PRP.⁷⁰ In the case of our thrombogram test, we purchased one unit of human whole blood (~450 mL) from a healthy single donor from the company ZenBio Incorporated (Triangle Park, North Carolina). We did this because it was not possible to collect whole blood from a donor at the University of Iowa on the same day as experimentation. We received the human whole blood from ZenBio one day post collection and ran a test thrombogram assay on this day. The test thrombogram assay consisted of running wells containing the thrombin calibrator, a suite of diluted thrombin calibrators (between 0-75% thrombin calibrator), blank wells (or wells containing PRP, PRP reagent, and fluorescent substrate only), wells containing glass shards (in addition to PRP, PRP reagent, and fluorescent substrate), and wells containing pieces of linear low-density polyethylene tubing (LLDPE, in addition to PRP, PRP reagent, and fluorescent substrate) in the fluorometer and collecting the corresponding kinetic signal intensity measurements. This unit of blood was stored at 2°C. The thrombogram assay testing coated flow diverting devices was run on day two post collection. To separate the PRP for our thrombogram assay, 100 mL of the whole blood unit was poured, under a sterile cell culture hood, into two plastic 50 mL centrifuge tubes. These tubes were centrifuged for 10 minutes between 18-20°C at 150 g in a swinging bucket centrifuge; following this, the blood was centrifuged again at the same temperature and speed for five minutes in order to maximize the supernatant that could be collected. The supernatant was then collected via Pasteur pipette cautiously, in order to avoid sucking up white cells from the buffy coat, placed in

a plastic test tube, and gently mixed – this is the PRP. Next 150 μL of this PRP was transferred to a small test tube and the platelet count was measured on the Sysmex XE-2100 CBC analyzer in the University of Iowa Medical Labs, which is the same model used clinically to measure human complete blood counts (CBC). The remaining PRP was stored in a tissue culture shaker at 37°C. After the PRP platelet count was recorded, approximately half of the PRP was pipetted into new plastic centrifuge tubes and spun again at 2000 g for 10 minutes at room temperature; this spinning was repeated for five minutes at the same speed and temperature to maximize the supernatant that could be collected. The supernatant was then pipetted off cautiously and transferred to a new plastic centrifuge tube – this is the PPP. This PPP was then used to adjust the PRP to approximately 150 platelets/nL and also stored in the tissue culture shaker at 37°C. To ensure the adjusted platelet count was approximately 150 platelets/nL, the platelet count of 300 μL of the adjusted PRP was measured via the Sysmex XE-2100 CBC analyzer (enough sample for n=3 platelet count measurements). After it was confirmed that the platelet count of the PRP was properly adjusted, the thrombogram test microplate was prepared. To do this one vial of the fluorescent substrate buffer (purchased from Thrombinoscope and called Fluo-Buffer) was warmed in a water bath for approximately 10 minutes; 10 mL of deionized (DI) water was also warmed in the bath. Once warm, 40 μL of fluorescent substrate (also purchased from Thrombinoscope and called Fluo-Substrate) was added to the Fluo-Buffer under the cell culture hood and was immediately vortexed, forming FluCa solution. To reconstitute the thrombin calibrator (purchased from Thrombinoscope), 1 mL of DI water was added to the vial. After 10 minutes, the thrombin calibrator vial was shook carefully; likewise to reconstitute the PRP reagent (purchased from Thrombinoscope) 1 mL of DI water was added to the vial under the cell culture hood and after 10 minutes the vial was shook carefully. The devices used in the assay were two commercial #2 flow diverting devices of size 5x26 mm. Because Thrombinoscope advises to run the CAT assay components in triplicate, the two #2 devices were cut into nine smaller pieces of approximately the same size (or about 4.3 mm in length) – three were coated with hTM, three were coated with TCT, and the remaining three were left uncoated (or left bare). Each device piece was then placed in a separate well of the 96-well microplate. Three small glass shards were broken from the tip of a sterile glass pipette under the cell culture hood and three similarly sized glass pieces were placed in individual wells; likewise, three small pieces of sterile LLDPE (purchased from Freelin-Wade), of similar size as the glass, were also

cut and placed in individual wells. Next the thrombin calibrators were added to the microplate. Undiluted calibrator, as well as calibrator diluted with PPP by 25%, 50%, 75%, and 100% were added to individual wells in 20 μ L aliquots, and in triplicate. Additionally, 5 μ L of the 0.02 mg/mL hTM-PBS solution that the hTM devices were incubated in was added to individual wells in triplicate. A schematic of the constituents of the microplate is shown as Figure 27.

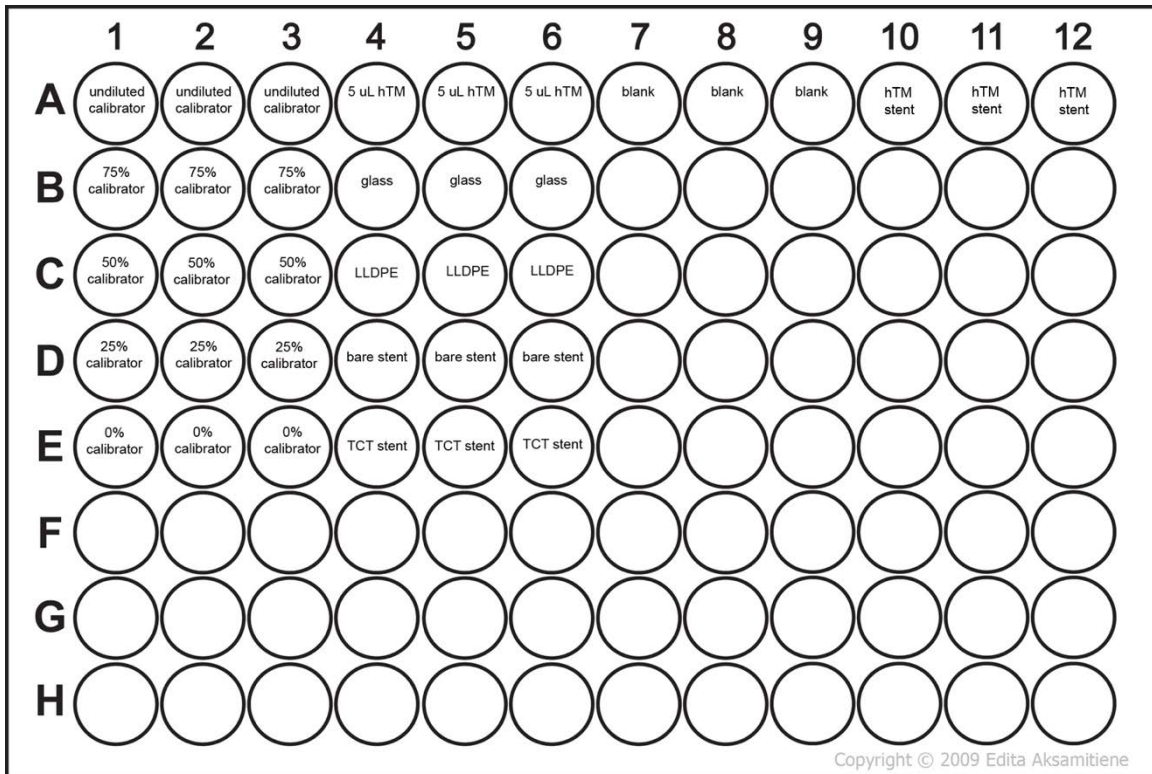


Figure 27: Constituents of the 96-well plate run in the in-house CAT assay. LLDPE refers to Linear Low-Density Polyethylene; hTM refers to the human recombinant thrombomodulin purchased from Sigma-Aldrich; TCT stent refers to device coated with every layer in the developed coating technology except the hTM layer; hTM stent refers to a device coated with every layer.

Next, 80 μ L PRP was added to each of the wells containing thrombin calibrator (wells in microplate columns 1-3 of Figure 27). Likewise 80 μ L PRP was added to the remaining wells; additionally, 80 μ L PRP reagent was added to these wells. The SpectraMax M5 fluorometer (Molecular Devices, USA) was turned on and allowed to warm to 37°C. After adding 20 μ L of FluCa to each well, the microplate was placed on a shaker for three minutes and then immediately placed in the fluorometer. The kinetic measurement was set to take a reading every 23 seconds for duration of one hour 15 minutes; the M5's excitation filter was set to 390 nm and the emission filter was set to 460 nm. After changing these settings, the kinetic measurement reading of the fluorescent signal from

thrombin commenced. After one hour 15 minutes, the data was outputted into a text file and saved.

To analyze the collected thrombin fluorescent signals from each well over time, the strategies outlined in H.C. Hemker and R. Kremers' 2013 paper *Data Management in Thrombin Generation* was used.⁶⁹ The general idea of the data analysis is to correct the experimentally measured thrombin calibrator signal intensities for the substrate consumption and inner filter effects by determining their ideal values, and to ultimately compute a value called the calibration factor from this corrected calibrator data. Once the calibration factor is known, it can be applied to the ideal, or corrected, fluorescence signal intensities from thrombin generating (i.e. unknown) samples, yielding a total ideal thrombin concentration integral for each. To account for the alpha2M effect on the unknown samples, the fluorescent signal corresponding to free thrombin alone is mathematically dissected from each total thrombin concentration integral. Equations can then be fitted to each total free thrombin concentration integral, the derivatives of which are the free thrombin generation time-courses for each unknown sample.

Regarding this data analysis, it should be mentioned that the raw fluorescent signal intensity data must to be properly organized. Natively the signal intensity data outputted from the SpectraMax M5 fluorometer is separated by time-point, as shown in Figure 28.

Time (hh:mm:ss)	Microplate Column		
	1	2	...
0:00:00	A1-0	A2-0	...
	B1-0	B2-0	...
	C1-0	C2-0	...
	D1-0	D2-0	...

0:00:23	A1-1	A2-1	...
	B1-1	B2-1	...
	C1-1	C2-1	...
	D1-1	D2-1	...

Figure 28: An example of the organization of the raw fluorescent signal intensity data outputted from the SpectraMax M5 fluorometer.

For analysis purposes the signal intensity data should be organized relative to microplate well, as shown as Figure 29.

Time (hh:mm:ss)	Microplate Well		
	1	2	...
0:00:00	A1-0	A2-0	...
0:00:23	A1-1	A2-1	...
0:00:46	A1-2	A2-2	...
0:01:09	A1-3	A2-3	...
0:01:32

Figure 29: An example of the organization of the raw fluorescent signal intensity data required for CAT assay data analysis.

As such, a MATLAB® computer code was written to transpose the raw signal intensity data such that it is organized relative to microplate well, or organized as shown in Figure 29. Once the data was organized in this manner all manipulations were done in Microsoft Excel. To start, each series of triplicate thrombin calibrator wells was averaged so that one average signal intensity (i.e. fluorescence) curve corresponded to the undiluted calibrator, as well as each diluted calibrator. Because of substrate

consumption and the inner filter effect, experimentally measured fluorescence curves, like those corresponding to thrombin calibrators, will stop increasing and eventually plateau even while enzymatic activity continues.⁶⁹ To correct for these two effects Hemker et al. developed a mathematical transformation called the H-Transform, which transforms the experimentally measured fluorescent signal into the signal that would be obtained if substrate consumption and the inner filter effect did not play a role in the signal measurement and acquisition.⁷⁵ While the H-Transform is an approximation, correction for substrate consumption and the inner filter effect based on theory would require determining five parameters for each fluorescence curve (two kinetic parameters related to substrate consumption, as well as three parameters characterizing the inner filter effect), which is theoretically difficult and practically impossible.⁶⁹ In contrast, the H-Transform requires a single parameter, α , and is shown as Equation 4.⁶⁹

$$\mathcal{F}_{ideal} = \alpha \tanh^{-1}(\mathcal{F}_{exp}/\alpha) \quad (4)$$

In Equation 4 F_{exp} is the experimentally measured fluorescence intensity, α is a constant, and F_{ideal} is the fluorescence intensity in the absence of substrate consumption and the inner filter effect (i.e. the transformed, ideal intensity).⁶⁹ The correct value of α is the one that converts the fluorescent signal into a straight line when the fluorescence intensity is constant; in other words, when the amidolytic activity (or the amide bond cleavage activity) of thrombin on the fluorosubstrate is constant. Constant amidolytic activity in human plasma is always due to the presence of the thrombin-alpha2M complex, since free thrombin in human plasma rapidly decays; the thrombin-alpha2M complex is used as the thrombin calibrator in the CAT assay.⁶⁹ Because of this, the easiest way to determine α is to take the first derivative of the experimentally measured thrombin calibrator curve, pass a trend-line through the values, and alter α until the trend-line is horizontal; the intercept of this horizontal trend-line with the ordinate is a value called the ideal calibrator reaction velocity.⁶⁹ Note that the first derivative of these ideal calibrator curves was computed using the numerical approximation given as Equation 5, or the first-order divided difference formula⁷⁶:

$$f'(t) = \frac{f(t_j) - f(t_i)}{t_j - t_i} \quad (5)$$

In Equation 5, f represents the ideal fluorescence signal intensity and t_i and t_j represent two adjacent measurement time points.

The ideal calibrator reaction velocity for the undiluted thrombin calibrator was used to compute the calibration factor, or the factor that transforms any ideal fluorescence signal to a total ideal thrombin concentration integral. As such, this single calibration factor was then used to transform the diluted and undiluted ideal calibrator intensities to total ideal thrombin concentration integrals. Each total ideal thrombin integral was differentiated using Equation 5, yielding the associated steady-state thrombin generation time-course for each calibrator. Note that since Equation 5 is first-order, the derivative it yields is much noisier than the original signal.⁶⁹ Therefore a trend-line was passed through each steady-state thrombin generation time-course, the intercept of which represents the calculated steady-state thrombin concentration for each calibrator. These steady-state thrombin generation time-courses are important since they can be used to gauge the accuracy of the CAT data analysis methods, given that the true thrombin concentration of each calibrator, whether diluted or not, is known a priori. As such, the purpose of diluting the purchased thrombin calibrator in this CAT assay was to enable a comparison between the known and computed thrombin calibrator concentrations. This comparison was done by plotting the known and calculated thrombin calibrator concentrations and seeing if a significant difference between the two existed. This comparison plot is shown as Figure 30.

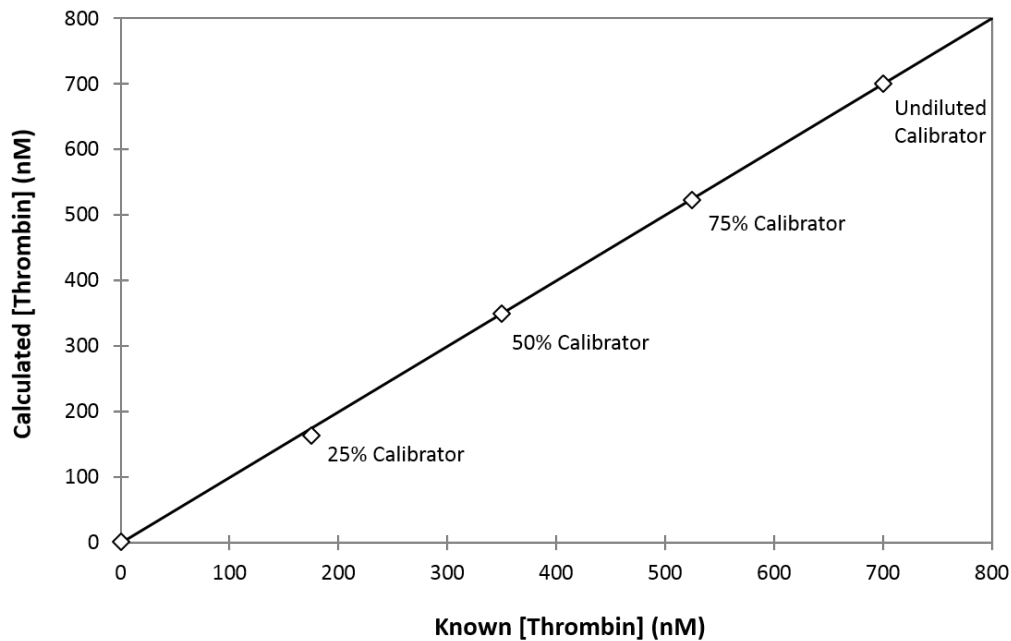


Figure 30: Comparison plot between the known and computed thrombin calibrator concentrations used in the in-house CAT assay. The thrombin calibrator concentrations were computed via the data analysis method outlined by Hemker and Kremers.⁶⁹

If the known and calculated thrombin calibrator concentrations were identical they would lie on the black line shown in Figure 30. As such, the agreement between the two is very strong, indicating that both the CAT assay protocol and analysis methods are sound.

To compute the thrombin generation time-courses for the unknown samples, the corresponding experimentally measured fluorescence intensities are first converted to their ideal values using the H-Transform (or Equation 4, with α determined from the average undiluted thrombin calibrator curve). Next the calibration factor was used to convert these ideal fluorescence signals to total ideal thrombin concentration integrals. From these total thrombin integrals, the fluorescent signal corresponding to free thrombin alone was mathematically dissected using the algorithm outlined by Hemker and Beguin in 1995; this was done to account for the alpha2M effect.¹⁷ This algorithm was programmed as a MATLAB® executable and the corresponding output total ideal *free* thrombin concentration integrals were inserted into Microsoft Excel, where the same reference value was subtracted from each to bring their origins to approximately zero. At this point in the data analysis a smooth curve was fitted through each total ideal *free* thrombin concentration integral; the generic form of this equation is given as Equation 6.⁶⁹

$$T = \varepsilon \times n \times \exp(-\exp(-(t - \tau)k_{dec})) \quad (6)$$

In Equation 6, T is the total ideal free thrombin concentration, ε is the ETP, τ is the time to peak thrombin concentration, π is the peak thrombin concentration, n is the number of measuring points per minute, and k_{dec} is the decay constant of thrombin; it can be calculated from the relation $k_{dec} = 2.72\pi/\varepsilon$, where the constant 2.72 is the basis of the natural logarithm.⁶⁹ Once the total ideal free thrombin integrals are properly fitted to Equation 6, the associated free thrombin generation time-courses for the unknown samples are found analytically by differentiating Equation 6 with respect to time, yielding Equation 7.

$$[Thrombin] = d(T)/dt = k_{dec} \times n \times \varepsilon \times \exp(k_{dec}(\tau - t) - \exp(k_{dec}(\tau - t))) \quad (7)$$

The average free thrombin generation time-courses, or thrombograms, for the unknown samples run in this in-house CAT assay are shown as Figure 31.

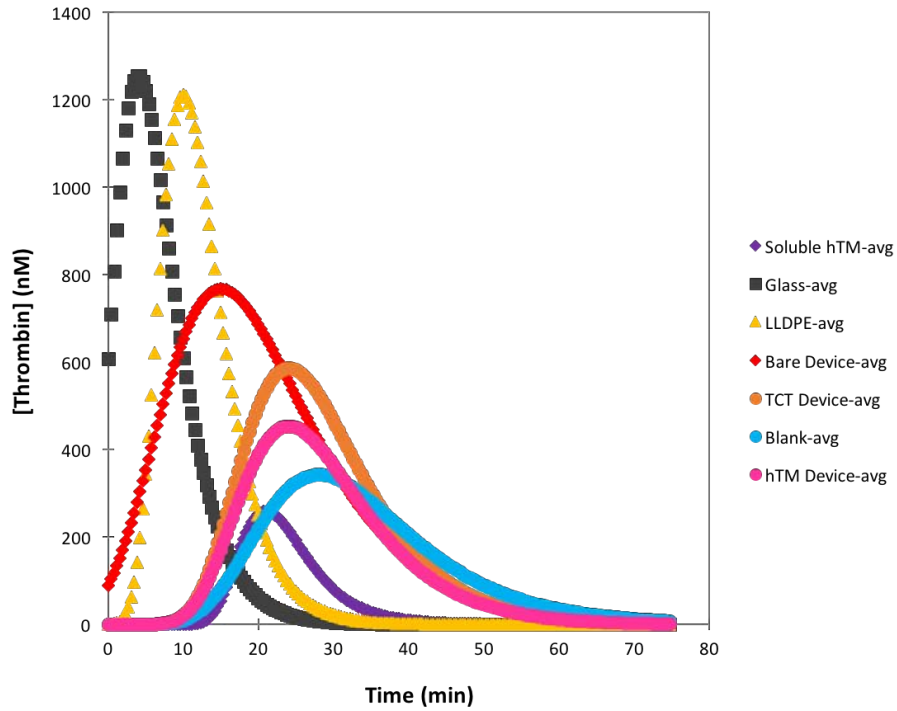


Figure 31: The average free thrombin generation time-courses, or thrombograms, associated with the unknown samples run in the in-house CAT assay.

As evidenced by Figure 26, several single value metrics exist to describe a given thrombogram. One such metric of overall thrombogenicity is peak thrombin concentration. This metric is shown in Figure 32 for all the samples run in this in-house CAT assay.

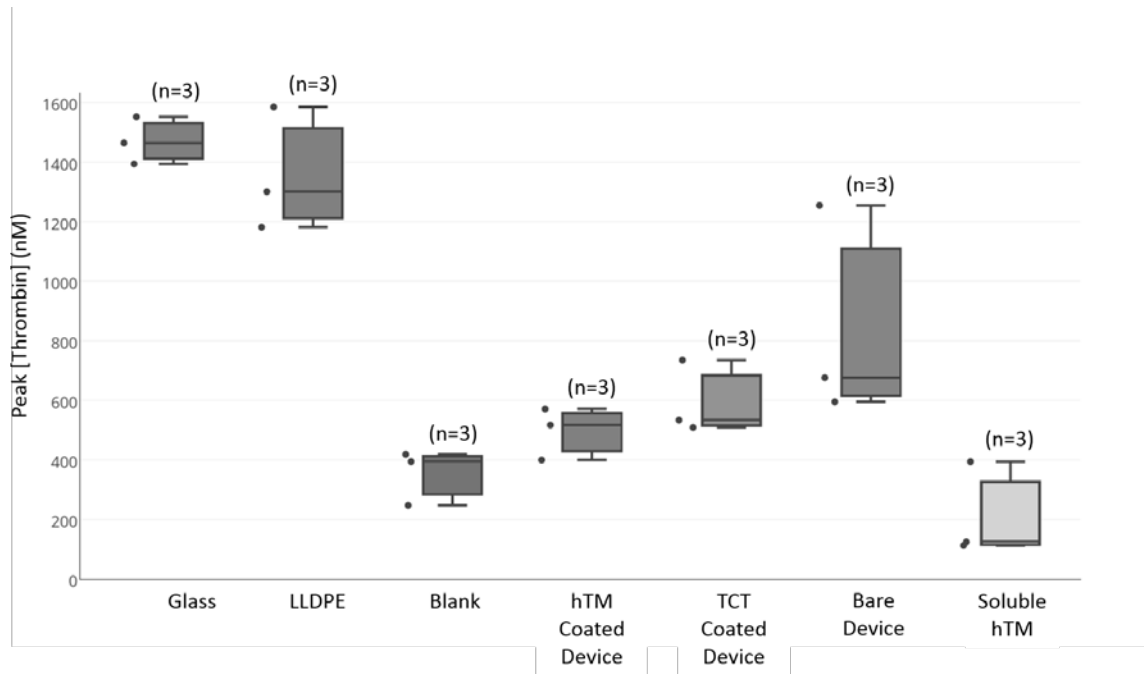


Figure 32: The peak thrombin concentration associated with the thrombogram of each sample run in the in-house CAT assay.

In Figure 32 both the hTM and TCT coated #2 flow diverting devices generated less thrombin, and therefore exhibited less thrombogenicity, than the bare #2 devices, as well as the positive controls glass and LLDPE. The two types of negative controls, blank and the soluble hTM, generated less thrombin than both the hTM and TCT coated #2 devices; this suggests that the developed coating technology may be optimized to achieve even lower thrombogenicity. Nevertheless, this thrombogram indicates that the bioactive function of the conjugated hTM in the developed coating technology may reduce flow diverting device #2 thrombogenicity to a greater extent than that of the combined Al₂O₃, APTES, and TCT layers. Further testing on this point is however warranted.

Third-Party In-Vitro Assessment of Coating Technology Thrombogenicity

In addition to the in-house CAT assay testing done at the University of Iowa, shown in Figure 32, in-vitro thrombogenicity testing of the developed coating technology was also done by a third-party commercial vendor. The testing protocol used was not made available; nevertheless, it is expected to be similar to the CAT assay method previously described. For this initial third-party in-vitro assay, I coated one flow diverting device #1 (4.75x18 mm in size) with hTM at the University of Iowa and shipped this

device whole to the commercial vendor on ice. The vendor then cut the hTM coated device into two 5.5 mm long pieces and performed the testing on these pieces. The results, in terms of peak thrombin generation, are shown in Figure 33.

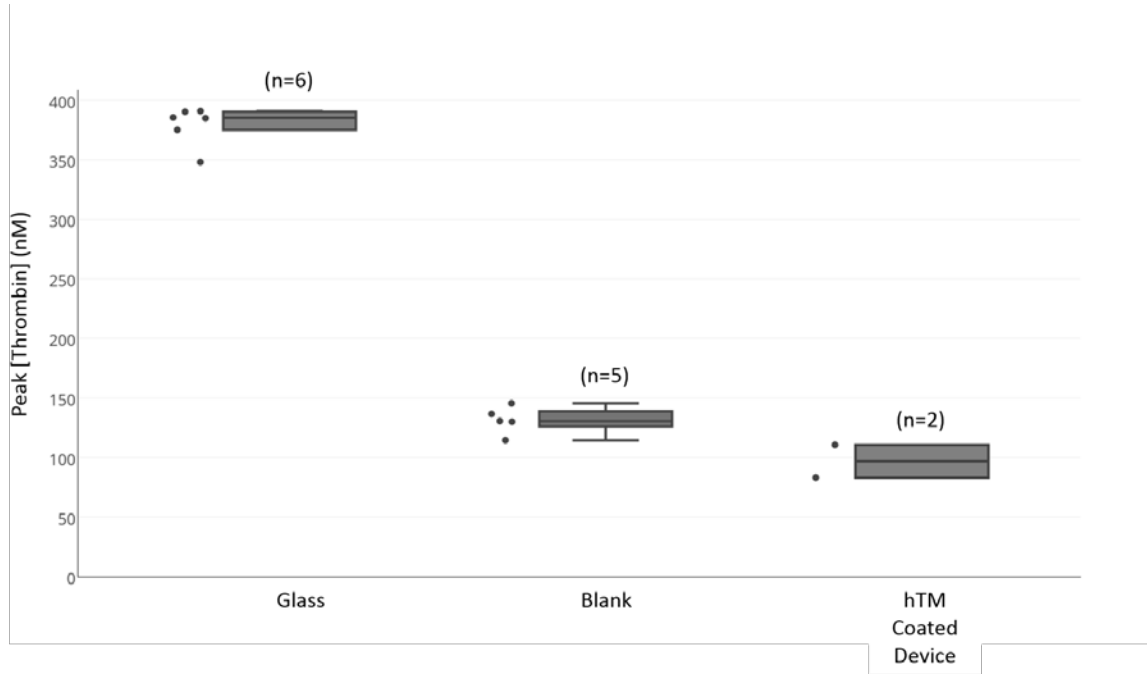


Figure 33: The peak thrombin concentration associated with the thrombogram of each sample tested by a third-party commercial vendor. The hTM coated commercial flow diverting device #1 in this test was shipped on ice.

Similar to the in-house thrombogram results shown in Figure 32, Figure 33 indicates that a hTM coated flow diverting device #1 stored at approximately 2°C generates thrombin comparable to that of blank wells in-vitro (in human re-calcified PRP). Next six coated commercial #1 flow diverting devices were sent to the third-party vendor; three were hTM coated #1 devices (one 5.0x18 mm, one 5.0x20 mm, and one 4.75x18 mm), while the remaining three #1 devices (one 5.0x14 mm, one 5.0x35 mm, and one 4.75x18 mm) were coated with a combination of hTM and APC (incubation solution consisted of 10 µg hTM + 0.25 mg APC in 500 µL DPBS). I coated all devices at the University of Iowa and shipped them whole to the vendor at room temperature. The vendor then cut each device in half and performed testing on the halves (3 halves were excluded from the study due to problems during testing and analysis). The peak thrombin generation test results are shown in Figure 34. Note that the vendor lumped all coated devices sent to them in a single group; in this in-vitro assay the vendor also tested against a similar flow diverting device coated with a competitive technology, as well as bare #1 devices.

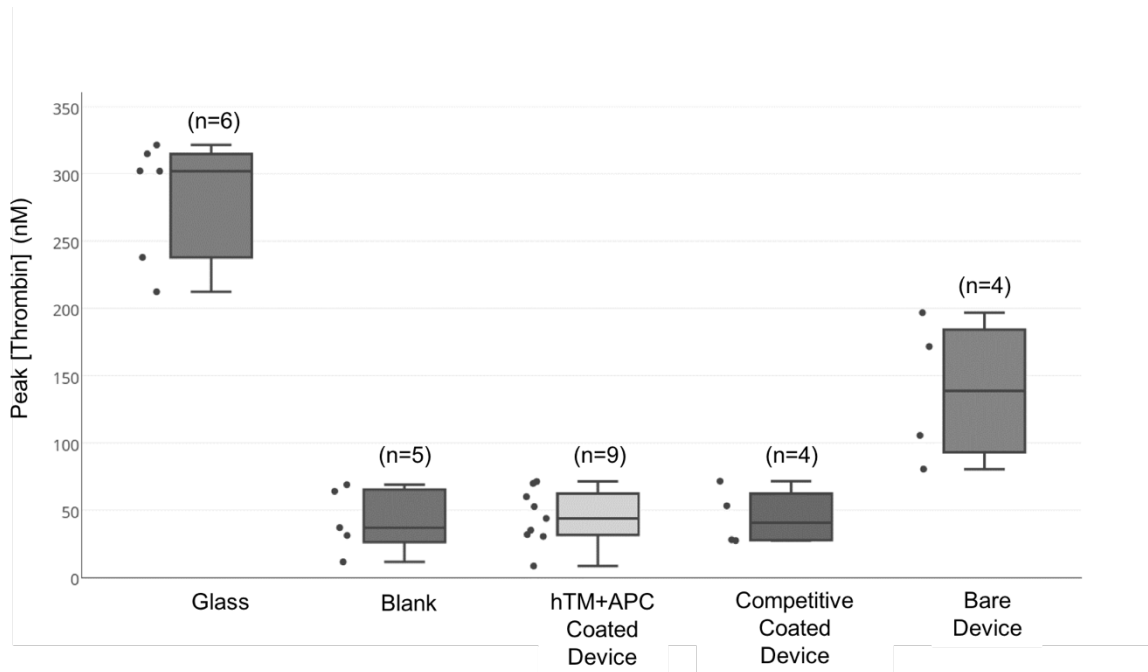


Figure 34: The peak thrombin concentration associated with the thrombogram of each sample tested by the third-party commercial vendor, relative to a similar flow diverting device coated with a competitive technology. The hTM and hTM+APC coated commercial #1 flow diverting devices in this test were shipped at room temperature.

Figure 34 indicates that the developed coating technology, regardless of being incubated with hTM alone or a combination of hTM and APC, has thrombogenicity comparable to the blank wells; additionally, the developed coating technology is comparable to the competitive technology, which are both less thrombotic than glass and bare #1 flow diverting devices. These results are in keeping with the in-vitro results previously discussed.

The final in-vitro thrombogenicity test performed by the third-party vendor was on three commercial #1 flow diverting devices coated with TCT. Similar to the other third-party in-vitro thrombogenicity tests, I coated these #1 devices (one 5.0x20mm device, one 4.5x20mm device, and one 4.5x18mm device) with TCT at the University of Iowa and shipped them whole at room temperature. The vendor then cut each device in half and performed the testing on each half. The peak thrombin generation test results are shown as Figure 35.

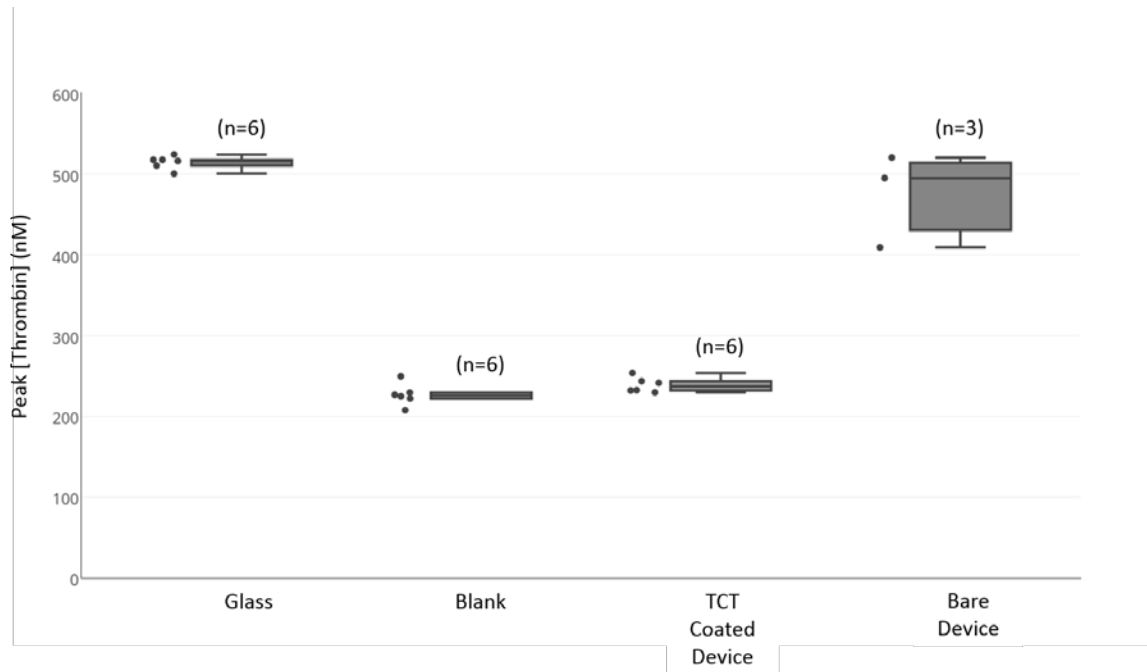


Figure 35: The peak thrombin concentration associated with the thrombogram of each sample tested by the third-party commercial vendor. The TCT coated commercial #1 flow diverting devices in this test were shipped at room temperature.

Figure 35 indicates that TCT coated #1 flow diverting devices have thrombogenicity comparable to blank wells, the implication of which is that the addition of the bioactive component hTM does little to further decrease the thrombotic response of coated #1 devices. This is in contrast to the findings of the in-house thrombogram, shown as Figure 32, which indicates that the developed coating technology (i.e with conjugated hTM) decreases commercial flow diverting device #2 thrombogenicity beyond that of TCT coated #2 devices. It is recognized that these in-vitro thrombin generation assays were performed with different flow diverting devices and different blood samples, both of which could impact results; as such, further testing is required.

In-Vitro Evaluation of Coating Technology Shelf Life

To evaluate the longitudinal stability of the bioactive component hTM in the developed coating technology, a shelf life study was performed; specifically, the study design consisted of coating pieces of commercial flow diverting device #3 (each piece between 3 – 4 mm in length, 5 mm in diameter) with the developed coating technology and assessing the immediate (or Time 0) thrombogenicity of these hTM coated devices (n=3) via the CAT assay protocol at the University of Iowa. The remaining hTM coated

#3 device pieces were stored on the shelf at ambient temperature and pressure; their thrombogenicity was assessed via the CAT assay at the following longitudinal time points post coating (n=3): one week, two weeks, 5 weeks, 8 weeks, and 33 weeks. Bare flow diverting device #3 pieces of the same diameter and approximately the same length (or between 3 – 4 mm) as the hTM coated pieces were cleaned via the established sonication protocol; their thrombogenicity was assessed via the CAT assay at the same longitudinal time points post coating (n=3 at each time point). At the initial, or Time 0, time point, 5 μ L from one of the six hTM-PBS solutions (used to incubate the coated devices in) was pipetted into individual microplate wells of the CAT assay and used as a negative control (n=3), as per the in-house CAT assay protocol previously discussed; following this, three of the six hTM-PBS incubating solutions were frozen at -80°C . The remaining three hTM-PBS solutions were further diluted by 0.1% Bovine Serum Albumin (BSA, purchased from Sigma-Aldrich) and frozen at -80°C . Subsequently for each longitudinal study time point one hTM-PBS solution and one hTM+BSA-PBS solution was thawed, pipetted into individual microplate wells (5 μ L each), and used as independent negative controls (n=3 each); subsequently, these two solutions were re-frozen at -80°C . Also at each longitudinal study time point, the tip of a sterile glass pipette was broken under the cell culture hood and similarly sized pieces were placed in individual microplate wells (n=3) for use as a positive control.

One unit of human whole blood (collected from healthy single donors into sodium citrate) was used for each CAT assay in this study and was purchased from ZenBio Incorporated; each unit of human whole blood arrived at the University of Iowa one day post collection and the respective shelf life CAT assay was run the same day. Upon arrival, about 100 mL of the whole blood sample was centrifuged in a swinging bucket centrifuge at 20°C to separate the PRP – ultimately the platelet count of this PRP was adjusted to approximately 150 platelets/nL using a Sysmex XE-2100 CBC analyzer and a sample of PPP to further dilute the platelet-rich blood sample, as outlined previously. However, the duration and time required for PRP centrifugation was found to be highly variable and dependent on blood sample, as well as time intensive; as a result, it was found that it was possible to centrifuge the whole blood sample too much and thus deplete the platelet count of the associated PRP sample used in the CAT assay. Over centrifugation of the whole blood sample occurred at the Week 5 and Week 33 shelf life study time points, which resulted in using PRP samples with fewer than 150 platelets/nL in the respective CAT assays. Additionally, the Sysmex XE-2100 CBC analyzer was

broken on the day of the Week 1 study time point, so that no PRP sample dilution could be performed; in this case, the respective human whole blood sample was centrifuged until there was visual PRP separation. Subsequently, this PRP sample was pipetted carefully from the buffy coat and used directly in the CAT assay; a 300 μ L aliquot of this PRP sample was stored in a tissue culture shaker at 37°C for approximately four hours until the Sysmex was functional and a platelet count measurement could be taken – at this time it was found that the PRP sample used in the Week 1 CAT assay contained approximately 234.3 platelets/nL. Table 2 summarizes the blood donor demographic information associated with each blood sample used in the shelf life study, as well as the platelet count of each respective PRP sample.

Table 2: Shelf life study blood donor demographic Information and associated platelet-rich plasma (PRP) platelet counts

Time Point Post Device Coating	Donor Sex	Donor Age	Donor Ethnicity	Donor Weight	Donor Blood Type	PRP Platelet Count (platelets/nL)
0 (i.e. immediately post coating)	M	36	African American	202	B+	154.0
Week 1	M	54	African American	164	A+	234.3*
Week 2	M	40	Hispanic	285	O+	155.3
Week 5	M	31	African American	210	not listed	136.3**
Week 8	M	45	African American	242	O+	153.0
Week 33	M	53	Hispanic	227	O+	126.5**

* indicates the Sysmex XE-2100 CBC analyzer was broken and the platelet count was measured post assay completion. **indicates that whole blood sample over centrifugation occurred.

It should be mentioned that a shelf life study CAT assay was run at Week 17 post coating; however, for this assay the autocalibrate setting of the SpectraMax M5 fluorometer was inadvertently set to “OFF”, resulting in premature saturation of the fluorometer photomultiplier tubes during kinetic measurement of the fluorescent signal, and a corresponding signal error; because of this error it was impossible to analyze the data and the entire dataset was thrown out.

Nevertheless, the same CAT assay data analysis strategy previously outlined⁶⁹ was used to analyze the shelf life study data time points summarized in Table 2. It should be noted that, across the time points analyzed, the bare flow diverting device #3

pieces especially exhibited undulations in their raw fluorescent signal time courses (similar undulations were sporadically observed with the hTM coated #3 devices) – such highly undulated raw data curves were not observed in the in-house CAT assay with the #2 flow diverting devices. As a result, these large undulations were propagated from the raw data through the mathematical corrections for substrate consumption, inner filter, and alpha2M effects, ultimately resulting in highly undulated total ideal free thrombin concentration integrals. Since Hemker et al.⁶⁹ devised the smooth model given by Equation 6 in 2013 (or a time-varying three parameter model containing parameters with physiologic meaning) to fit each total ideal free thrombin concentration integral, having highly undulated total ideal free thrombin concentration integrals leads to poor Hemker model fits and ultimately poor thrombograms. To highlight this, representative total ideal free thrombin concentration integrals with large undulations, and their corresponding Equation 6 Hemker et al. model fits, for both bare and hTM coated commercial #3 flow diverting devices from Time 0 is shown as Figure 36.

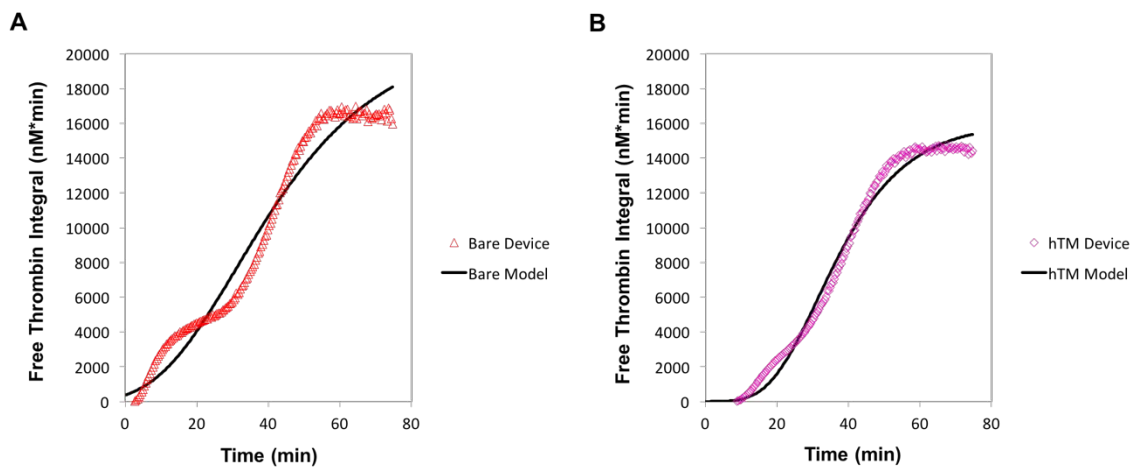


Figure 36: (A) A highly undulated free thrombin concentration integral for a bare commercial flow diverting device #3 piece, and respective Hemker model fit, observed for Time 0 of the shelf life study. (B) A moderately undulated free thrombin concentration integral for a hTM coated commercial flow diverting device #3 piece, and respective Hemker model fit, also observed for Time 0 of the shelf life study.

Observing undulations in total ideal free thrombin concentration integrals is not uncommon; in fact, in 2006 Wagenvoort et al.⁷⁷ defined an explicit four-parameter function, called the W-function, that could fit any experimental total ideal free thrombin concentration integral measured in PPP that the group tested within the limits of the experimental error. When thrombin generation was measured in PRP, Wagenvoort et al. found that a sum of two W-functions, shown as Equation 8, could always be fitted to the respective total ideal free thrombin concentration integral.⁷⁷

$$T = W(a, b, c, d, f, g, t_{01}, t_{02}, t) = abce^{bc(-t+t_{01})}(e^{b(t-t_{01})} - 1)^{c-1} + dgfe^{gf(-t+t_{02})}(e^{g(t-t_{02})} - 1)^{f-1} \quad (8)$$

Since the shelf life study was carried out in PRP, I tried fitting Equation 8 to the total ideal free thrombin concentration integrals shown in Figures 36A and 36B; however, since Equation 8 contains eight parameters it is an over parameterized model, meaning the fit of the model to any given total ideal free thrombin concentration integral is very sensitive to the initially specified parameter values – in other words, manifold possible model fits of indistinguishable validity exist for any given total ideal free thrombin concentration integral.⁷⁷

Since Equation 8 does not robustly fit total ideal free thrombin concentration integrals and since the 2013 Hemker et al. model given in Equation 6 is robust but can produce poor model fits, I thought perhaps instead of using either one to analytically compute the thrombin generation time course, numerically differentiating a total ideal free thrombin concentration integral to compute the corresponding thrombin generation time course might produce a thrombin generation time course that most closely represents the experimental data. As such, I computed the numerical derivative of every total ideal free thrombin concentration integral in each shelf life study assay using Equation 5 (where the difference of t_i and t_j was set to a moving average across a five-data point span) and determined the peak thrombin concentration in the resulting thrombogram; in addition, I used the 2013 Hemker et al. model (given by Equation 6) to fit every total ideal free thrombin concentration integral, and in the resulting thrombogram I likewise determined the peak thrombin concentration. To assess the extent of the variability existing between the peak thrombin concentrations computed by numerical differentiation and by the 2013 Hemker et al. model in the shelf life study, I plotted the two in the same plot. This comparison plot for peak thrombin concentration is shown as Figure 37.

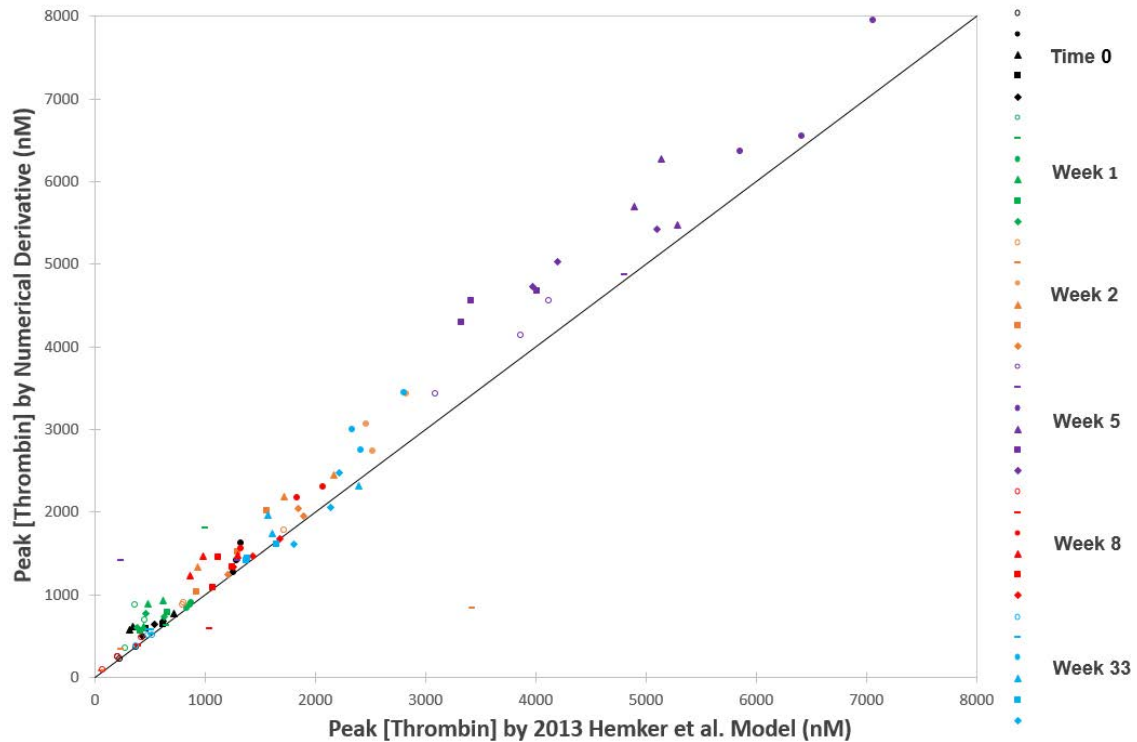


Figure 37: Comparison plot between the peak thrombin concentration computed by numerical differentiation and by the 2013 Hemker et al. model in the shelf life study.

If the peak thrombin concentrations computed by first differentiating any given total ideal free thrombin concentration integral numerically, or else by analytically differentiating the respective model proposed by Hemker et al. in 2013 were equivalent they would lie on the black line shown in Figure 37. As it stands, the computed peak thrombin concentrations all lie close to the equivalence line; in fact, calculation of peak thrombin concentrations by numerical differentiation consistently over estimates the respective value when compared to analytically differentiating the Hemker et al. 2013 model to determine the same. This is not surprising as first derivatives, even those computed via moving averages (as was done in this case), are much noisier and ultimately tend to amplify the original signal intensity.^{69, 76} Of the 103 data points, or peak thrombin concentrations, shown in Figure 37 only four are outliers relative to the equivalence line. These four are all peak thrombin concentrations associated with soluble hTM+BSA samples; in each of these four cases, the fit provided by the 2013 Hemker et al. model is extremely poor, yielding a diminished or else amplified peak thrombin concentration.

Since the peak thrombin concentrations shown in Figure 37 all lie relatively close to the equivalence line (albeit the four outliers), with any deviation exhibiting an over

estimation trend in numerically derived peak thrombin concentration value, ultimately indicates that regardless of how peak thrombin concentration is computed the trends in how peak thrombin concentration changes from sample to sample for any given time point remains the same. Keeping this in mind, Figure 38 outlines the peak thrombin concentrations computed for each sample via Hemker et al.'s 2013 model for every shelf life study time point – in other words, Figure 38 depicts the longitudinal trends in peak thrombin concentration for the shelf life study.

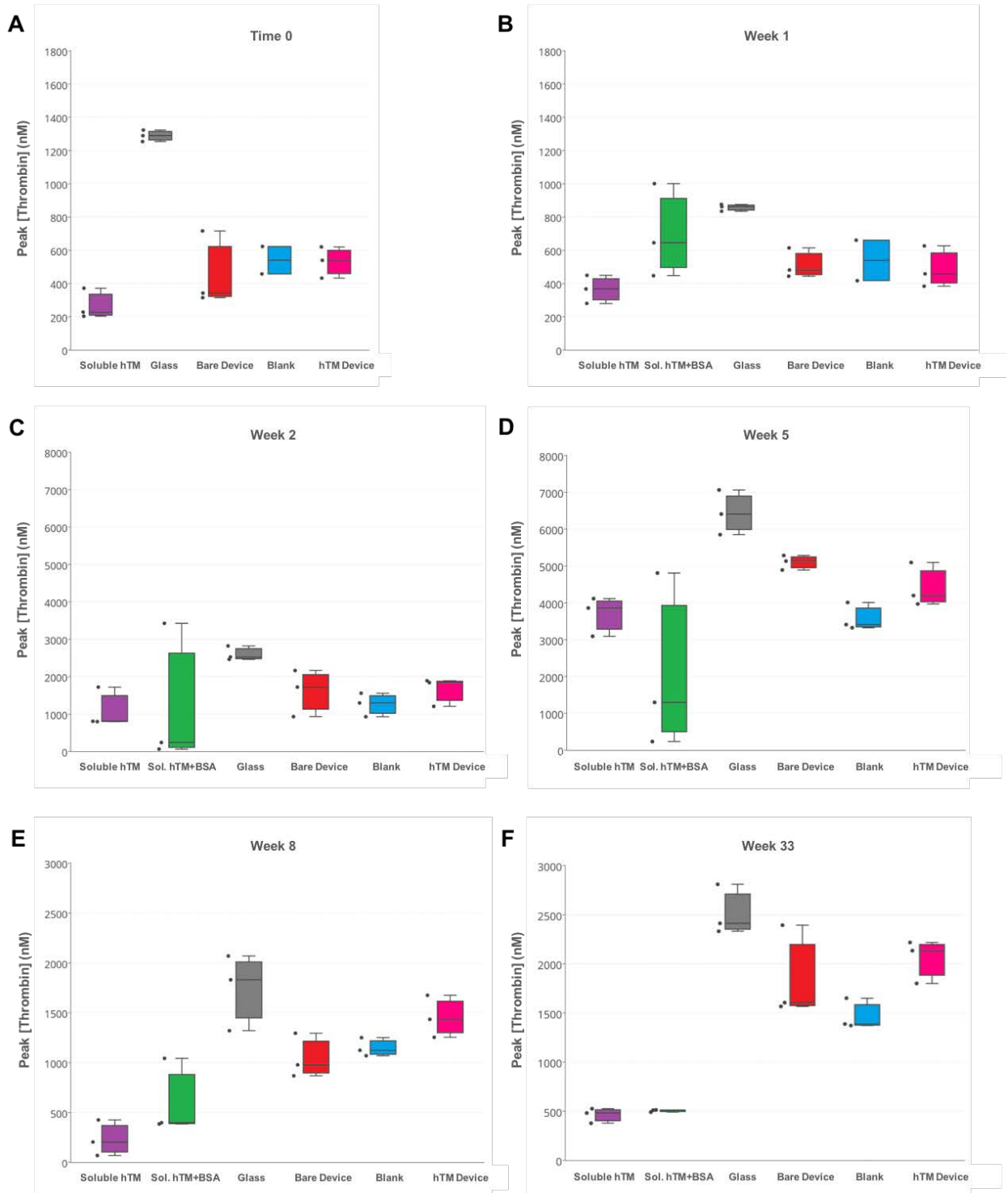


Figure 38: The peak thrombin concentrations computed via the Hemker et al. 2013 model⁶⁹ for (A) each sample tested in the shelf life CAT assay performed immediately post coating (Time 0), (B) each sample tested in the shelf life CAT assay performed one week post coating, (C) each sample tested in the shelf life CAT assay performed two weeks post coating, (D) each sample tested in the shelf life CAT assay performed five weeks post coating, (E) each sample tested in the shelf life CAT assay performed eight weeks post coating, and (F) each sample tested in the shelf life CAT assay performed 33 weeks post coating.

Note that all samples shown in Figure 38 were tested in triplicate (or n=3) albeit for the blank samples tested at Time 0 (Figure 38A) and Week 1 (Figure 38B); these two samples alone were tested in duplicate (or n=2), since pipetting errors caused the respective triplicate sample to be thrown out. Nevertheless, the most striking observation from Figure 38 is that the bare commercial flow diverting device #3 pieces exhibit large variation in the amount of thrombin they generate; furthermore, bare #3 device pieces are not particularly thrombogenic since in every CAT assay in this shelf life study at least some bare device pieces generate as much thrombin as blank wells, save for Week 5 (Figure 38D). The variability observed in this study regarding in the amount of thrombin generated by bare flow diverting device #3 pieces is likely impacting the longitudinal thrombin generating capacity of the hTM coated #3 flow diverting devices, making it difficult to parse out the individual contribution of the conjugated hTM on thrombin generation. Nevertheless, the variability in thrombin generating capacity of bare and hTM coated #3 devices in this study is likely only minimally impacted by surface area effects caused by testing devices of inconsistent lengths; this is because all devices tested in each shelf life CAT assay were carefully placed in the respective U-bottom microplate well such that, upon visual inspection, one device end was adjacent with the top of the U-bend while the other end was left unsubmerged – in other words, untouched by PRP and CAT assay reagents. More testing is required to further evaluate the thrombin generating capacity of both bare and hTM coated #3 flow diverting devices; though the trend indicated by this shelf life study is that the longitudinal thrombin generating capacity of the developed coating technology deposited on #3 flow diverting devices does not significantly increase.

In-Vivo Survival Study in a Porcine Model

Note: I coated all devices included in this study at the University of Iowa. The rest of the study was performed by Dr. David Hasan, a practicing neurosurgeon.

A porcine model was used to assess the feasibility of the developed coating technology in-vivo; specifically, this was done at the University of Iowa and was designed as a preliminary study to assess survival of pigs with implanted hTM coated devices. In particular the study design consisted of bilaterally-inserting 10 hTM coated stent-assisted coiling devices #4 (commercially available, 3.0x15 mm in size) into the common carotids of five mini Yucatan pigs. The pigs were of mixed sex and weighed

between 44-88 pounds each. Initially I coated all devices at the University of Iowa and shipped them to the device manufacturer, where they were inserted into their respective deployment catheters and sterilized via the manufacturer's standard electron beam sterilization technique. The devices were then shipped back to the University of Iowa for deployment in the pigs. The general care, anesthesia, operating room (OR), and euthanasia protocols for the animals used in this study were in compliance with the University's Institutional Animal Care and Use Committee (IACUC). Briefly, one hTM coated #4 device was deployed by a practicing neurosurgeon into each common carotid artery of an animal under general anesthesia, resulting in the deployment of two hTM coated #4 devices per animal. Device deployment and subsequent vascular wall apposition was checked with digital fluoroscopic x-ray during surgery. Post surgery, a clinical neurological check was performed on each animal every six hours for five days; this was done to check for signs of neurological deficit. On the fifth day the animals were again put under general anesthesia and subjected to both MRI and time-of-flight MRA head and neck scans. Each animal was then brought to the OR where the animal was euthanized and the carotid arteries were subsequently excised for gross inspection.

It should be mentioned that a limitation to this study is lack of a good animal model for acute stroke.⁷⁸ In pigs and sheep, lack of a true capillary bed between the pharyngeal and internal carotid arteries blocks full access to the internal carotid and therefore does not allow a clot to be delivered to the substance of the brain.⁷⁸ Excessive collateral circulation in dogs compromise their use as stroke models and smaller animals have blood vessels that are much smaller than the average adult human, limiting their use.⁷⁸ Nevertheless, the merit of the porcine model is that it roughly duplicates the vascular dimensions of an adult human,⁷⁸ which is why this model was chosen for the University of Iowa survival study.

The primary finding of this preliminary in-vivo survival study was that all animals were alive at five days post device implantation surgery and none exhibited neurological deficits on exam, meaning all animals survived and were in good health at the study endpoint. One pig developed a groin hematoma, a complication associated with the surgical access site, and developed a limp; however, the appropriate pain-relieving therapy for this complication was administered by a veterinarian. The MRI head and neck scans indicated no brain lesions or strokes in any of the animals; likewise, the time-of-flight MRA head and neck scans indicated good blood flow distal to the implantation

sites in each animal. A gross inspection of the excised #4 devices was done by a practicing neurosurgeon and indicated that eight devices were patent, while two devices exhibited major thrombosis thought to be caused by crimping of the device ends. Due to the age of the digital fluoroscopic x-ray used during surgery to position and deploy each device, it is unknown whether the device crimping occurred during deployment or during the excision procedure.

Ex-Vivo Evaluation of Coating Technology Thrombogenicity in a Primate Shunt Model

Note: I coated all devices included in this study at the University of Iowa. The rest of the study was performed by Dr. Monica Hinds, Associate Professor in Biomedical Engineering at the Oregon Health and Science University.

An established primate model⁷⁹⁻⁸⁴ was used to evaluate the extent of platelet and fibrin accumulation in two different commercially available flow diverters coated with the developed technology, as well as control devices, in permanent ex-vivo arteriovenous (AV) shunts in trained and conscious baboons. This primate shunt model has been used extensively to quantify the hemocompatibility of biomaterials, including stents,⁷⁹⁻⁸⁴ as well as the antithrombotic efficacy of both established and novel antithrombotic drugs.⁸⁵⁻⁸⁸ Specifically a baboon is a good thrombosis model because of its hemostatic similarity to humans, its large size, the logistical ease of acquiring frequent blood samples, as well as the animals' general acceptance of chronically patent AV cannulas.⁸⁹

All primate experimentation was performed at the Oregon National Primate Research Center (ONPRC) in Beaverton, Oregon under the umbrella of an IACUC-approved protocol #0681. The study design of the first experiment consisted of comparing both the platelet and fibrin deposition of the following commercial flow diverting devices, all 2.75x19 mm in size, deployed in the AV shunt of the same primate to limit variability (male, approximately four years old): a bare #2 flow diverting device (n=2), a hTM coated #2 device (n=2), and a bare #2 device deployed in combination with dual anti-platelet therapy (or DAPT) (n=2). I coated all #2 devices at the University of Iowa. In contrast, the second experiment consisted of comparing both the platelet and fibrin deposition of commercial flow diverting devices made by a different manufacturer, all 4.2x50 mm in size, deployed in the same AV shunt of a different primate (male,

approximately four years old): a bare flow diverting device #5 (n=2), a hTM coated #5 device (n=2), a hTM coated #5 device deployed in combination with aspirin, and a bare #5 device deployed in combination with DAPT (n=2). Like the initial flow diverting devices, I coated these flow diverting devices at the University of Iowa.

Prior to AV shunt deployment in both experiments, all devices were re-inserted into their respective deployment catheters and sterilized, via commercial electron beam techniques, by each respective device manufacturer and shipped to ONPRC for testing. Once there, each device was deployed in the AV shunt and the corresponding blood flow was held constant at 100 ml/min by an external screw clamp; a Doppler ultrasonic flow meter was also used to continuously measure the mean blood flow rate through the shunt during each experiment. To measure platelet deposition in each deployed device, autologous platelets were radiolabeled with Indium-111 (^{111}In) and re-injected into the primate weekly. Platelet deposition was then measured over a one-hour perfusion period using a high sensitivity 99Tc collimator and scintillation camera (GE 400T, General Electric); imaging of the 172 keV ^{111}In photon peaks was done at approximately three-minute intervals and recorded over the perfusion period.

Fibrin deposition was also measured during the same perfusion period; to do this, homologous fibrinogen labeled with Iodine-125 was first injected 24 hours prior to experimentation. Following the perfusion period, each device was removed from the shunt and the amount of fibrin deposition was measured after the Iodine-125 decayed using a Wizard gamma counter and standard curves.⁸⁹ Each device was subsequently dehydrated in increasing concentrations of ethanol, critical point dried, and weighed; the device weight was then compared to the weight prior to deployment in the shunt to determine the amount of fibrin accumulation over time. The extent of both platelet deposition and fibrin accumulation on the bare devices, hTM coated devices, hTM coated devices deployed in combination with aspirin (hTM-Coated+ASA), and bare devices deployed in combination with DAPT (Bare+DAPT) is shown as Figure 39. Specifically, the extent of fibrin accumulation and platelet deposition on the #2 devices – including bare and hTM coated #2 devices, as well as bare #2 devices deployed in combination with DAPT (Bare+DAPT) – was measured and is shown as Figures 39A and 39C, respectively. The extent of fibrin accumulation and platelet deposition on the #5 devices – including bare devices, hTM coated devices, hTM coated devices deployed in combination with aspirin only (hTM-Coated+ASA) and bare devices deployed in

combination with DAPT (Bare+DAPT) – was measured and is shown as Figures 39B and 39D, respectively.

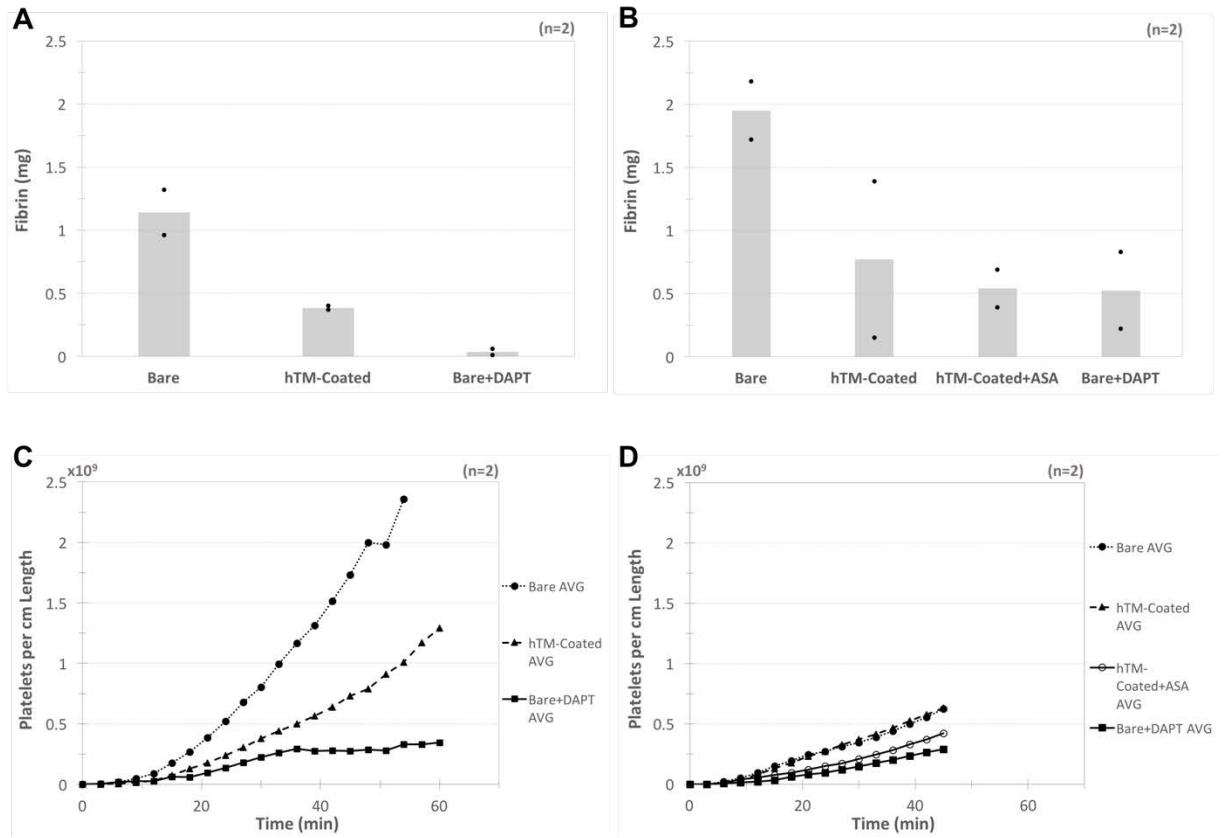


Figure 39: Figure 8: (A) Fibrin accumulation for each commercial flow diverting device #2 deployed in a primate AV shunt for an hour long perfusion period. The black circles indicate the fibrin accumulation for each individual device, while the gray bars indicate the average. (B) Fibrin accumulation for each commercial flow diverting device #5 deployed in a different primate AV shunt for a 45-minute perfusion period. The black circles indicate the fibrin accumulation for each individual device, while the gray bars indicate the average. (C) The corresponding average platelet accumulation for each #2 device deployed in the primate shunt and shown in panel A. (D) The corresponding average platelet accumulation for each #5 device deployed in the primate shunt and shown in panel B.

It should be noted that the second experiment, shown in Figures 39B and 39D, used flow diverting devices approximately 2.6 times as long as the devices used in the first experiment, or Figures 39A and 39C (50 mm long vs. 19 mm long). Because of the increased length, these devices were more difficult to deploy in the ex-vivo AV shunts; thus, some device ends were crimped during deployment. The combination of these factors led to uncontrollable platelet deposition in the bare #5 flow diverting devices deployed in combination with DAPT and resulted in the premature termination of the second experiment, or termination at 45 minutes post deployment.

The primary findings of these two ex-vivo primate shunt studies are: 1) the developed coating technology is functional on relatively short commercial #2 flow diverting devices without combined systemic anticoagulant use; in other words, short hTM coated #2 devices deployed alone accumulate fewer platelets (Figure 39C) and have decreased fibrin deposition (Figure 39A) ex-vivo when compared to bare #2 devices; however, short coated #2 devices deployed alone still accumulate more platelets and fibrin over time than bare #2 devices deployed in combination with DAPT and 2) the functionality of the developed coating technology is enhanced for relatively long #5 devices by combining their deployment with the administration of systemic aspirin; long hTM coated #5 devices deployed in combination with aspirin accumulate fewer platelets (Figure 39D) and fibrin (Figure 39B) over time than bare #5 devices and show similar platelet accumulation and fibrin deposition as bare #5 devices deployed in combination with DAPT.

CHAPTER 4

Specific Aim #3: Develop and Evaluate the Coating Technology as a Platform for the Attachment of FDA-Approved Molecules

Note: I helped coat all devices discussed herein at the University of Iowa.

Additionally, I performed several XPS acquisitions (as noted) and analyzed all of the associated XPS data.

The development of an antithrombotic coating technology for commercially available intracranial stents and flow diverting devices has the potential for great societal impact and therefore has garnered healthy commercial interest. Given this, we developed a coating technology with demonstrated suitability for commercially available intracranial devices and marked antithrombotic and hemocompatible functionality – all of this was done as part of specific aims #1-2, the details of which are outlined in Chapter 2 and 3. A schematic of the developed antithrombotic and hemocompatible coating technology is shown as Figure 2, with key design attributes outlined in Figure 3; in summary the developed coating technology is a very thin covalently-bound, multilayer film containing the naturally derived bioactive and antithrombotic agent human glycoprotein thrombomodulin (hTM). Inclusion of hTM in the coating chemistry was a targeted effort to actively disrupt the human coagulation cascade; hTM is an integral membrane protein expressed in-vivo on the human endothelial cell surface and actively disrupts coagulation since it acts as a protein cofactor in the thrombin-catalyzed activation of protein C.⁴⁹

From a commercial perspective, inclusion of the bioactive component hTM in the coating technology poses a problem since hTM is not FDA-approved; as a result, commercialization of the technology, as it stands, is more challenging. Yet hTM does not exclusively disrupt the human coagulation cascade; in fact, the FDA has approved several thrombin inhibitors for clinical use as anticoagulants, like Argatroban⁹⁰ and Lepirudin⁹¹. Likewise, other FDA-approved anticoagulants for use in humans contain bioactive components that inhibit Factor Xa, are platelet receptor antagonists, are fibrinolytic, or else are vitamin K antagonists (among other antithrombotic functions).⁹² With this in mind, one could replace the bioactive hTM component in the developed technology with an FDA-approved alternative since the conjugation of hTM to the underlying TCT layer is non-specific; in fact, both the order of deposited layers in the

developed technology and their chemistry could be modified to facilitate conjugation of FDA-approved molecules.

Specifically, inclusion of an FDA-approved alternative to hTM in the developed coating technology would lessen the amount of verification and validation testing required by the FDA for market approval. Furthermore, given the challenges outlined in Chapter 1 associated with incorporating bioactive components in coatings, it may be sufficient to incorporate a FDA-approved molecule with demonstrated hemocompatibility (and not bioactivity) into the technology; the idea being that such a technology would present fewer challenges in the way of U.S. market approval, facilitating commercialization. In the meantime, verification and validation testing could be performed on either the developed coating technology or else a modified technology containing an FDA-approved bioactive component – this type of commercialization pathway may be an attractive alternative to medical device companies looking to acquire the developed technology.

As such, specific aim #3 is to further develop and evaluate the coating technology as a platform for the attachment of FDA-approved molecules instead of the bioactive component hTM. The particular focus is to develop the coating technology as a platform for three specific FDA-approved molecules: methoxy-poly(ethylene glycol) amine (or mPEG), a derivative of phosphorylcholine (PC) called o-phosphorylethanolamine (o-PA), and heparin. Specifically, mPEG is a natural choice for incorporation into the developed technology since one terminal end consists of a primary amine that can be activated while the other is capped with a methoxy group that acts to prevent undesired intra- or intermolecular crosslinking and protein adsorption^{93, 94}; in fact, an injectable biologic containing mPEG and used to treat anemia gained FDA approval in 2007⁹⁵. Likewise, PC is a natural choice for incorporation into the technology since PC coatings have been used on implanted vascular devices for over 15 years.²⁰ Additionally, Medtronic's Shield Technology™ uses a modified version of PC chemically bound to their Pipeline™ Flex flow diverting device²⁰; since PC is a natural component of the red blood cell surface, PC coated vascular stents implanted in the peripheral or else coronary arteries of rabbits, pigs, dogs, and baboons reported decreased platelet adherence and thrombosis in the literature.⁹⁶⁻⁹⁹ In fact, the FDA approved a PC coated coronary stent (BiodivYsio™, Abbot Vascular Inc.) for use in human patients with symptomatic ischemic heart disease due to de-novo native coronary artery lesions in

2000.¹⁰⁰ Finally, heparin coatings have been used for decades to reduce the thrombogenicity of blood-contacting medical devices.¹⁰¹ Heparin is FDA-approved for use as a systemic anticoagulant in humans¹⁰¹; likewise several heparin coated medical devices have been approved by the FDA, including Carmeda BioActive Surface® coated hemodialysis catheters (2007) and the Cordis Bx Velocity™ coronary stent with Hepacoat™ (2001).¹⁰² As a result, heparin is another natural choice for inclusion in the developed coating technology.

In order to develop the coating technology as a platform for the attachment of FDA-approved molecules mPEG, PC, and heparin, several different coating chemistries with each molecule were tested on p-doped silicon wafers and their corresponding surface chemistry composition was evaluated via x-ray photoelectron spectroscopy (XPS). Subsequently the most promising chemistries incorporating each molecule were coated on commercial flow diverting device #5 pieces, their surface composition was evaluated via XPS, and their in-vitro thrombogenicity was assessed by a third-party vendor via the Calibrated Automated Thrombogram (CAT) Assay.

Development of the Coating Technology as a Platform for the Attachment of Heparin

Heparin coatings have been used on blood-contacting medical devices for decades in order to reduce device thrombogenicity.¹⁰¹ Several proprietary heparin-based medical device coatings have even gained FDA approval for use in the U.S. market.^{101, 102} Specifically, heparin is a polysaccharide with repeating disaccharide units of alternating glucosamine and uronic acid residues; it is structurally and functionally similar to glycosaminoglycan heparin sulfate, which is a naturally occurring anticoagulant on the luminal surface of endothelial cells.²⁶ Heparin's functionality as a natural anticoagulant is dependent upon binding the plasma protein antithrombin (AT) to its active pentasaccharide molecular sequence; once this occurs, the structure of AT is altered and the AT-mediated inhibition of clotting factors – including thrombin and factor X – is accelerated.¹⁰¹ In this inhibition reaction heparin serves as a catalyst, and is therefore not consumed.¹⁰¹ Additionally, heparin has been shown to possess antiproliferative effects, in that it has been shown to inhibit many growth factors that induce vascular smooth muscle cell proliferation and migration.¹⁰³ As a result for the last

50 or so years heparin has been the mainstay of clinical antithrombotic therapy, and has well documented side effect and efficacy profiles.²⁶

To integrate heparin into the developed coating technology, the coupling agent 3-aminopropyl-triethoxy-silane (APTES) was used; specifically, heparin was covalently attached to the APTES layer in the developed coating technology via incubation in two different buffers – one slightly acidic (MES) and one basic (sodium carbonate-sodium bicarbonate) – in order to potentiate the amino-binding affinity of APTES to the heparin molecule. A schematic of how heparin binds to the underlying APTES layer in either buffer is shown as Figure 40.

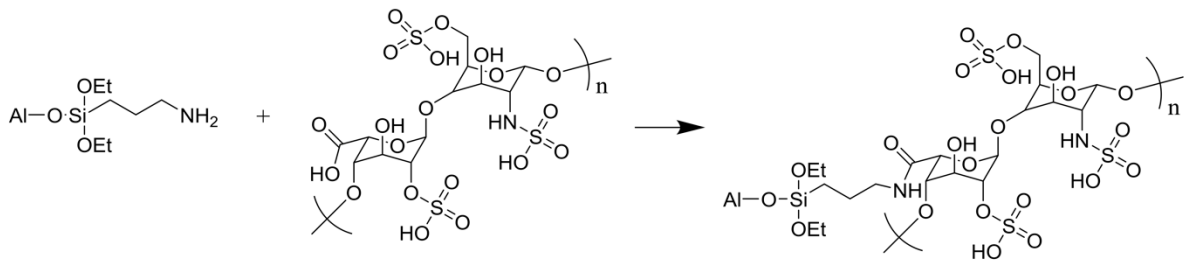


Figure 40: A schematic of how heparin binds to the silane APTES layer in the developed coating technology.

Note that hydroxyl groups in the APTES layer, likely formed by reaction of residual water from the heparin reaction or washing steps, or else the atmosphere, with ethoxy groups on the silane molecule, could also covalently bond heparin. In other words, APTES layer surface hydroxyls could also covalently bond heparin via its carboxylic acid.

Heparin Attachment in MES Buffer and Characterization by XPS

Initially a 1 cm x 1cm p-doped silicon wafer was milled from a larger such wafer using computer numerical controlled (CNC) machining and a diamond tipped blade in the University of Iowa's Optical Science and Technology Center (OSTC). Next this small, square wafer was functionalized with 300 cycles of PE-ALD deposited Al₂O₃ and the silane APTES following the protocol outlined in Chapter 2. Subsequently it was placed in the MES buffer consisting of 2-(N-morpholino)ethane sulfonic acid (50 mL, 0.05 M, 40% (v/v) ethanol/deionized water, pH = 5.5), N-(3-Dimethylaminopropyl)-N'-ethylcarbodiimide hydrochloride (95 mg, 0.5 mmol), and N-Hydroxysuccinimide (12 mg, 0.1 mmol). Next heparin sodium salt from porcine intestinal mucosa (100 mg, 5 μmol) was added to the MES buffer. The reaction was stirred at room temperature for 6 hours,

after which the mixture was decanted and the wafer was washed three times with each of the following: saturated sodium bicarbonate solution in deionized (DI) water (25 mL), DI water (25 mL), and methanol (25 mL). The wafer was then dried under a stream of ultra-high purity N₂ gas. This particular reaction protocol was adapted from Tebbe et al.¹⁰⁴

XPS was next used to assess the chemical composition of the immobilized heparin on the wafer surface using the Kratos Axis Ultra instrument at the University of Iowa. To acquire the survey scan, a monochromated Al K α source was used with a pass energy of 160 eV; the resulting survey scan is shown as Figure 41 with the relative atomic concentrations (At%) shown as a figure insert.

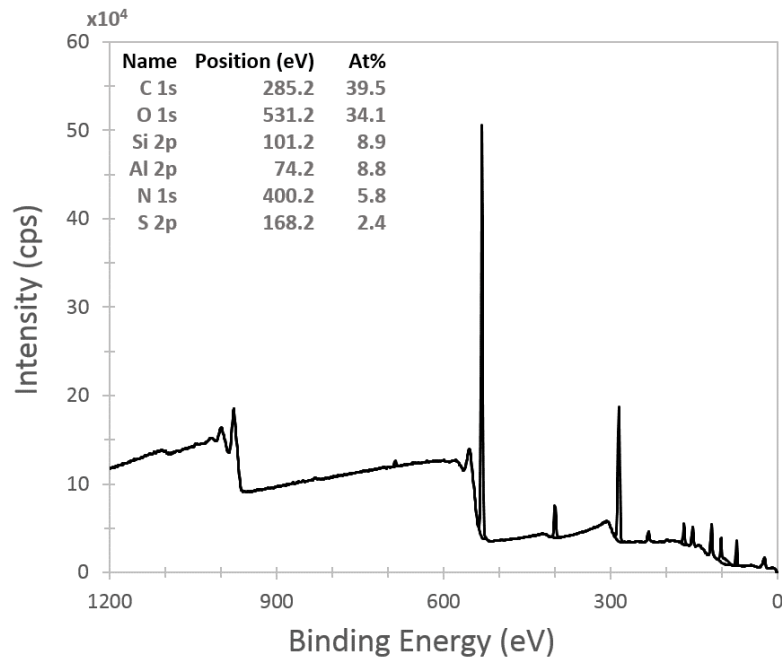


Figure 41: The acquired XPS survey scan on a 1 cm x 1 cm p-doped silicon wafer coated with 300 cycles PE-ALD deposited Al₂O₃, the silane APTES, and heparin with the coupling reaction done in MES buffer.

Figure 41 indicates that the characteristic element of heparin, sulfur (S), is present on the wafer surface. Furthermore, the signal intensity of the aluminum (Al) peak in Figure 41 is decreased relative to the same peak in the XPS survey scan of a similar 1 cm x 1cm p-doped silicon wafer coated with just 300 cycles of PE-ALD deposited Al₂O₃ and the silane APTES, shown as Figure 42.

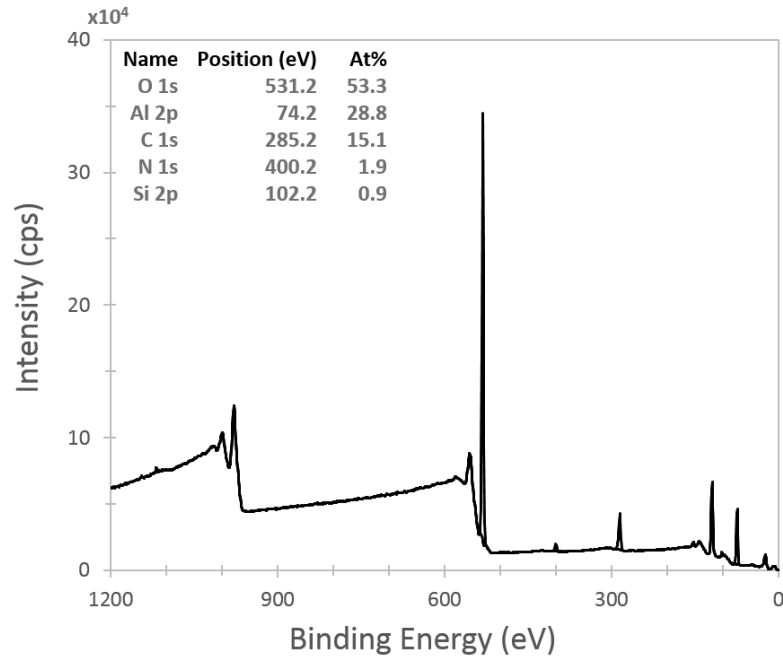


Figure 42: The acquired XPS survey scan on a 1 cm x 1 cm p-doped silicon wafer coated with 300 cycles PE-ALD deposited Al_2O_3 and the silane APTES.

A decreased Al peak in the XPS survey scan of the wafer exposed to the heparin coupling reaction in MES buffer (Figure 41) further indicates the presence of an over layer. Finally, the nitrogen (N) binding chemistry changes for the wafer exposed to the heparin coupling reaction in MES buffer; specifically, core level scans of nitrogen were taken (with a pass energy of 20 eV using the monochromated Al $K\alpha$ source) on both the APTES coated and heparin-MES silicon wafers and are shown as Figure 43.

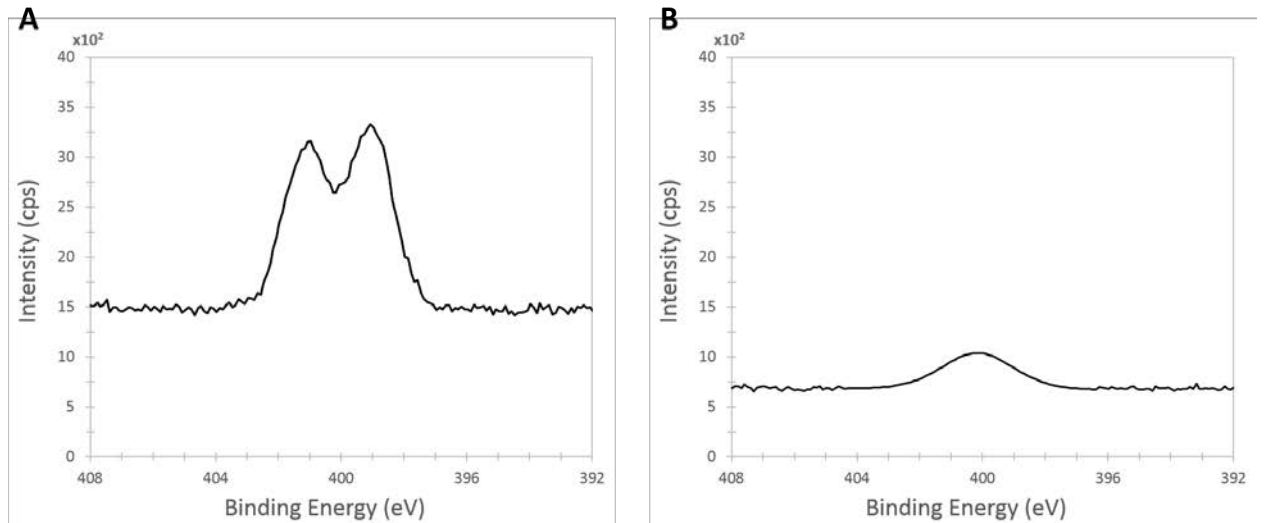


Figure 43: (A) The acquired XPS core level scan for nitrogen taken on a 1 cm x 1 cm p-doped silicon wafer coated with 300 cycles PE-ALD deposited Al_2O_3 , the silane APTES, and heparin with the coupling reaction done in MES buffer. (B) The acquired XPS core level scan for nitrogen taken on a 1 cm x 1 cm p-doped silicon wafer coated with 300 cycles PE-ALD deposited Al_2O_3 and the silane APTES.

Presence of the doublet in the nitrogen core level peak for the heparin-MES wafer (Figure 43A) is indicative of conjugation of heparin to the underlying amino-terminated APTES layer (Figure 43B).

Since the XPS survey and core level scans (shown in Figures 41, 42, and 43) suggest conjugation of heparin to a APTES-functionalized wafer surface in MES buffer, the surface of an intracranial flow diverting device piece was coated accordingly and further evaluated by XPS. Specifically, a commercial flow diverting device #5 piece (with diameter of 4.7 mm and length approximately 5 mm) was coated following the developed heparin-MES conjugation protocol and stored under inert N_2 gas. The resulting coating composition of this device piece was probed by an XPS technician approximately one week later at the University of Illinois at Urbana-Champaign (UIUC) Frederick Seitz Materials Research Laboratory using a Kratos Axis Ultra XPS instrument, since the Kratos Axis Ultra instrument at the University of Iowa was broken. The acquisition parameters of all UIUC XPS scans were kept the same, save for the core level scans, which were acquired at the UIUC with a beam emission current of 15 mA (compared to 10 mA at the University of Iowa) and anode voltage of 14 kV (compared to 15 kV at the University of Iowa) to avoid UIUC beam breakdown issues. The associated XPS survey and nitrogen core level scans of the heparin-MES flow diverting device #5 piece are shown as Figure 44.

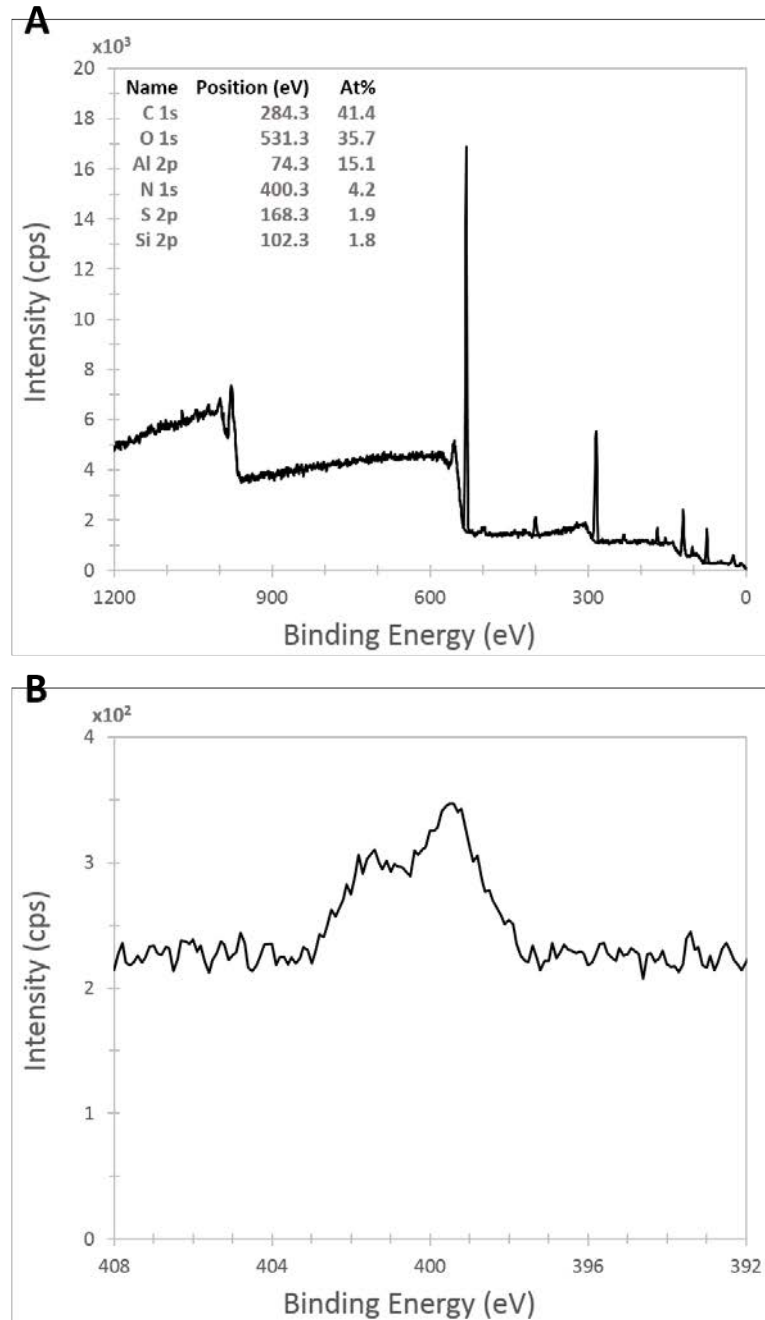


Figure 44: (A) The acquired XPS survey scan on a commercial flow diverting device #5 piece coated with 300 cycles PE-ALD deposited Al_2O_3 , the silane APTES, and heparin with the coupling reaction done in MES buffer. (B) The acquired XPS core level scan for nitrogen on the same device.

Like the XPS survey scan of the heparin-MES wafer (Figure 41), Figure 44A indicates that the characteristic element of heparin, sulfur (S), is present on the #5 device surface. Further, the presence of the doublet in the nitrogen core level peak of the coated #5 device (Figure 44B) is similar to the doublet associated with the heparin-MES wafer

(Figure 43A) and is indicative of heparin conjugation to the underlying amino-terminated APTES layer.

Heparin Attachment in Sodium Carbonate-Sodium Bicarbonate Buffer and Characterization by XPS

To try and potentiate the amino-binding affinity of APTES to the heparin molecule, running the conjugation reaction in a more basic sodium carbonate-sodium bicarbonate buffer was tried. To do this, a 1 cm x 1cm p-doped silicon wafer was initially milled from a larger such wafer using CNC machining and a diamond tipped blade in the University of Iowa's OSTC. Next this small, square wafer was functionalized with 300 cycles of PE-ALD deposited Al_2O_3 and the silane APTES following the protocol outlined in Chapter 2. Subsequently it was placed in a buffer of sodium carbonate-sodium bicarbonate (50 mL, 0.05 M in DI H_2O , pH = 10.3). Next N-(3-dimethylaminopropyl)-N'-ethylcarbodiimide hydrochloride (95 mg, 0.5 mmol) and N-hydroxysuccinimide (12 mg, 0.1 mmol) was added to the buffer, as well as heparin sodium salt from porcine intestinal mucosa (100 mg, 5 μmol). The reaction was stirred at room temperature for 6 hours; afterward the mixture was decanted and the wafer was washed three times with each of the following: saturated sodium bicarbonate solution in DI water (25 mL), DI water (25 mL), and methanol (25 mL). The wafer was then dried under a stream of ultra-high purity N_2 gas.

XPS was next used to assess the chemical composition of the immobilized heparin on the wafer surface using the Kratos Axis Ultra instrument at the University of Iowa. To acquire the survey scan, a monochromated Al $K\alpha$ source was used with a pass energy of 160 eV; the resulting survey scan is shown as Figure 45 with the relative atomic concentrations (At%) shown as a figure insert.

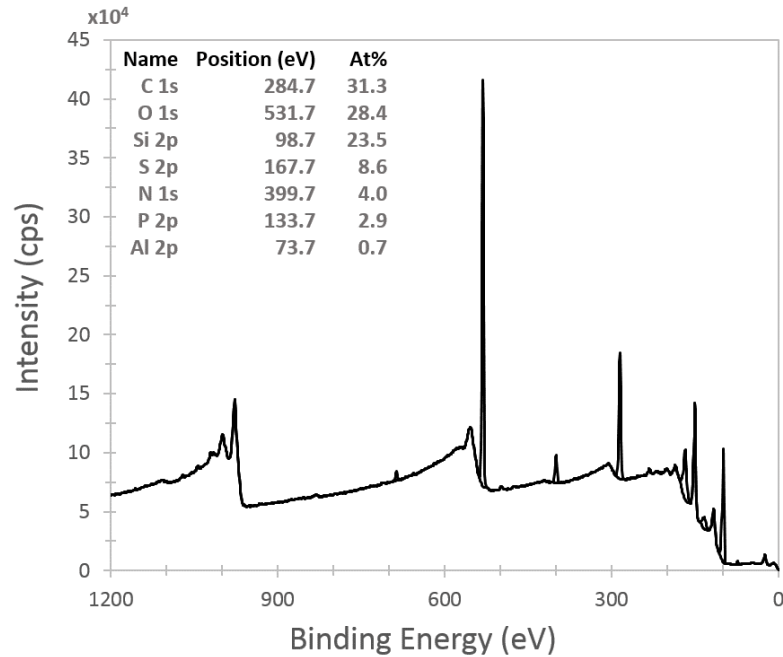


Figure 45: The acquired XPS survey scan on a 1 cm x 1 cm p-doped silicon wafer coated with 300 cycles PE-ALD deposited Al_2O_3 , the silane APTES, and heparin with the coupling reaction done in sodium carbonate-sodium bicarbonate buffer.

Figure 45 indicates that sulfur (S), the characteristic element of heparin, is present on the wafer surface. Furthermore, the signal intensity of the aluminum (Al) peak in Figure 45 is significantly decreased relative to the same peak in the XPS survey scan of a similar 1 cm x 1cm p-doped silicon wafer coated with just 300 cycles of PE-ALD deposited Al_2O_3 and the silane APTES, shown as Figure 42; a decreased Al peak further indicates the presence of an over layer. Finally, the nitrogen (N) binding chemistry changes for the wafer exposed to the heparin coupling reaction in sodium carbonate-sodium bicarbonate buffer; specifically, a core level scan of nitrogen was taken with a pass energy of 20 eV using the monochromated Al $K\alpha$ source at the University of Iowa on the same heparin-bicarbonate silicon wafer and is shown as Figure 46.

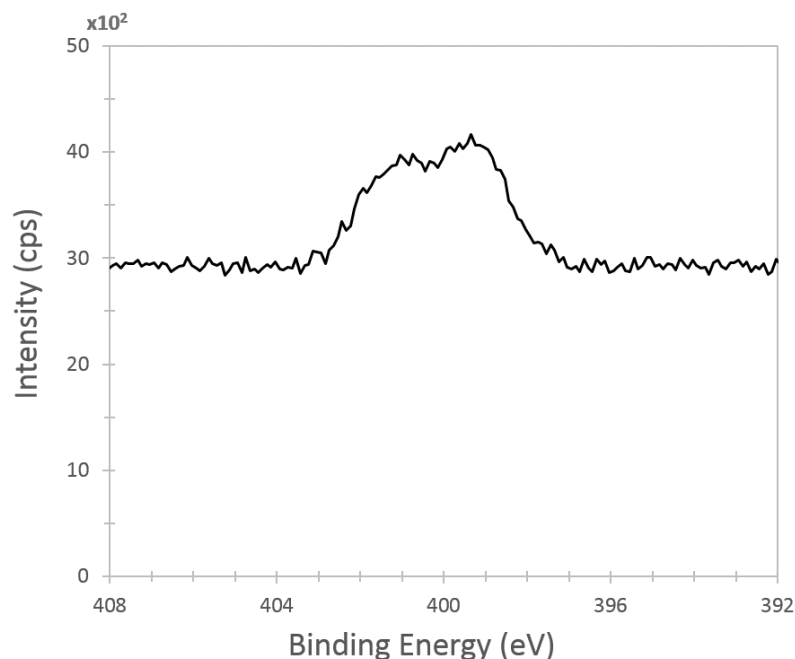


Figure 46: The acquired XPS core level scan for nitrogen taken on a 1 cm x 1 cm p-doped silicon wafer coated with 300 cycles PE-ALD deposited Al_2O_3 , the silane APTES, and heparin with the coupling reaction done in sodium carbonate-sodium bicarbonate buffer.

Presence of the doublet in the nitrogen core level peak in Figure 46 for the heparin-bicarbonate wafer is indicative of heparin conjugation to the underlying amino-terminated APTES layer (Figure 43B).

Since the XPS survey and core level scans (shown in Figures 45 and 46) suggest conjugation of heparin to a APTES-functionalized wafer surface in sodium carbonate-bicarbonate buffer, the surface of an intracranial flow diverting device piece was coated accordingly and further evaluated by XPS. Specifically, a commercial flow diverting device #5 piece (with diameter of 4.7 mm and length approximately 5 mm) was coated following the developed heparin-bicarbonate conjugation protocol and stored under inert N_2 gas. The resulting coating composition of this device piece was probed by an XPS technician approximately one week later at the UIUC Frederick Seitz Materials Research Laboratory using a Kratos Axis Ultra XPS instrument, since the Kratos Axis Ultra instrument at the University of Iowa was broken. The associated XPS survey scan, and nitrogen core level scan, of the heparin-bicarbonate flow diverting device #5 piece are shown as Figure 47.

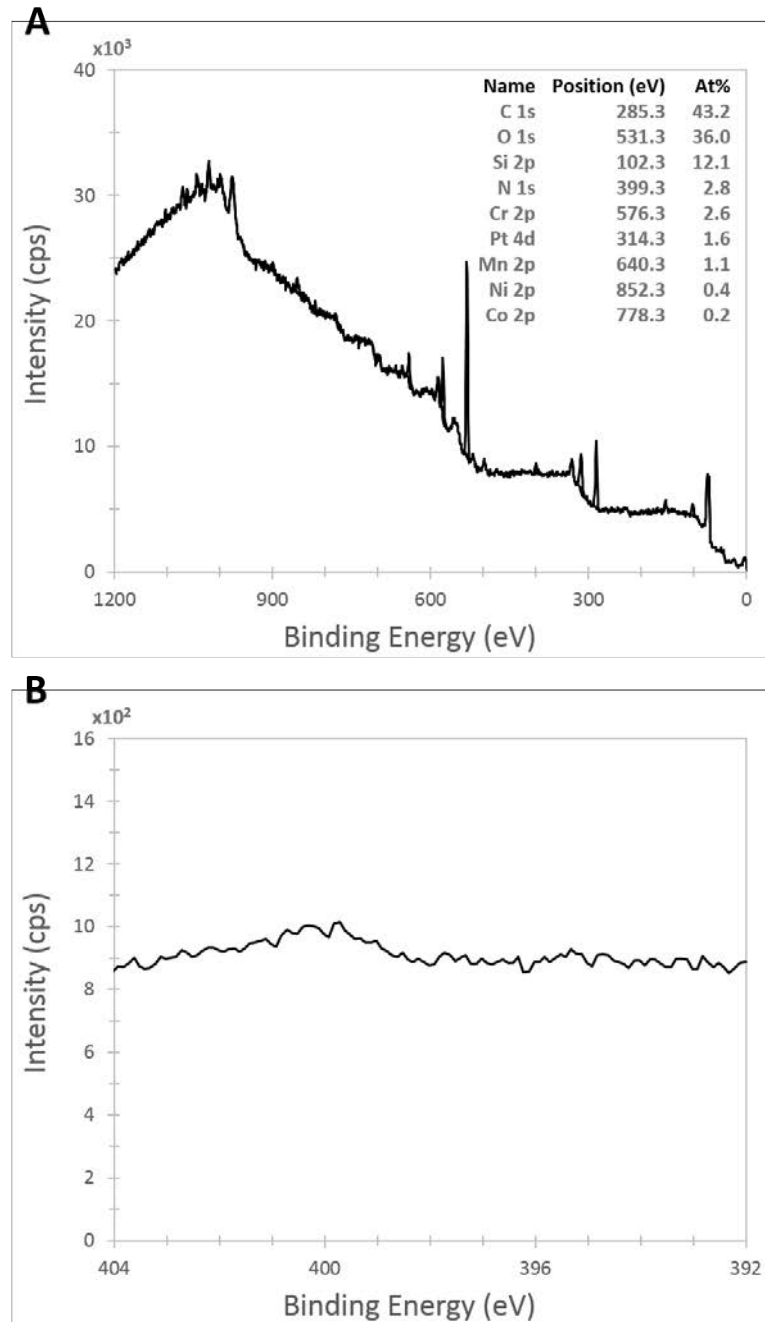


Figure 47: (A) The acquired XPS survey scan on a commercial flow diverting device #5 piece coated with 300 cycles PE-ALD deposited Al_2O_3 , the silane APTES, and heparin with the coupling reaction done in sodium carbonate-bicarbonate buffer. (B) The acquired XPS core level scan for nitrogen on the same device.

Unlike the XPS survey scan of the heparin-bicarbonate wafer (Figure 45), Figure 47A indicates that the characteristic element of heparin, sulfur (S), is not present on the coated #5 device surface; likewise, the topography of the survey scan peaks in Figure 47A is markedly different from those of the heparin-bicarbonate wafer shown in Figure

45. In fact, the topography of the survey scan peaks in Figure 47A is similar to the peak topography in the XPS survey scan acquired on a bare flow diverting device #5 and shown as Figure 48.

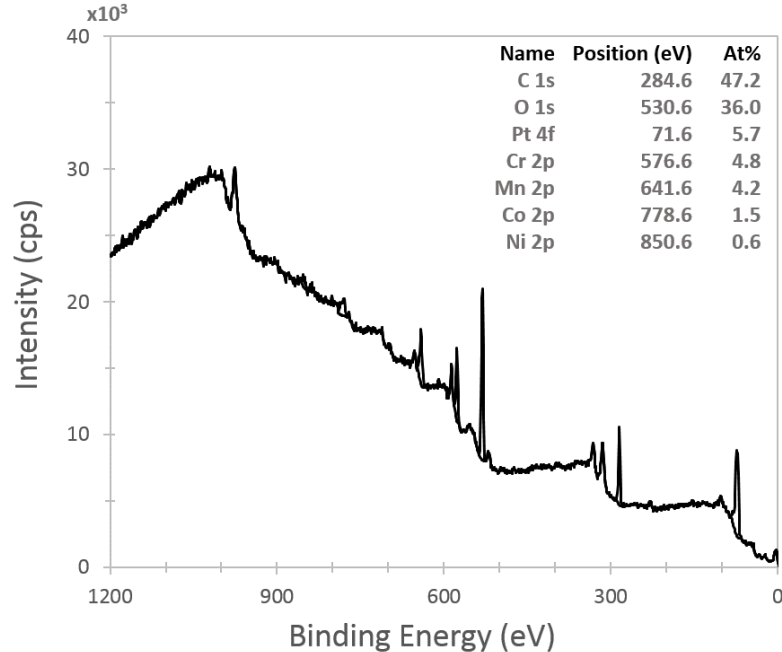


Figure 48: The acquired XPS survey scan on a bare commercial flow diverting #5 device.

It is well known that detected platinum 4f (Pt 4f) electrons overlap in binding energy with aluminum 2p electrons in XPS⁶⁴; thus, the survey scans in Figure 47A and Figure 48 are nearly identical. Further, no doublet is present in the nitrogen core level peak of the coated device (Figure 47B) and its intensity is distinctly low, barely rising from the baseline signal. Together this information suggests that heparin is not conjugated to the #5 flow diverting device; moreover, this particular reaction seemed to effectively etch away the underlying aluminum and silane coating layers, ultimately leading to exposure of the bare #5 device wires. Because the reaction was carried out in the sodium carbonate-bicarbonate buffer under basic conditions (with pH of approximately 10.3) it is possible for these conditions to facilitate surface etching.

Development of the Coating Technology as a Platform for the Attachment of Phosphorylcholine (PC)

Phosphorylcholine (PC) is the primary component of phospholipids present on the cell membranes of red blood cells; specifically it is zwitterionic and contains not only

polar head groups but also long hydrocarbon chains.³³ Because PC does not readily adsorb proteins, PC-based polymer coatings have been used commercially to enhance the biocompatibility of coronary stents; most notably the BiodivYsio™ coronary stent and delivery system, coated with a PC copolymer, gained FDA approval in 2000.^{33, 100} A multicenter randomized human trial called SOPHOS evaluated the safety and efficacy of BiodivYsio™ devices relative to their stainless steel counterparts and concluded that BiodivYsio™ devices were a safe and effective primary treatment method for patients with either stable or unstable angina pectoris and native coronary artery lesions; however, the trial failed to demonstrate the superiority of BiodivYsio™ devices compared to stainless steel devices.³³ Nevertheless, drug-eluting stents containing PC drug carrier polymers have been shown to reduce clinical and angiographic restenosis in humans.³³ As a result, Medtronic has developed a PC-based Shield Technology™ for their Pipeline Flex™ flow diverting device and has touted its small scale (3 nm thick), durability, and the increased lubricity it imparts during device deployment.²⁰ A clinical trial assessing the incidences of stroke and neurological adversities or death associated with the Shield Technology™ in the UK has been conducted, the final data collection date was December 2016, and the results should be released soon.⁴⁸ PC was chosen for integration into the developed coating technology because it has demonstrated some longitudinal thromboresistance in-vivo, and since it is the primary component of Medtronic's competitive Shield Technology™. Specifically, the PC derivative chosen for incorporation in the developed technology was o-phosphorylethanolamine (o-PA) because it contains the hydrophilic polar head group, characteristic of PC, attached to a reactive primary amine; o-PA was integrated into the developed technology by covalently attaching its primary amine to the TCT layer (or in one case, the APTES layer) by incubation in several different buffers with pH ranging from mildly acidic to basic – this was done in an attempt to potentiate the binding affinity of o-PA to TCT (or else, APTES).

o-PA Attachment in Citric Acid and Characterization via XPS

Initially a 0.05 M solution of citric acid in DI water was prepared, in addition to a 0.05 M solution of sodium citrate in DI water. Next 88.5 mL of the sodium citrate solution was combined with 11.5 mL of citric acid solution to create a buffer with a pH of approximately 6. Subsequently, o-PA (0.100 g, 0.7 mmol) was dissolved in 10 mL of

citric acid buffer in a small Erlenmeyer flask. A 1 cm x 1cm p-doped silicon wafer that had previously been CNC machined in the University of Iowa's OSTC, coated with 300 cycles of PE-ALD deposited Al_2O_3 , the silane APTES, and the coupler TCT was added to the flask; the reaction was allowed to stir at room temperature for 10 hours. Afterward the wafer was washed three times with DI water and three times with methanol, then dried under a stream of ultra-high purity N_2 gas.

XPS was next used to assess the chemical composition of the immobilized o-PA on the wafer surface using the Kratos Axis Ultra instrument at the UIUC, since the Kratos instrument at the University of Iowa was broken. To acquire the survey scan, a monochromated Al $K\alpha$ source was used with a pass energy of 160 eV; the resulting survey scan is shown as Figure 49 with the relative atomic concentrations (At%) shown as a figure insert.

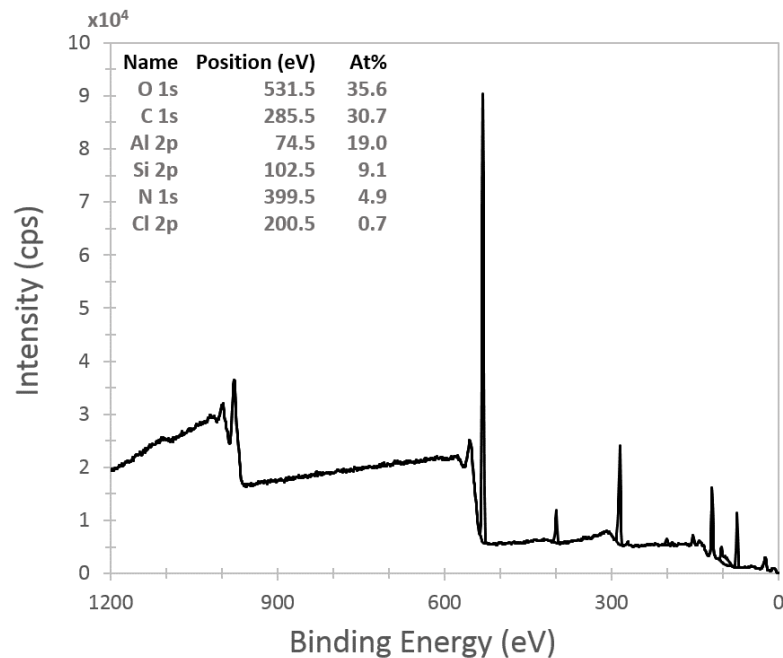


Figure 49: The acquired XPS survey scan on a 1 cm x 1 cm p-doped silicon wafer coated with 300 cycles PE-ALD deposited Al_2O_3 , the silane APTES, the coupler TCT, and o-PA with the coupling reaction done in citric acid buffer.

Figure 49 indicates that the characteristic element of o-PA, phosphorus (P), is not present on the wafer surface; as a result, o-PA is not likely conjugated to the TCT layer, meaning that citric acid is not an appropriate buffer for the reaction.

o-PA Attachment in a Sodium Bicarbonate Buffer and Characterization via XPS

Since running the o-PA conjugation reaction in citric acid buffer, with pH of approximately 6, did not yield surface conjugated o-PA, a sodium bicarbonate buffer with higher pH was tried. To do this a 0.05 M solution of sodium carbonate (Na_2CO_3) in DI water was prepared; a 0.05 M solution of sodium bicarbonate (NaHCO_3) in DI water was also prepared. Next 70 mL of 0.05 M Na_2CO_3 solution was combined with 30 mL of NaHCO_3 solution to create a bicarbonate buffer with a pH of approximately 10.3. Subsequently o-PA (0.100 g, 0.7 mmol) was dissolved in 10 mL of bicarbonate buffer in a small Erlenmeyer flask. A 1 cm x 1cm p-doped silicon wafer that had previously been CNC machined in the University of Iowa's OSTC, coated with 300 cycles of PE-ALD deposited Al_2O_3 , the silane APTES, and the coupler TCT was added to the flask. The reaction was allowed to stir at room temperature for 10 hours. Afterward the wafer was washed three times with DI water and three times with methanol, then dried under a stream of ultra-high purity N_2 gas.

XPS was next used to assess the chemical composition of the immobilized o-PA on the wafer surface using the Kratos Axis Ultra instrument at the UIUC, since the Kratos instrument at the University of Iowa was broken. To acquire the survey scan, a monochromated Al $K\alpha$ source was used with a pass energy of 160 eV; the resulting survey scan is shown as Figure 50 with the relative atomic concentrations (At%) shown as a figure insert.

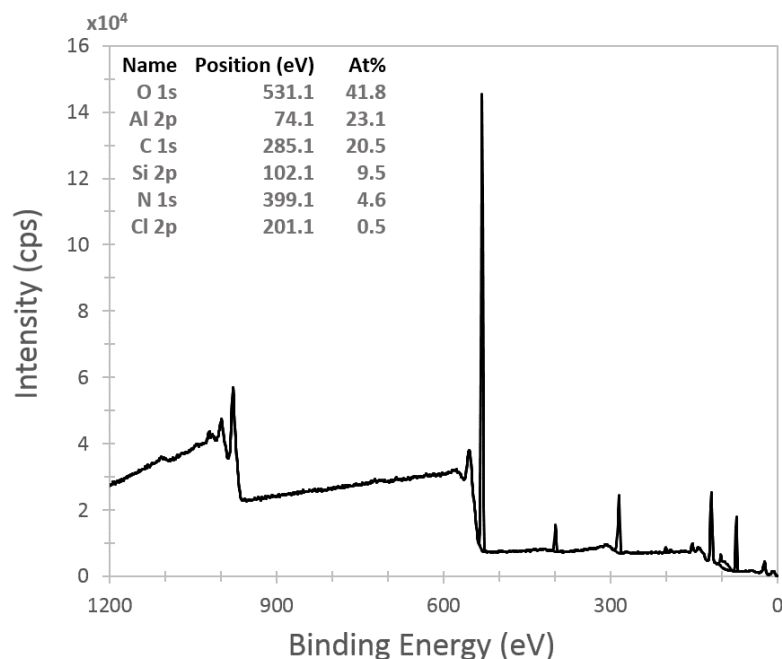


Figure 50: The acquired XPS survey scan on a 1 cm x 1 cm p-doped silicon wafer coated with 300 cycles PE-ALD deposited Al_2O_3 , the silane APTES, the coupler TCT, and o-PA with the coupling reaction done in a sodium bicarbonate buffer.

Figure 50 indicates that the characteristic element of o-PA, phosphorus (P), is not present on the wafer surface; as a result, o-PA is not likely conjugated to the TCT layer, meaning that the sodium bicarbonate buffer is not an appropriate buffer for the reaction.

o-PA Attachment via a Modified Coupling Protocol and Associated XPS Characterization

Since running the o-PA conjugation reaction in the citric acid and sodium bicarbonate buffers did not yield surface bound o-PA, conjugating o-PA in a slightly acidic MES buffer – similar to the heparin conjugation reaction in MES – was tried. To do this a 0.05 M MES buffer was prepared by dissolving 4-morpholineethanesulfonic acid (0.976 g, 5.0 mmol) in solution of 60 mL DI water and 40 mL ethanol. The resulting MES buffer was adjusted to a pH of approximately 5.5 by adding 10 M sodium hydroxide (NaOH) solution dissolved in DI water (0.05 mL) to the dissolved MES. Next o-PA (0.100 g, 0.7 mmol), N-hydroxysuccinimide (12 mg, 0.1 mmol), and N-Ethyl-N'-(3-dimethylaminopropyl)carbodiimide hydrochloride (95 mg, 0.5 mmol) were dissolved in 50 mL MES buffer. Once fully dissolved, a 1 cm x 1cm p-doped silicon wafer that had previously been CNC machined in the University of Iowa's OSTC, coated with 300 cycles of PE-ALD deposited Al_2O_3 and the silane APTES was added to the reaction

mixture and the reaction was allowed to stir for 6 hours at room temperature. Afterward the wafer was washed three times with each of the following: saturated sodium bicarbonate in DI water, DI water, and methanol. The wafer was then dried under a stream of ultra-high purity N₂ gas.

XPS was next used to assess the chemical composition of the immobilized o-PA on the wafer surface using the Kratos Axis Ultra instrument at the UIUC, since the Kratos instrument at the University of Iowa was broken. To acquire the survey scan, a monochromated Al K α source was used with a pass energy of 160 eV; the resulting survey scan is shown as Figure 51 with the relative atomic concentrations (At%) shown as a figure insert.

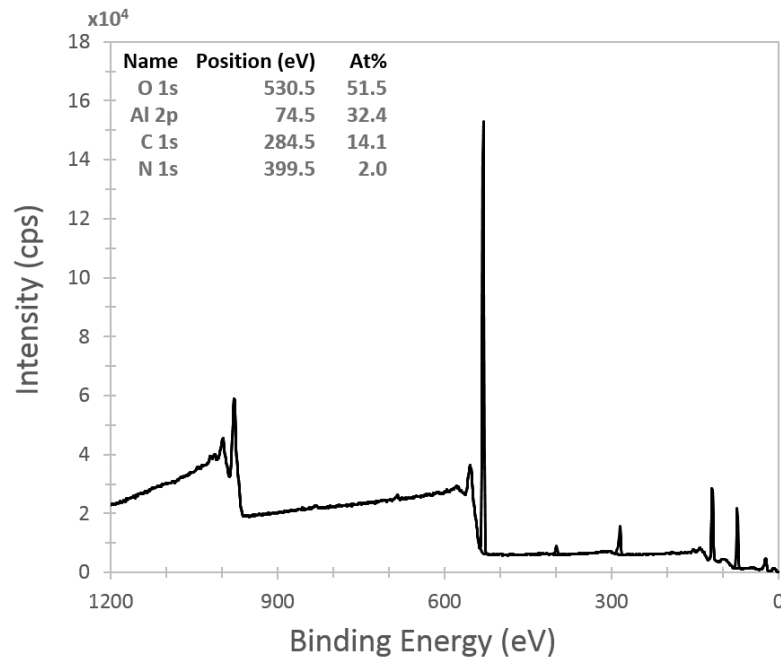


Figure 51: The acquired XPS survey scan on a 1 cm x 1 cm p-doped silicon wafer coated with 300 cycles PE-ALD deposited Al₂O₃, the silane APTES, and o-PA with the coupling reaction done in a MES buffer.

Figure 51 indicates that the characteristic element of o-PA, phosphorus (P), is not present on the wafer surface; furthermore, Figure 51 shows there is no silicon (Si) on the wafer surface, which seems to indicate degradation of the silane layer during this reaction. It is possible that the pH of the MES buffer dropped too low during the reaction, which would have facilitated silane layer degradation. Together this information suggests that o-PA is not conjugated to the wafer surface, and ultimately

lends insight that the modified coupling protocol is not easily controlled and therefore is an inappropriate methodology for conjugation of o-PA to the APTES layer.

o-PA Attachment in DI Water and Characterization by XPS

Since running the o-PA conjugation reaction in the citric acid, sodium bicarbonate, and MES buffers did not yield surface bound o-PA, conjugating o-PA in DI water was tried. To do this, o-PA (0.100 g, 0.7 mmol) was dissolved in 10 mL DI water in a small Erlenmeyer flask. A 1 cm x 1cm p-doped silicon wafer that had previously been CNC machined in the University of Iowa's OSTC, coated with 300 cycles of PE-ALD deposited Al_2O_3 , the silane APTES, and the coupler TCT was added to the reaction; the reaction was allowed to stir at room temperature for 10 hours. Afterward the wafer was washed three times with DI water and three times with methanol. The wafer was then dried under a stream of ultra-high purity N_2 gas.

XPS was next used to assess the chemical composition of the immobilized o-PA on the wafer surface using the Kratos Axis Ultra instrument at the UIUC, since the Kratos instrument at the University of Iowa was broken. To acquire the survey scan, a monochromated Al $K\alpha$ source was used with a pass energy of 160 eV; the resulting survey scan is shown as Figure 52 with the relative atomic concentrations (At%) shown as a figure insert.

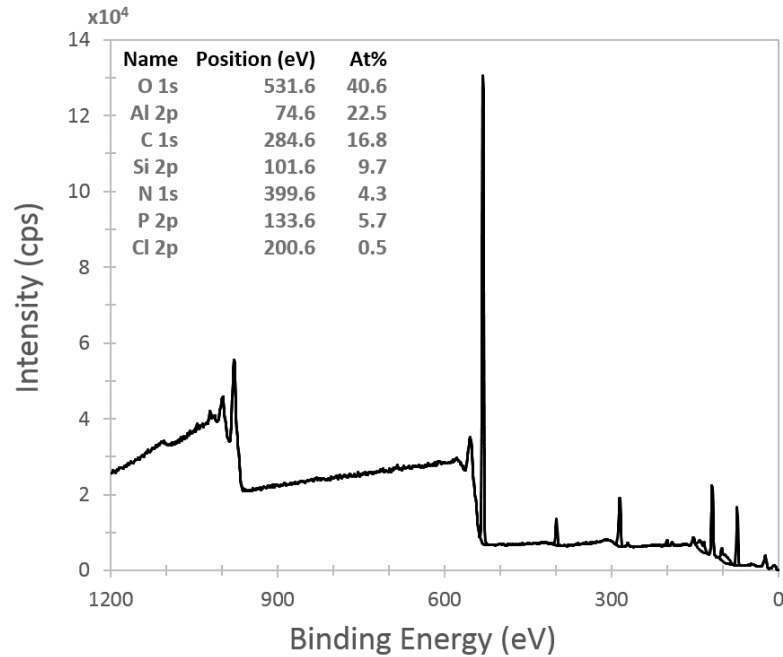


Figure 52: The acquired XPS survey scan on a 1 cm x 1 cm p-doped silicon wafer coated with 300 cycles PE-ALD deposited Al_2O_3 , the silane APTES, the coupler TCT, and o-PA with the coupling reaction done in deionized water.

Figure 52 indicates that the characteristic element of o-PA, phosphorus (P), is present on the wafer surface. To further probe the surface, a core level scan of phosphorus was taken, with pass energy of 20 eV using the same monochromated Al $K\alpha$ source, on the wafer reacted with o-PA in DI water (Figure 53).

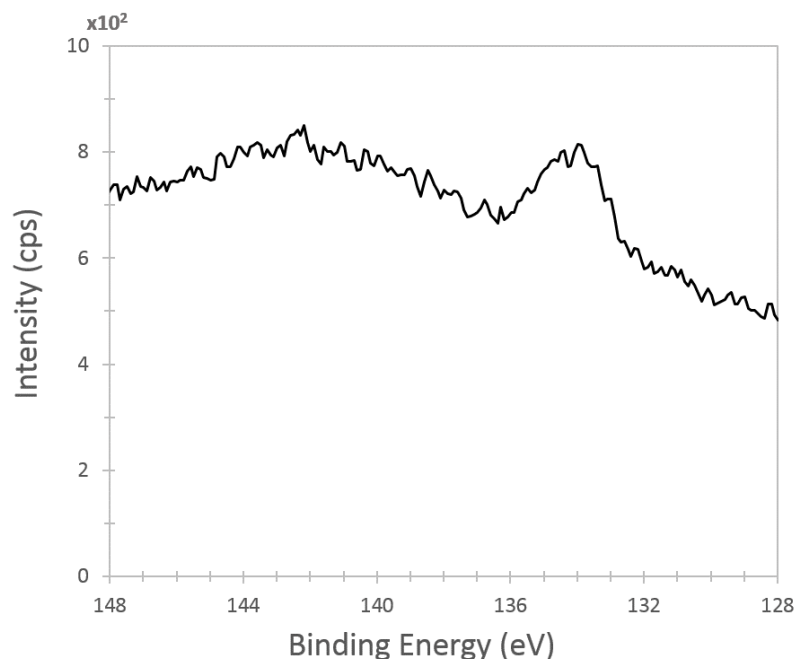


Figure 53: The acquired XPS core level scan for phosphorus taken on a 1 cm x 1 cm p-doped silicon wafer coated with 300 cycles PE-ALD deposited Al_2O_3 , the silane APTES, the coupler TCT, and o-PA with the coupling reaction done in deionized water.

Figure 53 further verifies the presence of phosphorus on the o-PA wafer surface since a clear peak is present at the characteristic binding energy of approximately 134 eV. A schematic of how o-PA binds to the TCT layer of the developed coating technology in DI water is shown as Figure 54.

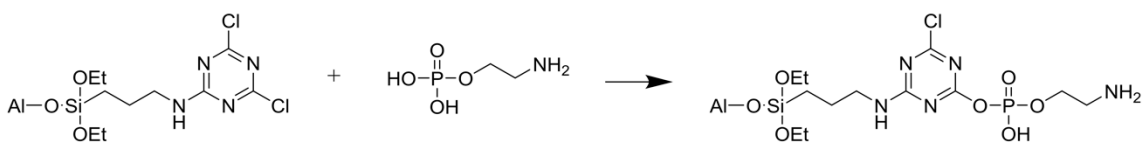


Figure 54: A schematic of how o-PA binds to the coupler TCT layer in the developed coating technology.

Note that since this reaction is done in DI water, o-PA is more likely to attach to the TCT layer of the developed coating technology via oxygen rather than nitrogen. This is because the nitrogen in o-PA is likely protonated and unreactive in DI water, based on the acid dissociation constant (pKa) of DI water relative to the pKa of nitrogen in this molecule; in contrast, oxygen is likely deprotonated and thereby reactive at the pKa of DI water. It is also possible for o-PA to attach to the APTES layer by reaction of its free amine with an ethoxy group on the silane molecule.

Since the XPS survey and core level scans (shown in Figures 52 and 53) suggest conjugation of o-PA to a TCT-functionalized wafer surface in DI water, the surface of an intracranial flow diverting device piece was coated accordingly and further evaluated by XPS. Specifically, a commercial flow diverting device #5 piece (with diameter of 4.7 mm and length approximately 5 mm) was coated following the developed o-PA-DI water conjugation protocol and stored under inert N₂ gas. The resulting coating composition of this device piece was probed by an XPS technician approximately one week later at the UIUC Frederick Seitz Materials Research Laboratory using a Kratos Axis Ultra XPS instrument, since the Kratos Axis Ultra instrument at the University of Iowa was broken. The associated XPS survey scan of the o-PA-DI water flow diverting device #5 piece is shown as Figure 55.

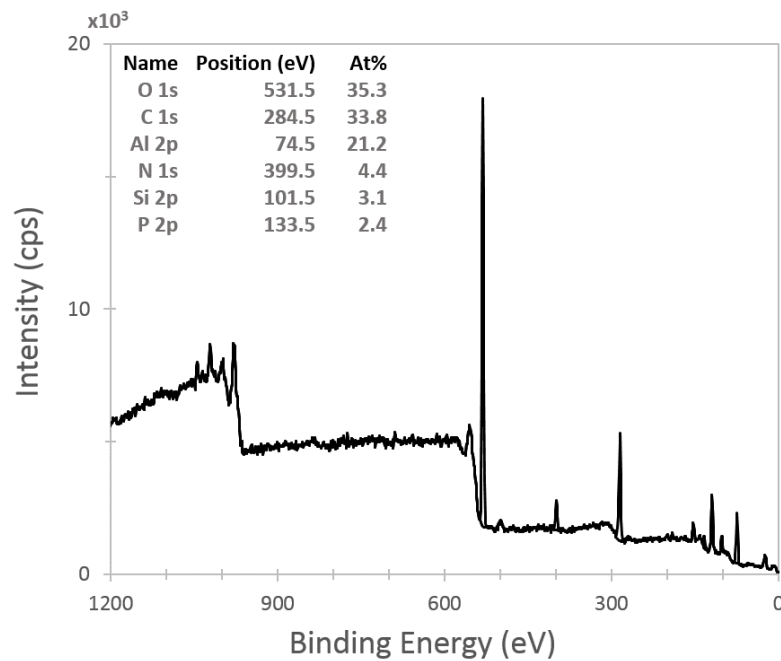


Figure 55: The acquired XPS survey scan on a commercial flow diverting device #5 piece coated with 300 cycles PE-ALD deposited Al₂O₃, the silane APTES, the coupler TCT, and o-PA with the coupling reaction done in deionized water.

Like Figure 52, Figure 55 indicates that the characteristic element of o-PA, phosphorus (P), is present on the #5 device surface. Further, the nitrogen (N) binding chemistry changes upon reaction with o-PA; in particular, the nitrogen peak shifts to a lower electron binding energy. To quantify this binding energy shift, core level scans of nitrogen were taken, with pass energy of 20 eV using the same monochromated Al K α source, on both the #5 device piece reacted with o-PA in DI water (Figure 56A) and a

similar #5 device coated with 300 cycles of PE-ALD deposited Al_2O_3 , the silane APTES, and the coupler TCT (Figure 56B).

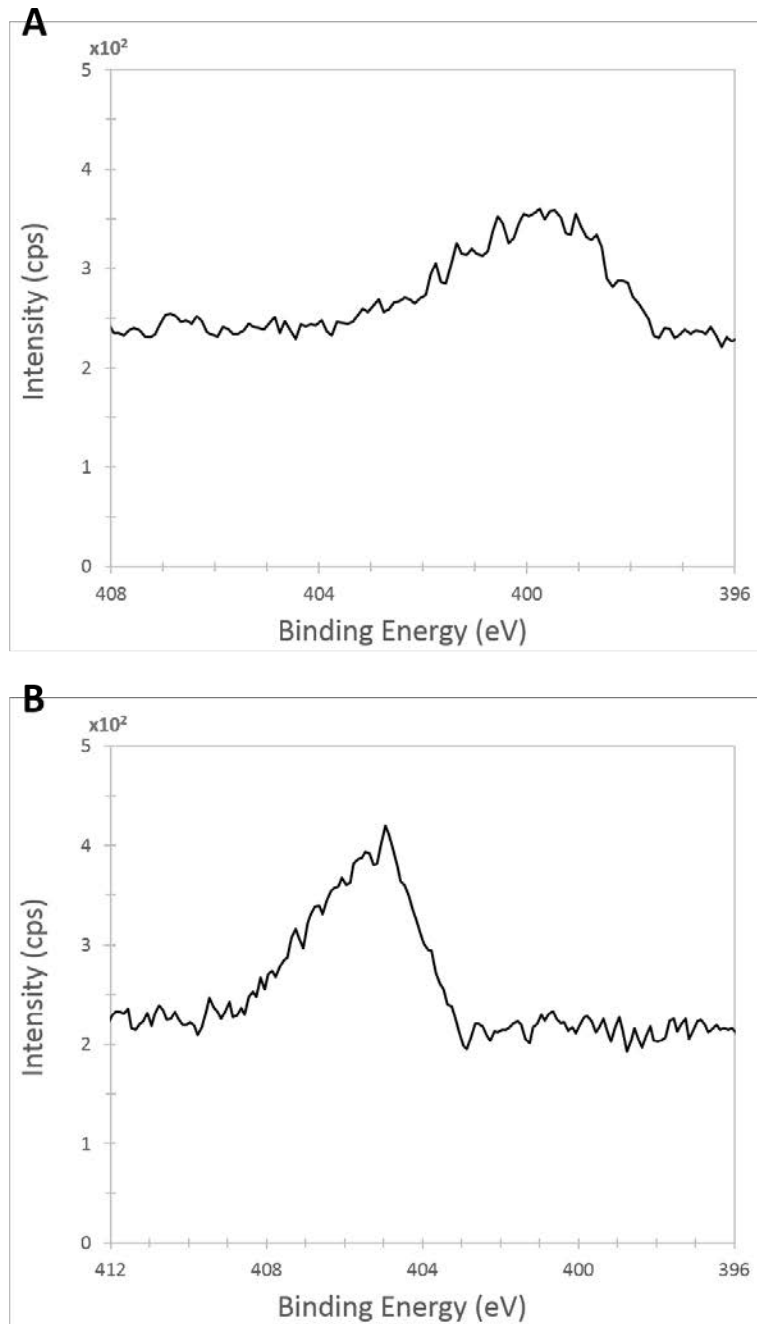


Figure 56: (A) The acquired XPS core level scan for nitrogen on a commercial flow diverting device #5 piece coated with 300 cycles PE-ALD deposited Al_2O_3 , the silane APTES, the coupler TCT, and o-PA with the coupling reaction done in deionized water. (B) The acquired XPS core level scan for nitrogen on a commercial flow diverting device #5 piece coated with 300 cycles PE-ALD deposited Al_2O_3 , the silane APTES, and the coupler TCT.

Figure 56A indicates that an electron shift to a lower binding energy is observed in the nitrogen core level peak upon incubation of a #5 device with o-PA in DI water, relative to a TCT-functionalized #5 device (Figure 56B). This shift is likely indicative of o-PA conjugation to the TCT layer since the oxidation state of nitrogen in o-PA is more negative (fewer imines and more amine groups). Moreover, the decreased signal intensity of the nitrogen peak observed in Figure 56A likely suggests o-PA conjugation since fewer nitrogen atoms are present in the o-PA molecule as compared to TCT; likewise, the nitrogen atoms comprising the underlying TCT layer are now more difficult to detect via XPS since they are sterically shielded by conjugated o-PA, and therefore contribute less to the overall nitrogen signal intensity.

Development of the Coating Technology as a Platform for the Attachment of Methoxy-poly(ethylene glycol) (mPEG)

The covalent conjugation of poly(ethylene glycol) (or PEG) moieties to therapeutic agents was first reported in the 1970s by Abuchowski et al.; their work outlined a strategy for using PEG conjugation to improve the therapeutic value of proteins.¹⁰⁵ Since then the covalent conjugation of PEG moieties to proteins has been extensively studied in the literature, and several PEG-protein conjugates have been commercialized.^{93, 95} The PEG-protein conjugation technique is versatile, with demonstrated efficacy, in part due to the large selection of PEG moieties available for research.⁹³ Namely the technique is advantageous to the conjugated protein in-vivo by prolonging its half-life, reducing immunogenicity, and decreasing the likelihood of aggregation.⁹³

However in the case of the developed technology the conjugation of PEG will not act as a therapeutic agent, but rather as an immobilized agent to reduce the amount of surface adsorbed protein and dampen the associated foreign body response to the intracranial device; in fact, PEG has been a key polymer in reducing protein adsorption to surfaces of all types.⁹⁴ The particular PEG chosen for conjugation to the developed technology was methoxy-poly(ethylene glycol) amine, or mPEG, since one terminal end consists of a primary amine that can be activated, while the other is capped with a methoxy group that acts to prevent undesired intra- or intermolecular crosslinking.⁹³ To integrate mPEG into the technology, the end consisting of the primary amine was covalently attached to the TCT layer by incubation, at varying concentrations, in either

methanol or DI water; in an effort to further potentiate the binding affinity of TCT to mPEG, reacting larger mPEG molecules to TCT was also tried.

mPEG Attachment in Methanol and Characterization by XPS

Initially mPEG (100 mg, 20 μmol) with average molecular weight of 5000 was dissolved in 10 mL of methanol in a small Erlenmeyer flask, yielding a 10 mg/mL mPEG-methanol solution. Subsequently a 1 cm x 1 cm silicon wafer previously CNC machined at the University of Iowa's OSTC and further functionalized with 300 cycles of PE-ALD deposited Al_2O_3 , the silane APTES, and TCT was added to the flask. The reaction was stirred for 24 hours at room temperature; the reaction mixture was then decanted and the wafer was washed three times with methanol (~15 mL) and dried under a stream of ultra-high purity N_2 gas.

XPS was next used to assess the chemical composition of the immobilized mPEG on the wafer surface using the Kratos Axis Ultra instrument at the University of Iowa. To acquire the survey scan, a monochromated Al $K\alpha$ source was used with a pass energy of 160 eV; the resulting survey scan is shown as Figure 57A with the relative atomic concentrations (At%) shown as a figure insert. The survey scan of a similar 1 cm x 1cm p-doped silicon wafer coated with just 300 cycles of PE-ALD deposited Al_2O_3 , the silane APTES, and the coupler TCT is shown as Figure 57B and was also acquired via the Kratos Axis Ultra instrument at the University of Iowa.

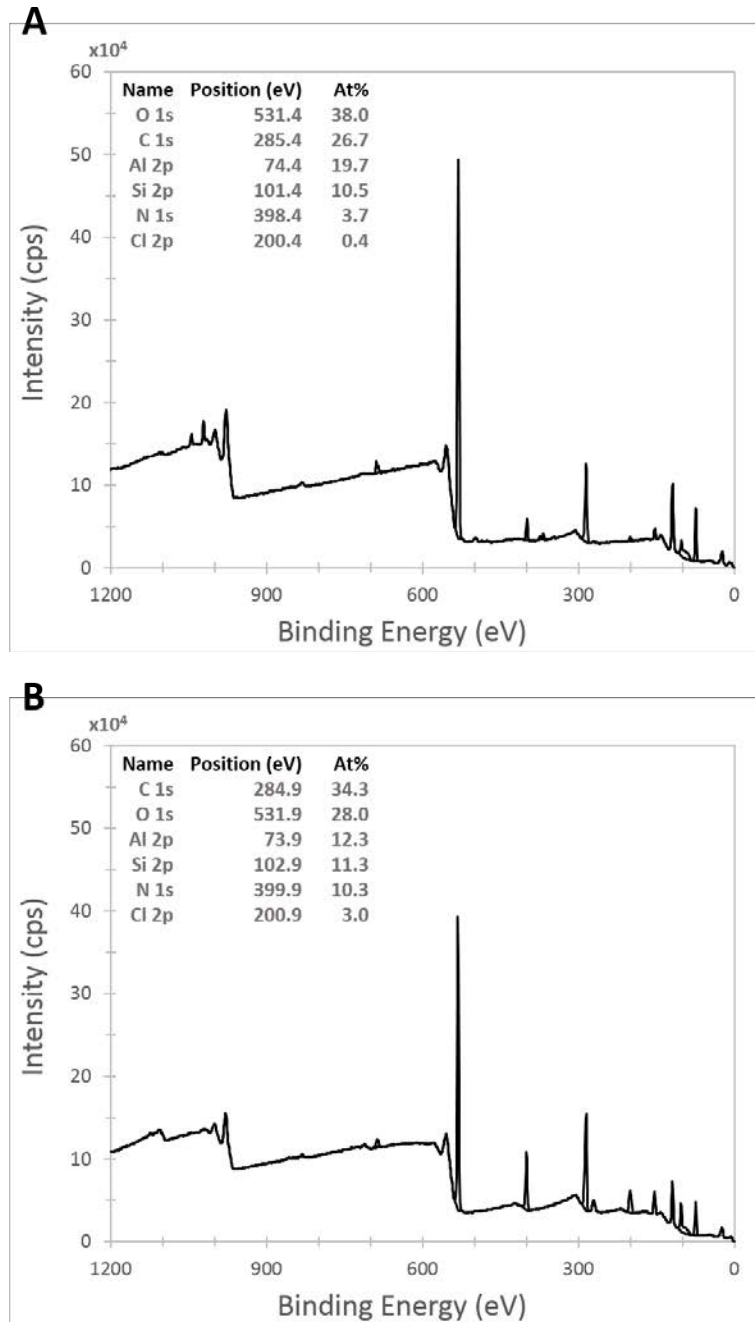


Figure 57: (A) The acquired XPS survey scan on a 1 cm x 1 cm p-doped silicon wafer coated with 300 cycles PE-ALD deposited Al_2O_3 , the silane APTES, the coupler TCT and mPEG with average molecular weight of 5000 dissolved in methanol at 10 mg/mL. (B) The acquired XPS survey scan on a 1 cm x 1 cm p-doped silicon wafer coated with 300 cycles PE-ALD deposited Al_2O_3 , the silane APTES, and the coupler TCT.

Since there is no characteristic element of mPEG, or element unique to this molecule that is not present in the underlying layers, one way to verify the presence of mPEG on the wafer surface is to compare the signal intensities of the elements comprising the

underlying layers post mPEG exposure (Figure 57A) to their respective intensities prior to exposure to mPEG (Figure 57B) – in other words, to compare the relative signal intensities of several known elements in the coating technology pre- and post mPEG incubation. From this perspective, Figure 57A indicates that the aluminum (Al) peak is larger on the wafer incubated in the mPEG 10 mg/mL solution than on the TCT wafer (Figure 57B). This is surprising since addition of an overlayer like mPEG would decrease the Al signal intensity; yet, Figure 57A indicates that the wafer incubated in the mPEG 10 mg/mL solution also has less intense carbon (C), nitrogen (N), and chlorine (Cl) peaks than the TCT wafer. Together this combined information could indicate that perhaps the mPEG wafer was probed by the XPS x-ray beam at a location where no TCT, and therefore no mPEG, is attached. This could be possible since the spot size of the XPS x-ray beam used to interrogate each surface is 300 μm x 700 μm – the XPS SEM images of the TCT layer, shown as Figure 20, reveal that the layer is likely not pin-hole free which is also corroborated by the confocal microscopy images (Figure 23A and 23B), showing inhomogeneous signal intensity of the fluoro-labeled TCT layer on a commercial #1 flow diverting device – thus it may be possible for the XPS x-ray beam to probe a location where no TCT, or else mPEG, is present.

mPEG Attachment in Deionized (DI) Water and Characterization by XPS

To increase the likelihood of conjugating mPEG to the TCT layer, increased concentrations (60 mg/mL at 14 μmol and 100 mg/mL at 23 μmol) of mPEG with a higher average molecular weight (13,000) were each dissolved in 3 mL DI water in small Erlenmeyer flasks. Subsequently, commercial flow diverter device #5 pieces (with diameter of 4.7 mm and length approximately 5 mm) previously coated with 300 cycles of PE-ALD deposited Al_2O_3 , the silane APTES, and the coupler TCT were added to each flask and allowed to react for 24 hours at room temperature. Afterward each device piece was washed three times with DI water and three times with methanol, then dried under a stream of ultra-high purity N_2 gas and stored under N_2 .

The resulting mPEG coating compositions, mPEG-60 and mPEG-100, conjugated to the #5 device pieces were probed by an XPS technician approximately one week later at the UIUC Frederick Seitz Materials Research Laboratory using a Kratos Axis Ultra XPS instrument, since the Kratos Axis Ultra instrument at the University of Iowa was broken. The XPS survey scan of the PEG-60 flow diverting

device #5 piece is shown as Figure 58A; likewise, the XPS survey scan of a similar flow diverting device #5 piece functionalized with 300 cycles of PE-ALD deposited Al_2O_3 , the silane APTES, and TCT is shown as Figure 58B.

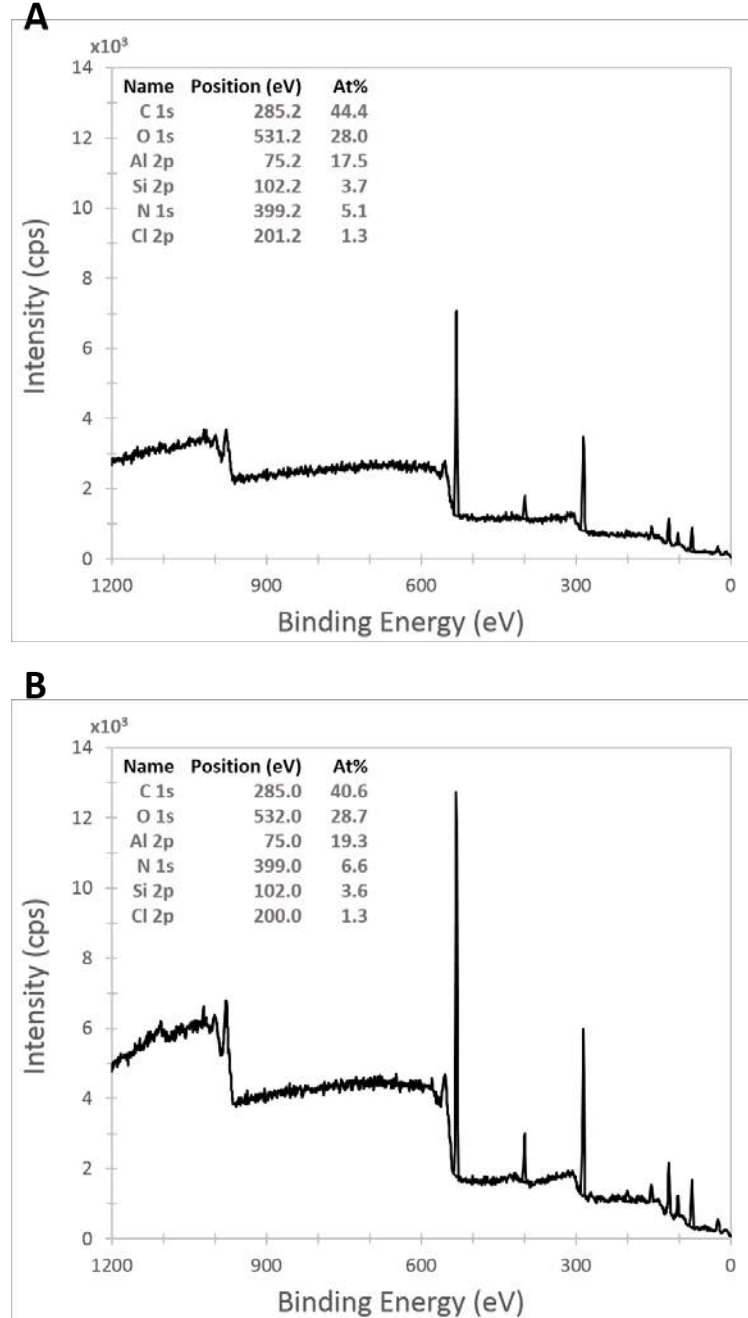


Figure 58: (A) The acquired XPS survey scan on a commercial flow diverting device #5 piece coated with 300 cycles PE-ALD deposited Al_2O_3 , the silane APTES, the coupler TCT, and mPEG with average molecular weight of 13000 dissolved in deionized water at 60 mg/mL. (B) The acquired XPS survey scan on a flow diverting device #5 piece coated with 300 cycles PE-ALD deposited Al_2O_3 , the silane APTES, and the coupler TCT.

Figure 58A indicates that the aluminum (Al) peak is decreased for the PEG-60 device #5 as compared to the TCT-functionalized device. This finding is consistent with addition of a mPEG overlayer. Moreover, the increased carbon (C) peak and decreased nitrogen (N) peak observed for the PEG-60 device (Figure 58A) relative to the TCT device (Figure 58B) is likely indicative of mPEG conjugation since mPEG contains more carbon atoms and fewer nitrogen atoms per molecule than TCT. Finally, the binding chemistry of nitrogen (N) changes upon reaction with mPEG at 60 mg/mL; in particular, the nitrogen peak shifts to a lower electron binding energy. To quantify this binding energy shift core level scans of nitrogen were taken, with pass energy of 20 eV using the same monochromated Al K α source, on both the #5 device piece reacted with 60 mg/mL mPEG in DI water (Figure 59A) and a similar #5 device coated with 300 cycles of PE-ALD deposited Al₂O₃, the silane APTES, and the coupler TCT (Figure 59B).

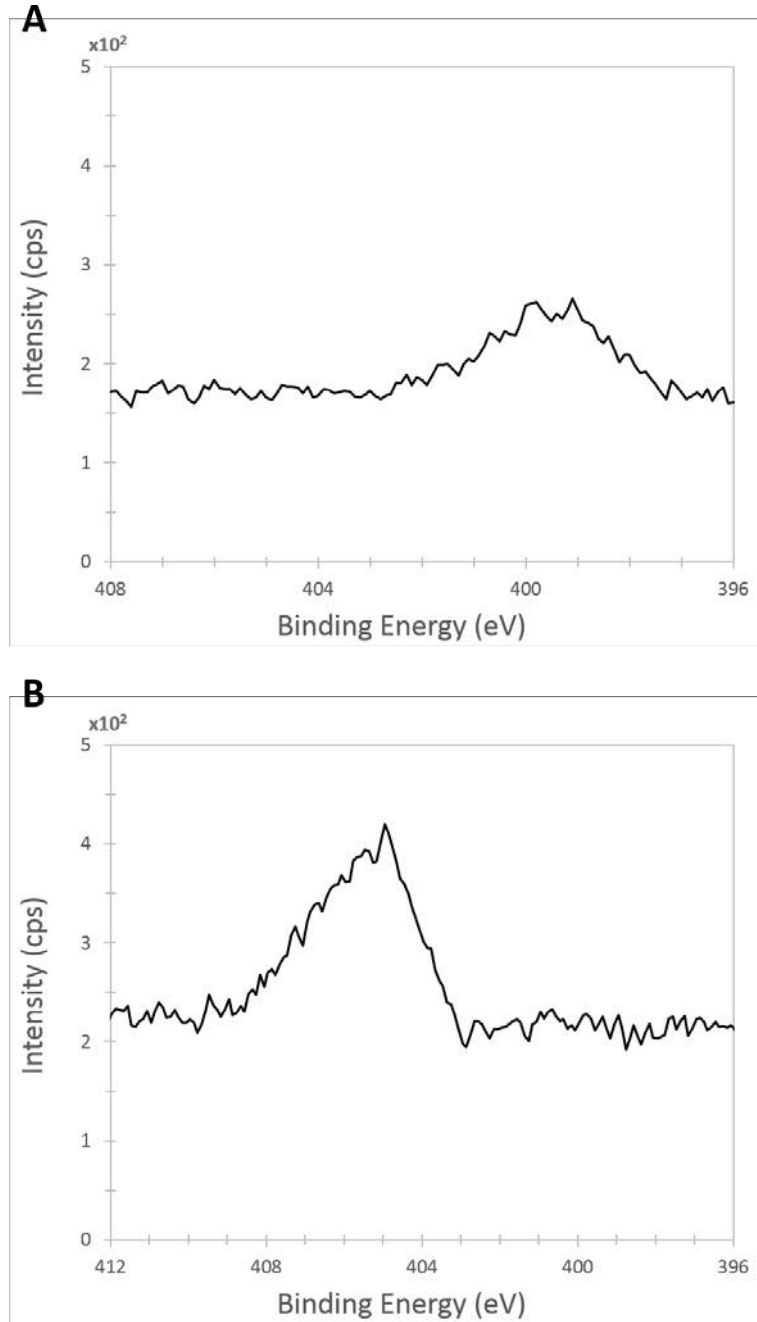


Figure 59: (A) The acquired XPS core level scan for nitrogen on a commercial flow diverting device #5 piece coated with 300 cycles PE-ALD deposited Al_2O_3 , the silane APTES, the coupler TCT, and mPEG with average molecular weight of 13000 dissolved in deionized water at 60 mg/mL. (B) The acquired XPS core level scan for nitrogen on a commercial flow diverting device #5 piece coated with 300 cycles PE-ALD deposited Al_2O_3 , the silane APTES, and the coupler TCT.

Figure 59A indicates that an electron shift to a lower binding energy is observed in the nitrogen core level peak upon incubation of a #5 flow diverting device with 60 mg/mL mPEG in DI water, relative to a TCT-functionalized #5 device (Figure 59B). This shift is

likely indicative of mPEG conjugation to the TCT layer since the oxidation state of nitrogen in mPEG is more negative (fewer imines and more amine groups). Moreover, the decreased signal intensity of the nitrogen peak observed in Figure 59A likely suggests mPEG conjugation since fewer nitrogen atoms are present in the mPEG molecule as compared to TCT; likewise, the nitrogen atoms comprising the underlying TCT layer are now more difficult to detect via XPS since they are sterically shielded by conjugated mPEG, and therefore contribute less to the overall nitrogen signal intensity.

Likewise, the mPEG-100 #5 device piece was probed by an XPS technician approximately one week post coating at the UIUC Frederick Seitz Materials Research Laboratory using a Kratos Axis Ultra XPS instrument, since the Kratos Axis Ultra instrument at the University of Iowa was broken. The XPS survey scan of the PEG-100 flow diverting device #5 piece is shown as Figure 60A; likewise, the XPS survey scan of a similar flow diverting device #5 piece functionalized with 300 cycles of PE-ALD deposited Al_2O_3 , the silane APTES, and TCT is shown as Figure 60B.

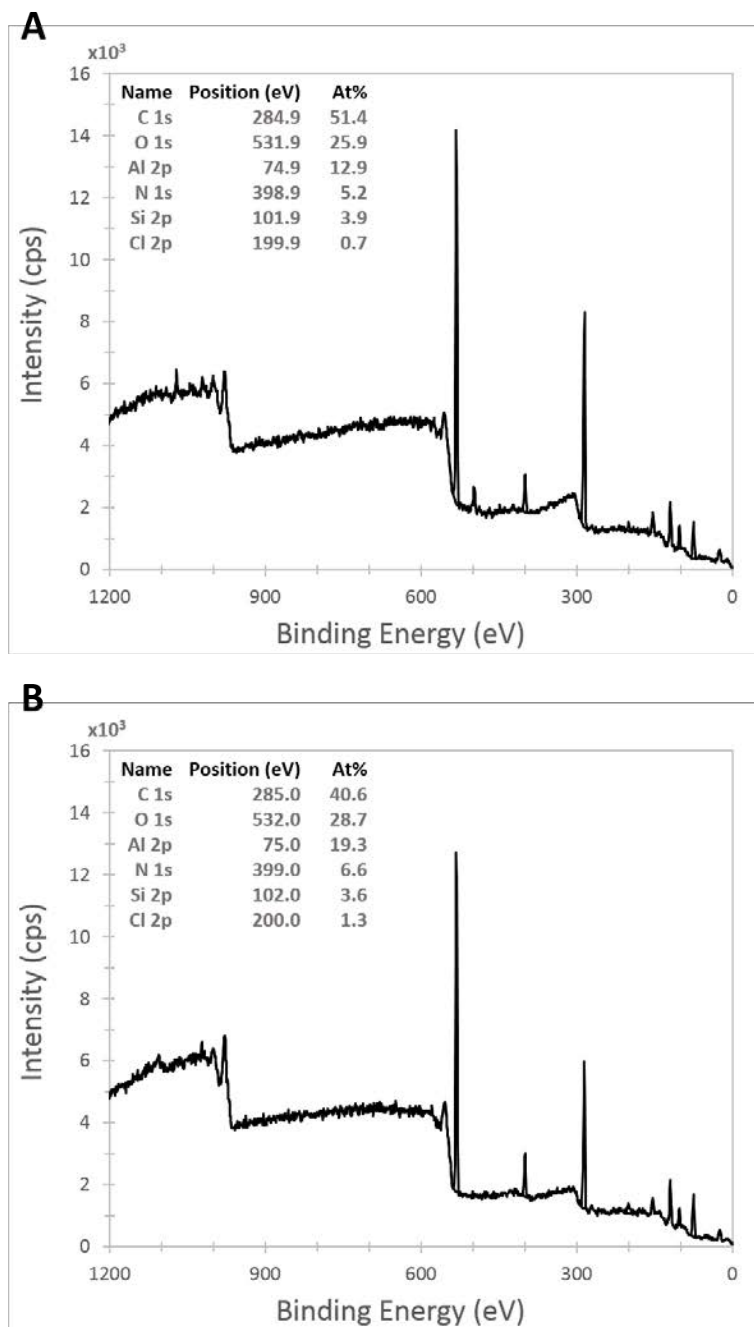


Figure 60: (A) The acquired XPS survey scan on a commercial flow diverting device #5 piece coated with 300 cycles PE-ALD deposited Al_2O_3 , the silane APTES, the coupler TCT, and mPEG with average molecular weight of 13000 dissolved in deionized water at 100 mg/mL. (B) The acquired XPS survey scan on a commercial flow diverting device #5 piece coated with 300 cycles PE-ALD deposited Al_2O_3 , the silane APTES, and the coupler TCT.

Similar to Figure 58A, Figure 60A indicates that the aluminum (Al) peak is decreased for the PEG-100 #5 device as compared to the TCT-functionalized #5 device. This finding is consistent with addition of a mPEG overlayer. Moreover, the increased carbon (C)

peak and decreased nitrogen (N) peak observed for the PEG-100 device (Figure 60A) relative to the TCT device (Figure 60B) is likely indicative of mPEG conjugation since mPEG contains more carbon atoms and fewer nitrogen atoms per molecule than TCT. Finally, the binding chemistry of nitrogen (N) changes upon reaction with mPEG at 100 mg/mL; in particular, the nitrogen peak shifts to a lower electron binding energy. To quantify this binding energy shift core level scans of nitrogen were taken, with pass energy of 20 eV using the same monochromated Al K α source, on both the #5 device piece reacted with 100 mg/mL mPEG in DI water (Figure 61A) and a similar #5 device coated with 300 cycles of PE-ALD deposited Al₂O₃, the silane APTES, and the coupler TCT (Figure 61B).

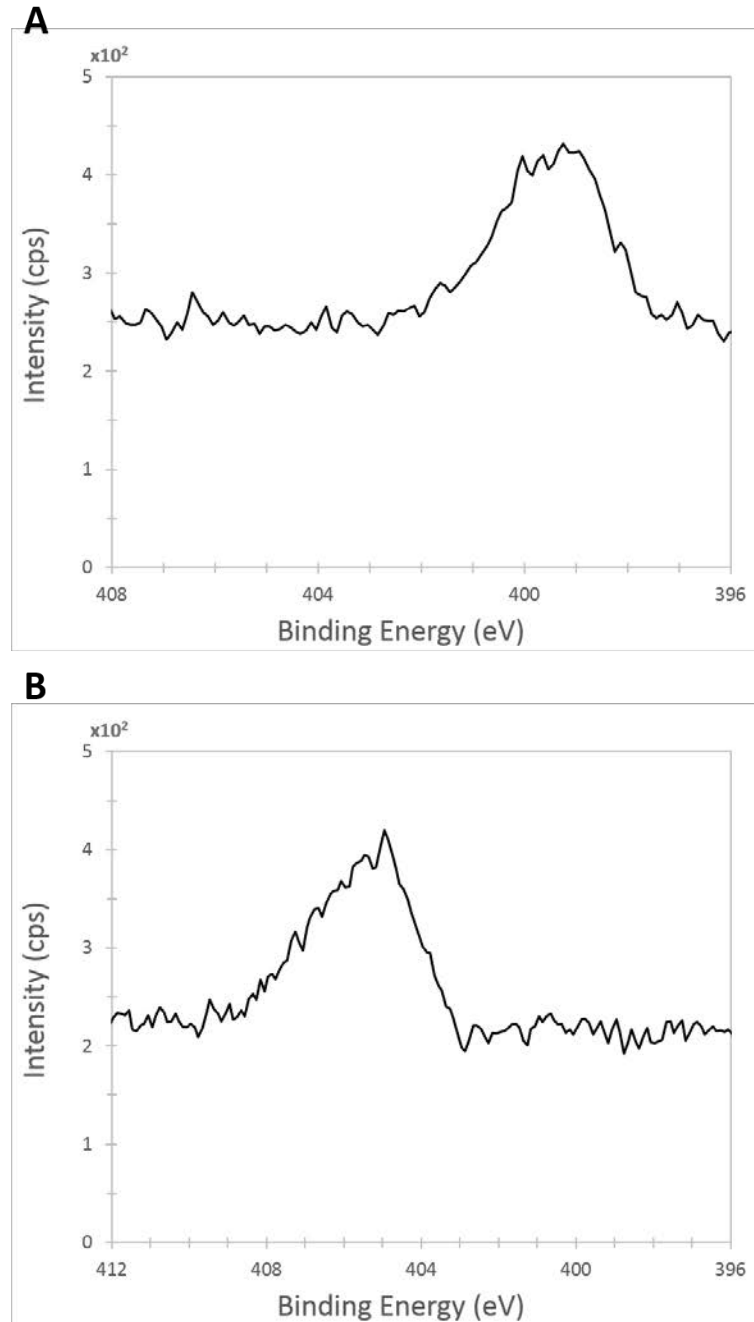


Figure 61: (A) The acquired XPS core level scan for nitrogen on a commercial flow diverting device #5 piece coated with 300 cycles PE-ALD deposited Al_2O_3 , the silane APTES, the coupler TCT, and mPEG with average molecular weight of 13000 dissolved in deionized water at 100 mg/mL. (B) The acquired XPS core level scan for nitrogen on a commercial flow diverting device #5 piece coated with 300 cycles PE-ALD deposited Al_2O_3 , the silane APTES, and the coupler TCT.

Figure 61A indicates that an electron shift to a lower binding energy is observed in the nitrogen core level peak upon incubation of a #5 device with 100 mg/mL mPEG in DI water, relative to a TCT-functionalized #5 device (Figure 61B). This shift is likely

indicative of mPEG conjugation to the TCT layer since the oxidation state of nitrogen in mPEG is more negative. A schematic of how mPEG binds to the TCT layer of the developed coating technology in DI water is shown as Figure 62.

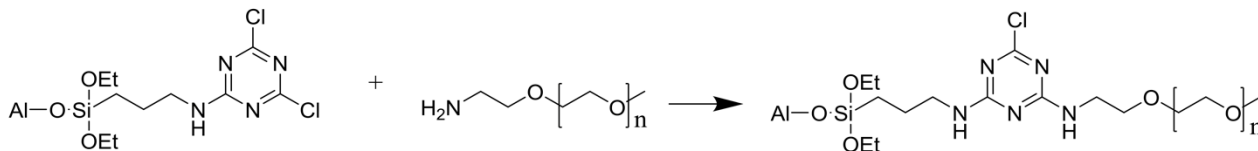


Figure 62: A schematic of how mPEG binds to the coupler TCT layer of the developed coating technology.

Note that it is also possible for mPEG to attach to the APTES layer by reaction of its free amine with an ethoxy group on the silane molecule.

Third-Party In-Vitro Thrombogenicity Assessment of the Coating Technology as a Platform for the Attachment of FDA-approved Molecules

Inclusion of the bioactive component hTM in the developed coating technology poses a problem, from a commercial perspective, since hTM is not FDA-approved; therefore, commercialization of the technology, as it stands, is more challenging. Inclusion of an FDA-approved alternative to hTM, whether bioactive or not, would lessen the amount of verification and validation testing required by the FDA for market approval and facilitate early commercialization of the technology. This type of commercialization pathway may be an attractive alternative to medical device companies looking to acquire the technology. With this in mind, the focus was to develop the coating technology as a platform for three specific FDA-approved molecules: methoxy-poly(ethylene glycol) amine (or mPEG), o-phosphorylethanolamine (o-PA) a derivative of phosphorylcholine (or PC), and heparin. These particular FDA-approved molecules were chosen because each has established a precedent in the literature as a surface modification or coating for medical devices; likewise, once surface immobilized, each has demonstrated marked improvement of device biocompatibility.^{94, 96, 101} The strategies created for incorporating each in the developed coating technology in place of hTM were discussed in the previous sections; moreover, their covalent attachment to the respective underlying coating layer was substantiated via XPS.

To test the in-vitro functionality of each developed coating chemistry platform for conjugation of mPEG, o-PA, and heparin, the Calibrated Automated Thrombogram

(CAT) Assay was used and was performed by Haematologic Technologies Incorporated (HTI), a third-party ISO 9001:2015 certified company. The preliminary study design consisted of coating pieces of a commercial flow diverting device #5 with hTM and TCT, two known chemistries, at the University of Iowa and shipping to HTI for CAT assay testing; this was done to assess the validity of the assay protocol by providing an opportunity to identify problems and explore solutions.

The CAT assay protocol that was used for testing at HTI was developed via collaboration with HTI hematologists and research scientists, the goal of which was to replicate, as close as possible, the in-house CAT assay protocol previously discussed. This developed test protocol retains use of Thrombinoscope CAT reagents; however one key difference was introduced, namely the incorporation of platelet-poor plasma (PPP) as the test plasma and a replacement for platelet-rich plasma (PRP). This change was spurred by lack of a high-fidelity human blood cell counter at HTI to measure blood platelet counts; because Thrombinoscope recommends using their PRP reagent with normalized human PRP samples, the inability of HTI to accurately measure and normalize plasma platelet counts was considered problematic. Since HTI has experience in using the CAT assay with PPP to assess the thrombogenicity of intravenous immune globulin (IVIG) therapy pharmaceuticals, incorporation of PPP into this test protocol was considered acceptable. Furthermore, since this CAT assay is measuring the outcome of thrombin generation, rather than platelet aggregation or activation, platelets in this assay serve only as a surface for coagulation reactions to occur; yet the platelet surface is imitated in the current assay (and in-house assay as well) by addition of phospholipids, since it is on the phospholipid surface that many of the coagulation reactions occur. Thus, having HTI perform the CAT assay in PPP was considered sufficient; in fact, aside from HTI performing the assay with PPP and the associated Thrombinoscope PPP reagent, all other protocol details were kept consistent with the in-house CAT assay protocol.

In this preliminary study, commercial flow diverting device #5 pieces (each with diameter of 4.7 mm and length approximately 5 mm) were coated with hTM (n=4) and TCT (n=4) and immediately shipped to HTI; lyophilized human recombinant hTM (10 µg, Sigma-Aldrich), sterile glass shards (n=4, similarly sized), and bare #5 device pieces (n=4, diameter of 4.7 mm and length approximately 5 mm) were also shipped to HTI as CAT assay controls. All device pieces and controls were received by HTI and tested in

the CAT assay three days post coating deposition. It should be noted that, immediately prior to testing, the lyophilized human recombinant hTM was reconstituted by an HTI scientist in 500 μ L 1X DPBS, following the developed protocol, and immediately included in the assay as a negative control. The resulting peak thrombin generation results are shown as Figure 63.

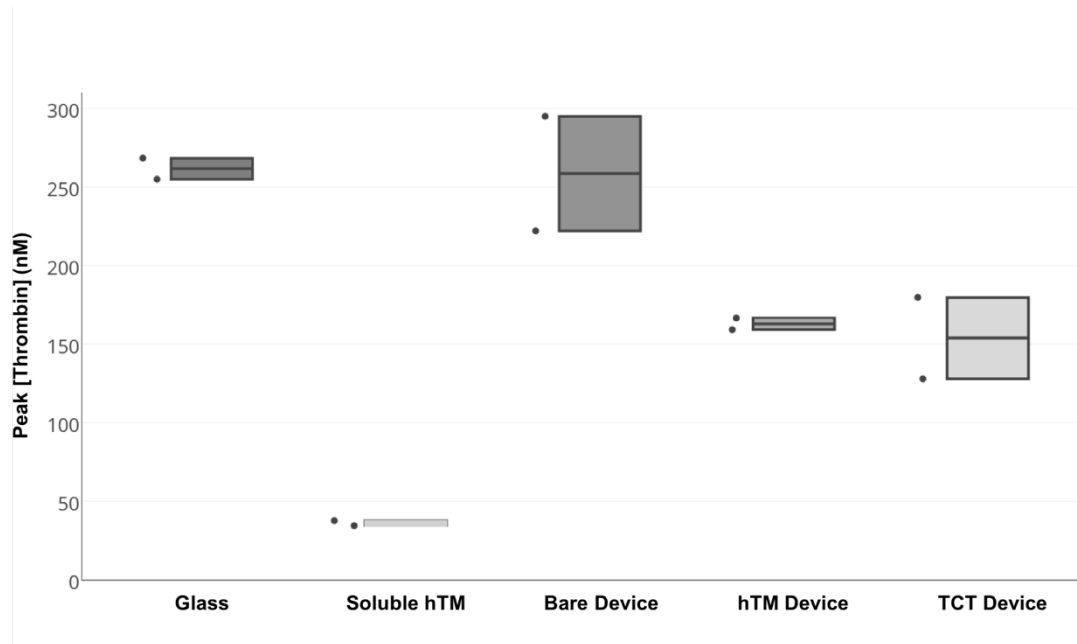


Figure 63: The peak thrombin concentration associated with the thrombogram of each sample tested in the preliminary CAT assay by Haematologic Technologies Inc. three days post coating deposition.

Note that, while four samples of each type of coated device or control were shipped to HTI for preliminary CAT assay testing, only two samples in each category were tested and are depicted in Figure 63; since it was the first time HTI had run this particular CAT assay, the remaining two samples in each category were withheld and saved in case problems were encountered. Nevertheless, these saved samples were ultimately tested by HTI one week post coating deposition; the associated peak thrombin generation results for these samples are shown as Figure 64.

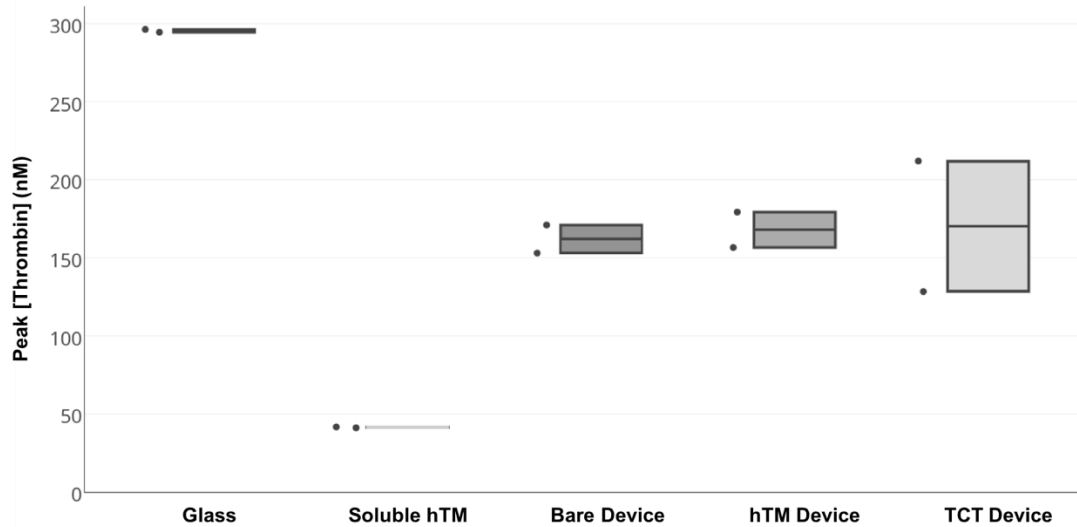


Figure 64: The peak thrombin concentration associated with the thrombogram of each sample tested in the preliminary CAT assay by Haematologic Technologies Inc. one week post coating deposition.

The most striking observation from Figures 63 and 64 is that the commercial bare flow diverting device #5 pieces exhibit large variation in the amount of thrombin they generate, similar to the commercial flow diverting device #3 pieces probed in the hTM shelf life study (Figure 38). The variability observed, regarding the amount of thrombin generated by bare #5 flow diverting pieces, is likely impacting the thrombin generating capacity of the hTM coated #5 devices. While more testing is required, these two preliminary studies indicate that the positive and negative controls of glass and soluble hTM, respectively, behave as expected under the HTI CAT assay test conditions in PPP.

Because these preliminary studies demonstrated that the positive and negative controls behaved as expected, HTI's CAT assay with PPP was next used to test the in-vitro functionality of each developed coating chemistry platform. For this test, commercial flow diverting device #5 pieces (each with diameter of 4.7 mm and length approximately 5 mm) were coated at the University of Iowa with the following chemistries: hTM (n=3), TCT (n=3), o-PA-DI water (or o-PA-DI, n=3), heparin-MES (or hep-MES, n=3), heparin-bicarbonate (or hep-bic, n=3), PEG-60 (n=3), and PEG-100 (n=3) and immediately shipped to HTI. These particular chemistries were chosen as their corresponding XPS survey and core level scans indicated it likely that each conjugated either mPEG, o-PA, or heparin to the intracranial device; therefore, these

chemistries were thought to possess the most promising functionality profiles. Likewise, lyophilized human recombinant hTM (10 µg, Sigma-Aldrich), sterile glass shards (n=3, similarly sized), bare flow diverting device #5 pieces (n=3, diameter of 4.7 mm and length approximately 5 mm) and bare flow diverting device #1 pieces (n=3, diameter of 3.5 mm and length approximately 5 mm) were also shipped to HTI as CAT assay controls. All device pieces and controls were received by HTI and tested in the CAT assay three days post coating deposition. It should be noted that, immediately prior to testing, the lyophilized human recombinant hTM was reconstituted by an HTI scientist in 500 µL 1X DPBS, following the developed protocol, and immediately included in the assay as a negative control. The resulting peak thrombin generation results are shown as Figure 65.

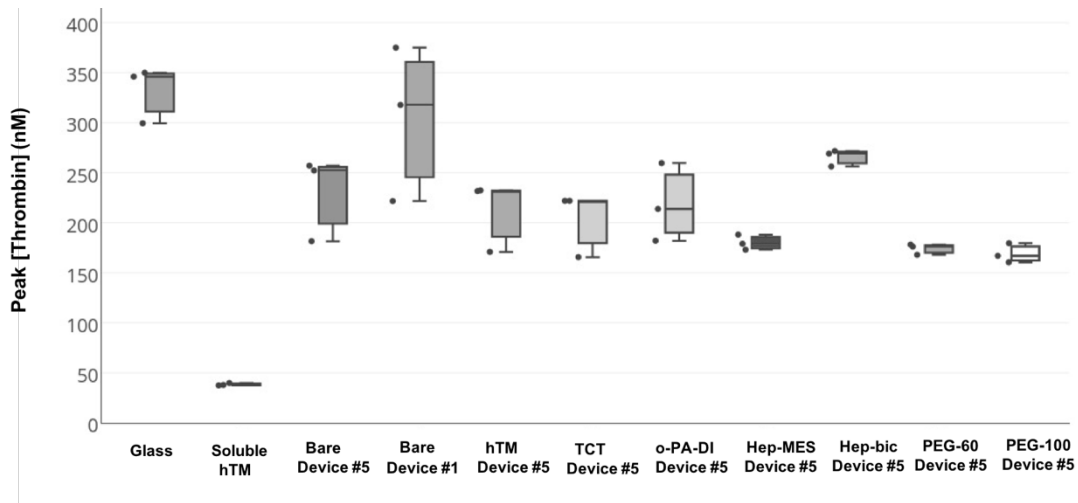


Figure 65: The peak thrombin concentration associated with the thrombogram of each developed coating chemistry platform in the CAT assay by Haematologic Technologies Inc. three days post coating deposition.

Figure 65 indicates that the hTM, TCT, and o-PA-DI coating chemistries do little to improve the thrombogenicity inherent to the bare flow diverting device #5. In contrast, the heparin-MES, PEG-60, and PEG-100 coating chemistries provide some improvement in #5 device thrombogenicity. This test also reveals that there seems to be large variability in the thrombin generating capacity of commercially available flow diverting devices #1 and #5; in fact, both inter- and intra-device related differences in thrombin generating capacity exist. Despite the small sample size in this study (n=3), which does not lend itself to statistical analyses, the observation that the Heparin-MES, PEG-60, and PEG-100 coated #5 devices have the least amount of intra-device variability in thrombin generation, and the smallest peak thrombin concentrations overall,

suggest that they are the most promising coating formulations and should be selected for further optimization and testing.

CHAPTER 5

Failed Experiments

Throughout the course of my dissertation work I attempted several types of experiments in which problems persisted and were not completely resolved. This chapter outlines these experiments and the associated shortcomings.

The Protein C Activation Assay: A Static In-Vitro Thrombogenicity Test

The bioactivity of the conjugated hTM in the developed coating technology was evaluated in-vitro via the Protein C Activation Assay. This assay measures hTM functionality indirectly; specifically, it does so by measuring the change in optical density produced by a chromogenic substrate specific to activated protein C (APC) in buffered solution – APC is generated by the thrombin-thrombomodulin complex and works with its cofactor protein S to degrade factors Va and VIIIa so that they no longer facilitate thrombin generation and factor Xa formation.^{73, 106} Once the change in optical density, triggered by APC generation, is measured it is compared to the optical density signals generated from standard amounts of soluble hTM in buffered solution. From this comparison, the amount of functional hTM immobilized to a device, for instance, can be computed.

To perform this assay, practicing hematologist and research scientist at the University of Iowa Dr. Steven Lentz was consulted and the Lentz Lab protocol for the Protein C Activation Assay was used for this test. The test design consisted of evaluating the functionality of conjugated hTM on two commercial stent-assisted coiling #6 devices (4.5 x 22 mm), as compared to a bare #6 device of the same size. First, hTM was conjugated to the #6 device surfaces via the developed coating technology protocol at the University of Iowa. Next the two hTM devices were placed in individual microfuge tubes containing 5 μ L of 200 μ g/ml cell lysate extract (20 mM Tris-HCl with pH 8.0, 100 mM NaCl, 3 mM CaCl₂, 0.6% triton X-100); the hTM devices were not cut, but rather partially submerged in the lysate solution. The bare device was also partially submerged in 5 μ L 200 μ g/ml cell lysate extract in another microfuge tube. Next, 5 μ L of the soluble hTM standards (human recombinant with the following concentrations: 0, 2.5, 5.0, 10.0, and 20 nM) were pipetted into separate microfuge tubes (prepared in triplicate); likewise,

5 μL of 200 $\mu\text{g}/\text{ml}$ cell lysate extract was added to these tubes. Following this the pre-mix, consisting of assay buffer, 325 nM human alpha-thrombin, and 1.5 μM protein C, was made and 20 μL was added to each microfuge tube. Note that the assay buffer consisted of deionized (DI) water (45.5 mL), 1 M Tris-HCl (pH = 7.4, 2.5 mL), 0.1 M CaCl_2 (1 mL), 5 M NaCl (1 mL), and Bovine Serum Albumin (BSA, 50 mg). All the samples were mixed gently by pipetting, centrifuged at 1000 rpm, and incubated in a water bath at 37°C for 30 minutes. After incubation, 2 μL of stop solution (consisting of 123 μL assay buffer, 11 μL anti-thrombin III at 6 mg/mL, and 66 μL heparin at 1000 U/mL) was added to each sample, vortexed, and centrifuged at 1000 rpm. The samples were then assayed immediately. To start, the chromogenic substrate S-2366 (20 mM, 50 μL) was brought to room temperature; afterward it was gently mixed with 4.45 mL of DI water. Following this, 5 μL of each sample or control was added to individual wells of a 96-well microplate. With a multi-pipettor, 100 μL of S-2366-DI water solution was then added to each well. The 96-well plate was then placed in a microplate reader with absorbance set at 405 nm for five minutes.

Due to difficulty experienced in exporting the raw absorbance time courses from the microplate reader, only the *absorbance rates* for the three devices and the hTM standards were recorded. These absorbance rates were then used to regenerate the raw absorbance time courses for the control and hTM coated devices; these regenerated raw absorbance time courses are shown in Figure 66.

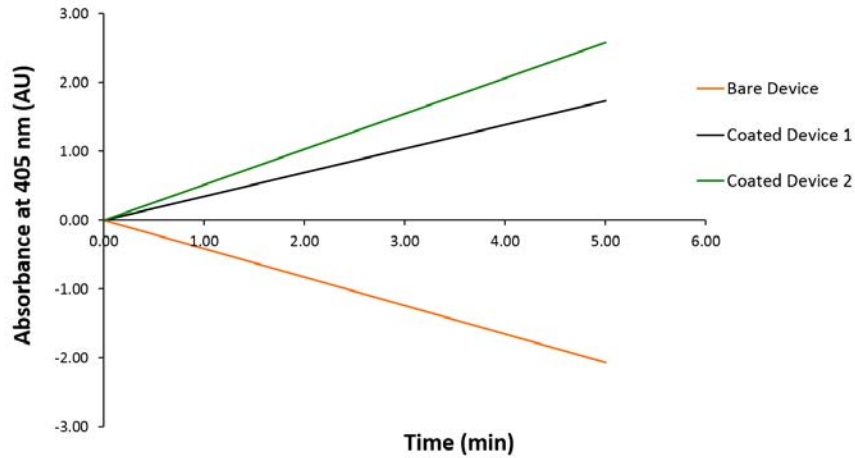


Figure 66: The regenerated absorbance versus time raw data for the bare and hTM coated commercial stent-assisted coiling #6 devices tested in the Activated Protein C assay. The raw data was regenerated using the recorded absorbance rates over the measurement time period, due to difficulty experienced in exporting the raw data from the microplate reader.

The hTM standard curve was then generated by plotting the absorbance rates of each hTM standard against their respective hTM concentrations; a linear trend-line was passed through this curve and its equation was used to linearly interpolate the measured absorbance rates of the bare and hTM coated devices onto the standard curve. In this way the amount of active hTM conjugated to the coated devices was determined. This standard curve is shown as Figure 67.

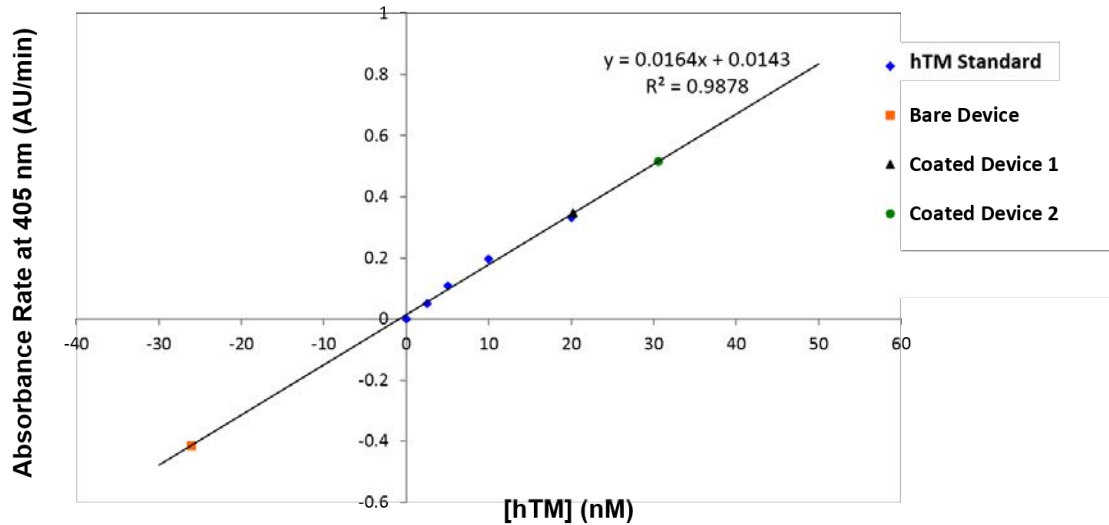


Figure 67: The hTM standard curve associate with the Activated Protein C assay. The measured absorbance rates for the bare and hTM coated commercial stent-assisted coiling #6 devices were linearly interpolated on this curve to determine the amount of active hTM conjugated to the coated devices.

The negative absorbance rate associated with the bare stent-assisted coiling #6 device, shown in Figures 66 and 67, was a surprising result. Sean Gu, an M.D. and Ph.D. student in the Lentz Lab who helped with the assay protocol and data analysis, also ran his own samples of digested mouse heart tissue in this Activation Protein C assay. He found that the mouse heart tissue exhibited negative absorbance over time across the triplicate wells. While the precise mechanism is unknown, it is believed that metal ions, characteristic of both the bare #6 device and the mouse heart tissue, act to attenuate the function of the chromogenic substrate S-2366 and therefore produce negative absorbance over time. Additionally, differences in the measured absorbance rates were found to exist between the two hTM coated devices, as shown in Figure 66. A potential explanation for this difference is that the devices were submerged to a different extent in the buffer solution, causing different amounts of protein C activation and ultimately absorbance rates. Since this was the first time the assay had been done with solid devices, the degree of device submersion in the buffer was not considered initially to be a source of error. Nevertheless, from the linearly interpolated hTM concentrations of the hTM coated devices onto the standard curve (Figure 67) it is estimated that between 20.2-30.5 nM of the conjugated hTM is functional. Furthermore, it is surmised that this functional hTM is bound to approximately 5 mm of a #6 device, which is an estimate of the average device submersion in the buffer solution during the assay.

Ultimately because the control, or bare, #6 device attenuated the function of the chromogenic substrate used in this Activated Protein C assay it is unclear what to make of the results, though a plausible explanation of the attenuation is postulated. Thus, this assay should be repeated with other types of metallic and non-metallic controls, as well as more careful consideration for the length of device submerged in the assay buffer solution.

The Modified Chandler Loop: A Dynamic In-Vitro Thrombogenicity Test

The Modified Chandler Loop was originally described in 2002 by Tepe et al.¹⁰⁷ as an in-vitro model to evaluate the thrombogenicity of peripheral vascular stents. The model design is shown in Figure 68.

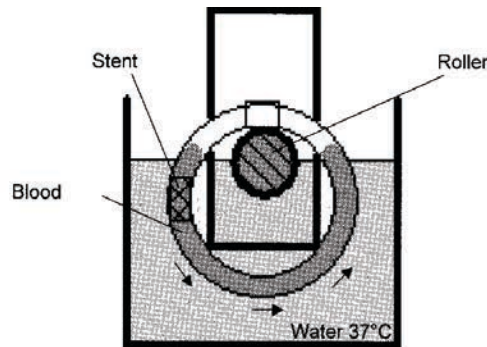


Figure 68: The Modified Chandler Loop as described by Tepe et al.¹⁰⁷

As evidenced by Figure 68, the Modified Chandler Loop is a single tubing loop in which a vascular stent is deployed, partially filled with blood, and closed. This closed loop is then rotated via a roller through a warm water bath to passively circulate the blood throughout. Unlike the original model design proposed by Chandler in 1958, which used an internal motor to pump blood through the closed loop¹⁰⁸, the modified design uses only the rotation of the loop to circulate the blood within.¹⁰⁷ Using rotation to passively circulate blood helps mitigate the traumatizing effects of pushing blood through a pump, which likely activates platelets to such a degree that the additional platelet activation caused by exposure to the deployed device surface would be difficult to measure.¹⁰⁷

Thus, the Modified Chandler Loop is an in-vitro closed circuit model that can dynamically move blood through any tubular vascular device deployed within and possesses relatively low inherent platelet activation; in this way the Modified Chandler Loop more closely mimics physiologic blood flow through vascular devices and is

therefore unlike any other in-vitro test model. As a result, the Modified Chandler loop was thought to be a good model to test the thrombogenicity of the developed coating technology in a dynamic blood flow environment with the merit of having control over blood flow parameters like velocity and shear stress, control not possessed in in-vivo models. With this aim, a Modified Chandler Loop was built in-house to dynamically test the thrombogenicity of the developed coating technology.

Since the Modified Chandler Loop needs to be steadily rotated to circulate the blood within, a multifunctional wheel to hold a Chandler tubing loop, close it, and connect it to a motor shaft was designed in PTC Creo® and is shown as Figure 69.



Figure 69: A multifunctional wheel designed in PTC Creo® to hold a Modified Chandler Loop, close it, and connect it to a motor shaft. The interior hole is designed to fit the motor shaft, while the flange on top provides both radial and longitudinal compression to close the tubing ends.

As shown in Figure 69, a groove along the circumference of the wheel holds the tubing in place. The flange on top of the wheel provides both radial and longitudinal compression to close the tubing ends, which is tightened manually via screws and nuts. Each wheel accommodates 50 cm of tubing with 1/8 inch inner diameter and outer diameter of 1/4 inch. The interior hole is designed to fit a motor shaft, allowing for loop rotation at 15 rpm and a blood flow velocity within of 12.5 cm/s, which is specified by Tepe et al.¹⁰⁷ Several of these wheels were 3D-printed in ABS plastic and were used for experimentation. A photo of the entire Modified Chandler Loop in-house set-up is shown as Figure 70.

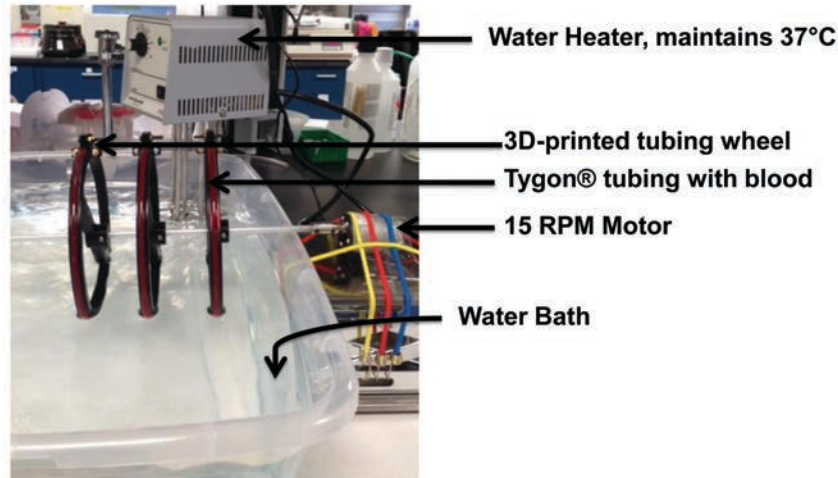


Figure 70: Photo of the Modified Chandler Loop built in-house at the University of Iowa.

The experimental protocol for evaluating dynamic intracranial device thrombogenicity in a Modified Chandler Loop at the University of Iowa is as follows: first human whole blood was collected from a healthy volunteer following standard hospital procedure into tri-sodium citrate vacutainer tubes (containing 3.2% tri-sodium citrate at 0.109 M); this whole blood sample was stored under a sterile cell culture hood at room temperature. Next the heater immersed in the Modified Chandler Loop water bath was started so that the water could equilibrate to 37°C. Subsequently the intracranial devices of interest (in these studies, all were commercial flow diverting #1 devices with diameters between 2.75 – 3.00 mm and lengths between 10 – 14 mm) were pushed into individual, autoclaved Tygon® tubing loops via the associated sterile device guide wire under a sterile cell culture hood. In all these studies the intracranial devices of interest were either bare, hTM, or hTM+APC (10 µg hTM + 0.25 mg APC in 500 µL 1X DPBS Buffer) #1 devices coated following the developed protocol at the University of Iowa; in some cases, #1 devices spray-coated with hTM+APC (10 µg hTM + 0.25 mg APC) in PLGA at the University of Iowa were also tested. Likewise, several tests included similarly sized glass (3 x 10 mm) and linear low-density polyethylene (LLDPE, 3.2 x 10 mm) tubes, which were pushed by the sterile device guidewires into individual Tygon® tubing loops and tested as controls. Following this, the tubing loops containing either the deployed devices or the control glass or LLDPE tubes were then attached to individual 3D-printed tubing wheels and ultimately fastened to the same motor shaft.

To negate the effect of the sodium citrate anticoagulant on the whole blood sample, a 25 mM solution of CaCl₂ was made and 86.4 µL was added to every 2.7 mL of

blood; this resulted in an approximately physiological level of Ca^{2+} in the blood. Next, a 16.5 G syringe was used to dispense 3 mL of the re-calcified blood into each tubing loop; the loops were subsequently closed via the tubing wheel flanges. Any excess blood, referred to as “pre-blood” in these studies, was kept in its sodium-citrate vacutainer and placed in an insulated cell culture shaker at 37 °C. Next the motor shaft with attached tubing wheels was fastened to a 15 rpm motor and run for six hours, as shown in Figure 67, rotating the individual Chandler loops. Afterward the blood from each wheel was separately collected into K_2EDTA vacutainers under a sterile hood; the pre-blood was also poured into a K_2EDTA vacutainer. All of the collected blood samples were then run through the Sysmex XE-2100 CBC analyzer in the University of Iowa Medical Labs to measure individual platelet counts, which were recorded. Finally, under a sterile hood the devices and control tubes were pushed out of their associated tubing loops with a guide wire and imaged via light microscopy.

A total of five separate Modified Chandler Loop studies were run at the University of Iowa which tested the thrombogenicity of coated and bare commercial flow diverting #1 devices, as well as the thrombogenicity of similarly sized glass and LLDPE tubes, in dynamic blood flow environments. However inconsistent platelet counts measured among coated devices and controls (consisting of glass and LLDPE tubes, bare #1 devices, and pre-blood) plagued these tests; additionally, the Chandler loops containing the glass and LLDPE tubes were always patent at the end of testing. Because the controls never properly thrombosed, and because the platelet counts of all samples were inconsistent between tests, the Modified Chandler Loop was abandoned as a dynamic in-vitro thrombogenicity test model for the developed coating technology. Similar inconsistencies with the Modified Chandler Loop in-vitro model were corroborated by the medical device company Medtronic Inc.

Static In-Vitro Platelet Adhesion: A Method for Qualitative Assessment

The blood platelet is an important cell in the coagulation process. When the vascular endothelium is damaged platelets adhere to the exposed collagen, microfibrils, and basement membrane underneath.¹⁰⁹ Once adhered, platelets release the contents of their alpha granules, which act as mediators to promote a number of hemostatic mechanisms and functions like vasoconstriction or recruitment of more platelets; these processes involve a macroscopic platelet shape change from discoid to a spheroid,

spiny formation.¹⁰⁹ Platelet aggregation continues and is mediated by the local concentration of released granular contents, particularly of adenosine diphosphate (ADP); if ADP concentration does not reach a high local concentration the platelet aggregation may be reversible, otherwise aggregation is irreversible and a platelet plug is formed.¹⁰⁹ Changes in the platelet's surface architecture during this process expose surface phospholipids, which act as receptors for coagulation proteins to promote or else accelerate thrombin formation.¹⁰⁹ The ensuing coagulation cascade, or the series of enzymatic reactions involving plasma, proteins, phospholipids, and calcium ions, then serves to finalize the process initiated by the platelet.¹⁰⁹ Because of the singular importance of platelets in coagulation, and ultimately thrombin generation, the extent of platelet aggregation on implanted medical devices could be used as a metric of device thrombogenicity. Thus, in this set of experiments platelets were separated from human whole blood, seeded, and incubated on both coated and control silicon wafer and flow diverting device surfaces; the extent of platelet aggregation was qualitatively evaluated on these surfaces by scanning electron microscopy (or SEM) imaging.

The platelet separation, seeding, and incubation protocol used in these experiments was adapted from that published by Okpalugo et al. in 2004.¹¹⁰ In brief, platelet separation was achieved in the initial experiment by purchasing one unit of human whole blood, collected from a healthy donor into sodium citrate, from ZenBio Incorporated; this human blood unit arrived at the University of Iowa one day post collection, was stored at 2°C overnight, and the respective platelet incubation experiment was run on day two post collection. At the time of the experiment a portion of the whole blood sample was centrifuged in a swinging bucket centrifuge to separate out the platelet-rich plasma (PRP) for later seeding and incubation – ultimately the platelet count of this PRP was adjusted to approximately 1.0×10^8 platelets/mL using a Sysmex XE-2100 CBC analyzer and platelet-poor plasma (PPP), since this particular platelet count was published by Okpalugo et al.¹¹⁰ To achieve platelet separation, approximately 30 mL of the human whole blood was centrifuged at 20°C for the following relative centrifugal forces (g): 200g for 10 minutes, followed by 230g for 10 minutes, followed by 250g for 10 minutes, after which the supernatant was collected with care to not disrupt the buffy coat. Next this supernatant was centrifuged at 20°C and 280g for 10 minutes, and again at the same temperature and 150g for 10 minutes, after which the associated supernatant was carefully collected; next, the collected supernatant was again centrifuged at 20°C and 170g for 10 minutes – the resulting buffy

coat was discarded, leaving the PRP sample. The platelet count of this PRP sample was measured using the Sysmex XE-2100 CBC analyzer in the University of Iowa Medical Labs and was found to be approximately 1.03×10^8 platelets/mL; as a result, no further dilution by PPP was required. The samples tested in this experiment were 1 cm x 1 cm p-doped silicon wafers coated with the following formulations: TCT, hTM (incubated in a solution of 10 μ L hTM in 1000 μ L 1X DPBS), PEG-10, heparin-bicarbonate, and heparin-MES. A 1 cm x 1 cm glass square and a 1 cm x 1 cm bare p-doped silicon wafer were included in the test as positive controls; to give some insight into the how stable these coatings formulations are over time, similarly sized PEG-10, heparin-bicarbonate, and heparin-MES wafers that had been stored under nitrogen gas for approximately three weeks were also included in the test. Under a sterile cell culture hood these 10 1 cm x 1 cm samples were placed into individual wells of a 24-well microplate. Following this 1 mL of the PRP sample (possessing approximately 1.03×10^8 platelets) was pipetted on top of each sample; the microplate was then covered and placed in a cell culture incubator at 37°C under 5% CO₂ and 95% air for one hour. Following the incubation period, each wafer was washed twice with 1X DPBS buffer in the sterile hood and allowed to air dry therein for 10 minutes. Subsequently the platelets attached to each wafer sample were fixed for SEM imaging by immersion in 4% paraformaldehyde solution for one hour, followed by immersion in 1% osmium tetroxide in 0.1 M phosphate solution for 30 minutes; each sample was dried by immersion in successively increased concentrations of ethanol (four minutes each) and finally hexamethyldisilazane (HMDS, 20 minutes). Afterward each sample was mounted on an aluminum SEM stub with silver paint and allowed to dry overnight.

The Hitachi S-4800 SEM instrument in the University of Iowa Central Microscopy Research Facility (CMRF) was used to qualitatively assess the extent of platelet aggregation on the wafer and glass surfaces. Just prior to imaging, each sample was coated with a thin conducting film of gold-palladium using the Emitech K550 Sputter Coater (Emitech Ltd, UK) in the CMRF – this was done to reduce SEM surface charging effects, allowing for better image contrast during SEM image acquisition. The samples were then loaded into the SEM; the instrument's electron detector was set to detect a mixture of backscattered and secondary electrons using an accelerating electron beam voltage of 1.8 kV for image acquisition. Subsequently each sample surface was probed with the SEM beam. However, no intact platelets were observed on any of the surfaces; rather, only remnant remains of fragmented platelets were detected. An acquired SEM

image depicting these fragmented platelets is shown as Figure 71; in particular, it was taken on the bare silicon wafer at magnification 30.0k but is a characteristic image of the platelet fragments observed on every sample tested in this experiment.

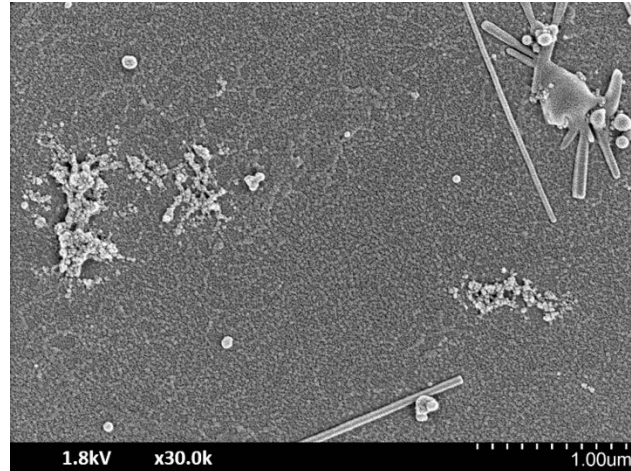


Figure 71: Platelet fragments observed by SEM on a bare, p-doped silicon wafer sample incubated for one hour in static human blood plasma containing approximately 1.03×10^8 platelets. No intact platelets were observed on this wafer sample, nor were they observed on any of the other coated or glass wafers tested in this platelet incubation experiment.

The characteristic image shown in Figure 71 indicates that platelets had attached to the control and modified wafer surfaces tested, but their attachment was disrupted prior to SEM imaging. Since this experiment was the first of its kind that I had attempted, I concluded that the once attached platelets were likely sheared from their respective wafer surfaces during either the PBS washing step or the SEM platelet fixation step when the associated fluid streams contacted the wafer surfaces. As such, I sought to repeat the experiment by keeping the washing and fixation fluids from directly contacting the sample surfaces; this was achieved by dispensing the associated fluids adjacent to each microplate well wall. In addition, the adhered platelets were immediately fixed in this experiment without allowing the samples to air dry in-between.

In the second platelet incubation experiment the extent of platelet aggregation on two bare p-doped silicon wafers was tested; particularly, the two bare wafer samples were incubated with platelets for a longer duration, washed carefully, and any adhered platelets were immediately fixed. To decrease costs one unit of human whole blood from a healthy donor (into sodium citrate), previously purchased from ZenBio Incorporated and stored at 2°C for eight days post collection, was used as the platelet sample. To achieve platelet separation approximately 20 mL of the human whole blood

was centrifuged at 20°C for the following relative centrifugal forces (g): 200g for 20 minutes, followed by 230g for 10 minutes, followed by 250g for 10 minutes, following which the supernatant was carefully collected and separated into two plastic tubes containing 4.5 mL each. These two plasma samples were again spun at 20°C and 150g for 10 minutes – the resulting buffy coat was then discarded, leaving the PRP sample. The platelet count of this PRP sample was measured using the Sysmex XE-2100 CBC analyzer in the University of Iowa Medical Labs and was found to be approximately 0.47×10^8 platelets/mL; as a result, no further dilution by PPP was required. Because this platelet count was lower than the count used by Okpalugo et al.¹¹⁰, another 30 mL whole blood sample from the same unit was spun down to PRP; however the resulting platelet count was approximately equivalent to 0.47×10^8 platelets/mL. As a result, the decreased platelet count in these PRP samples was attributed to the combined effects of whole blood storage time, temperature, and anticoagulant use rather than over centrifugation; investigators have noted that platelet aggregability in whole blood changes as time elapses after venipuncture.¹¹¹ After the PRP sample was prepared, two bare 1 cm x 1 cm p-doped silicon samples were placed into individual plastic petri dishes under a sterile cell culture hood. Following this 100 μ L of the PRP sample (possessing approximately 4.7×10^6 platelets) was pipetted directly on top of each sample; each petri dish was then covered and placed in a cell culture incubator at 37°C under 5% CO₂ and 95% air for 2.5 hours. Following the incubation period, each wafer was carefully washed, by keeping the fluid stream adjacent to the dish wall, once with 1X DPBS buffer in the sterile hood. Immediately afterward the platelets attached to each wafer sample were fixed for SEM imaging by immersion in 4% paraformaldehyde solution for one hour, followed by immersion in 1% osmium tetroxide in 0.1 M phosphate solution for 30 minutes; each sample was dried by immersion in successively increased concentrations of ethanol (four minutes each) and finally hexamethyldisilazane (HMDS, 20 minutes). Afterward each sample was mounted on an aluminum SEM stub with silver paint and allowed to dry overnight.

Like the initial platelet incubation experiment, the Hitachi S-4800 SEM instrument in the University of Iowa CMRF was used to qualitatively assess the extent of platelet aggregation in this second experiment on the two bare wafer surfaces. Just prior to imaging, each wafer was coated with a thin conducting film of gold-palladium using the Emitech K550 Sputter Coater in the CMRF. The samples were then loaded into the SEM; the instrument's electron detector was set to detect a mixture of backscattered and

secondary electrons using an accelerating electron beam voltage of 1.8 kV for image acquisition. Subsequently each wafer surface was probed with the SEM beam. This time, intact platelets were observed on both surfaces. Characteristic SEM images of each wafer surface, both taken at magnification 5.0k, are shown as Figure 72.

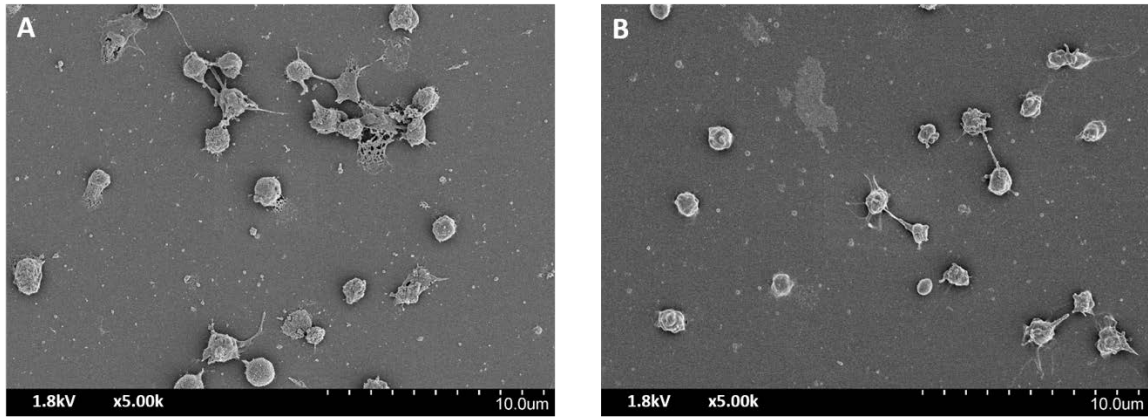


Figure 72: (A) SEM image of adhered platelets, observed on a bare, p-doped silicon wafer sample incubated for 2.5 hours in 100 μL of static human blood plasma containing approximately 4.7×10^6 platelets. (B) SEM image of adhered platelets observed on a second bare, p-doped silicon wafer also incubated for 2.5 hours in 100 μL of static human blood plasma containing approximately 4.7×10^6 platelets.

Figures 72A and 72B indicate that incubating human platelets directly on a wafer surface for a 2.5 hour duration followed by careful washing and immediate cell fixation results in reliable platelet adhesion to the associated surface.

To continue to explore the effects of human plasma platelet concentration, incubation volume, and incubation duration on static platelet surface adhesion and aggregation, a third platelet incubation experiment was run. This time four bare wafer samples were incubated in two different plasma platelet concentrations and volumes, and for two different incubation durations; specifically, one bare wafer was incubated in 100 μL PRP possessing approximately 54×10^3 platelets/ μL for three hours, the second bare wafer was incubated in 1 mL PRP possessing approximately 54×10^3 platelets/ μL for three hours, and the remaining two bare wafers were each incubated in 100 μL PRP possessing approximately 22×10^3 platelets/ μL for two hours. In this experiment human PRP, collected from a healthy donor into sodium citrate, was purchased directly from ZenBio Incorporated (~200 mL); this PRP unit arrived at the University of Iowa one day post collection and the platelet incubation experiment was run on the same day. Immediately upon arrival the PRP was mixed gently under a sterile cell culture hood and the associated platelet count was measured via the Sysmex XE-2100 CBC analyzer in

the University of Iowa Medical Labs; it was found to be approximately 0.54×10^8 platelets/mL. A portion of this PRP was then diluted to approximately 0.22×10^8 platelets/mL by addition of PPP, which was made by centrifuging a sample of the PRP at 20°C and 2000g for 10 minutes. After the two PRP samples were prepared, two bare 1 cm x 1 cm p-doped silicon samples were placed into individual wells of a 24-well microplate under a sterile cell culture hood. Following this 100 μ L of the more concentrated PRP sample (possessing approximately 5.4×10^6 platelets total) was pipetted directly on top of the first wafer sample; likewise, 1 mL of the more concentrated PRP sample (possessing approximately 0.54×10^8 platelets total) was pipetted on top of the second wafer sample. The microplate was covered and placed in a cell culture incubator at 37°C under 5% CO₂ and 95% air for three hours. One hour into this incubation, 100 μ L of the more dilute PRP sample (possessing approximately 2.2×10^6 platelets total) was pipetted directly on top of the remaining two bare wafer samples, which had been placed in individual wells of a second 24-well microplate under a sterile hood. This second microplate was covered and placed in the cell culture incubator at 37°C under 5% CO₂ and 95% air for two hours, so that the end of both incubation periods coincided. Following incubation, each wafer was carefully washed, by keeping the fluid stream adjacent to the well wall, once with 1X DPBS buffer in the sterile hood. Immediately afterward the platelets attached to each were fixed for SEM imaging by immersion in 4% paraformaldehyde solution for one hour, followed by immersion in 1% osmium tetroxide in 0.1 M phosphate solution for 30 minutes; each sample was dried by immersion in successively increased concentrations of ethanol (four minutes each) and finally hexamethyldisilazane (HMDS, 20 minutes). Afterward each sample was mounted on an aluminum SEM stub with silver paint and allowed to dry overnight.

Like the initial two platelet incubation experiments, the Hitachi S-4800 SEM instrument in the University of Iowa CMRF was used to qualitatively assess the extent of platelet aggregation in this third experiment. Just prior to imaging, each wafer was coated with a thin conducting film of gold-palladium using the Emitech K550 Sputter Coater in the CMRF. The samples were then loaded into the SEM; the instrument's electron detector was set to detect a mixture of backscattered and secondary electrons using an accelerating electron beam voltage of 1.8 kV for image acquisition. Subsequently each wafer surface was probed with the SEM beam and intact platelets were observed on all four surfaces. Characteristic SEM images of the wafer surfaces, taken at magnification 3.0k, are shown as Figure 73.

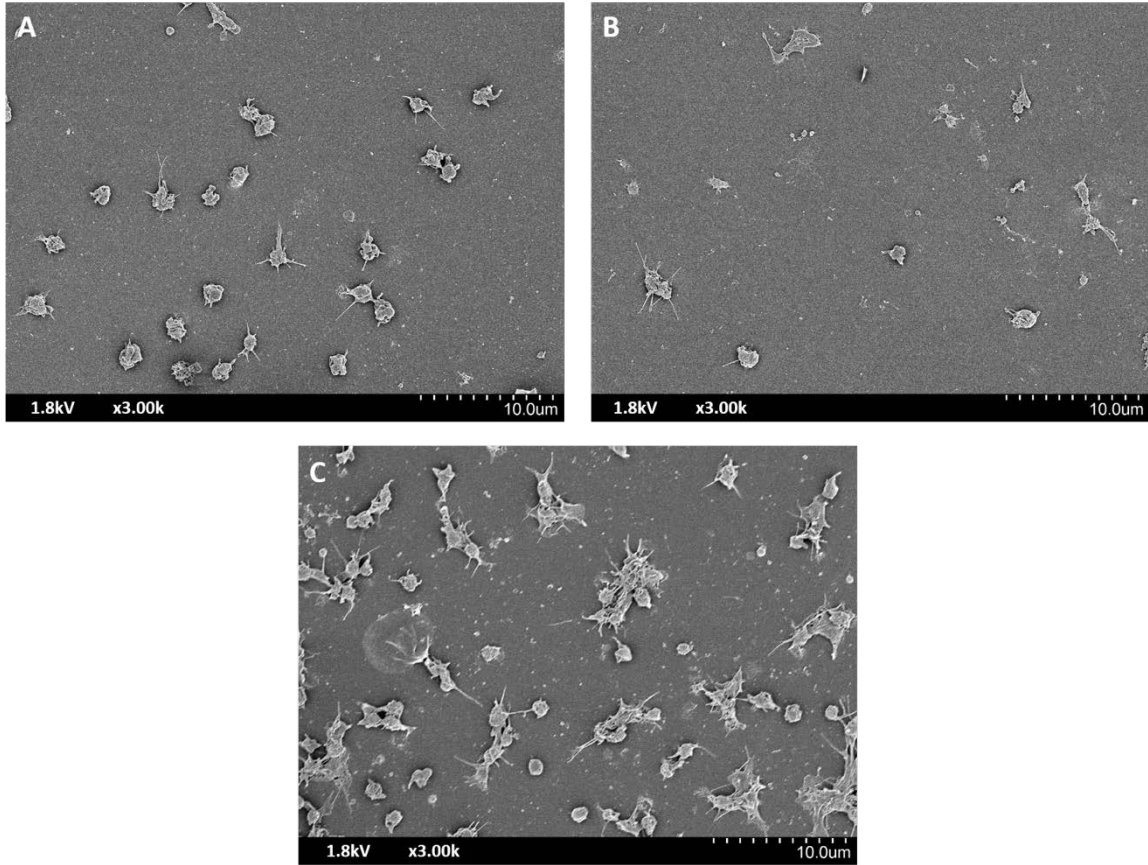


Figure 73: (A) SEM image of adhered platelets, observed on a bare, p-doped silicon wafer sample incubated for 3 hours in 100 μ L of static human blood plasma containing approximately 5.4×10^6 platelets. (B) SEM image of adhered platelets, observed on a bare, p-doped silicon wafer sample incubated for 3 hours in 1 mL of static human blood plasma containing approximately 0.54×10^8 platelets. (C) SEM image of adhered platelets, characteristic of those observed on bare, p-doped silicon wafers incubated for 2 hours in 100 μ L of static human blood plasma containing approximately 2.2×10^6 platelets.

Figure 73A indicates that decreasing the plasma incubation volume is advantageous to promote platelet surface adhesion and aggregation on p-doped silicon wafers, since fewer attached platelets were observed on a similar wafer incubated in human plasma containing the same platelet concentration (0.54×10^8 platelets/mL) but 10X the plasma volume (Figure 73B). This observation could be explained by the idea that platelets are more likely to remain buoyant in a larger plasma volume than if a smaller plasma volume is pipetted as a thin film directly on the surface of interest. Figure 73C, as a SEM image characteristic of p-doped silicon wafers incubated for two hours in 100 μ L of PRP containing 0.22×10^8 platelets/mL, indicates that the amount of platelet adhesion to a wafer surface can be optimized by changing the platelet concentration of the incubating plasma; in this experiment, the amount of platelet adhesion and aggregation to the wafer surface increased when the incubating plasma's platelet concentration decreased, given

both were incubated in the same small plasma volume (100 μ L) and despite a shortened incubation duration. This observation could be explained by the idea that platelets are more likely to interact with each other while buoyant when their concentration is increased. Thus, Figures 73A, 73B, and 73C indicate that incubating a surface of interest in a small plasma volume and low platelet concentration will minimize platelet-platelet interactions due to buoyancy effects and promote platelet surface adhesion and aggregation.

The latter finding was used to guide a final platelet incubation experiment on a commercially available bare flow diverting device #1 piece; specifically, a bare #1 device piece approximately 4.75 x 4 mm in size was incubated in 140 μ L of PRP possessing approximately 0.28×10^8 platelets/mL. This particular plasma incubation volume and platelet concentration were chosen since each were close to the respective incubation volume (100 μ L) and platelet concentration (0.22×10^8 platelets/mL) that best promoted platelet surface adhesion and aggregation on the p-doped silicon wafer. To decrease costs one unit of human PRP from a healthy donor (into sodium citrate), previously purchased from ZenBio Incorporated and stored at 2°C for eight days post collection, was used as the platelet sample. The associated platelet count of this PRP sample was measured via the Sysmex XE-2100 CBC analyzer in the University of Iowa Medical Labs and was found to be approximately 0.28×10^8 platelets/mL. In a sterile cell culture hood the flow diverting device #1 piece was placed into a single well of a 96-well microplate and 140 μ L of PRP (possessing approximately 3.9×10^6 platelets total) was pipetted on top. The microplate was covered and placed in a cell culture incubator at 37°C under 5% CO₂ and 95% air for three hours. Following this incubation the device was carefully washed, by keeping the fluid stream adjacent to the well wall, once with 1X DPBS buffer in the sterile hood. Immediately afterward the platelets attached were fixed for SEM imaging by immersion in 4% paraformaldehyde solution for one hour, followed by immersion in 1% osmium tetroxide in 0.1 M phosphate solution for 30 minutes; the device was subsequently dried by immersion in successively increased concentrations of ethanol (four minutes each) and finally hexamethyldisilazane (HMDS, 20 minutes). Afterward the device was mounted on an aluminum SEM stub with silver paint and allowed to dry overnight.

Like the previous three platelet incubation experiments, the Hitachi S-4800 SEM instrument in the University of Iowa CMRF was used to qualitatively assess the extent of

platelet aggregation on this #1 device. Just prior to imaging, the device was coated with a thin conducting film of gold-palladium using the Emitech K550 Sputter Coater in the CMRF. The sample was then loaded into the SEM; the instrument's electron detector was set to detect a mixture of backscattered and secondary electrons using an accelerating electron beam voltage of 1.8 kV for image acquisition. Subsequently the device surface was probed with the SEM beam. However, neither intact platelets nor platelet fragments were observed on any of the device wires. A SEM image representative of the observed wire surface, and taken at magnification 3.0k, is shown as Figure 74.

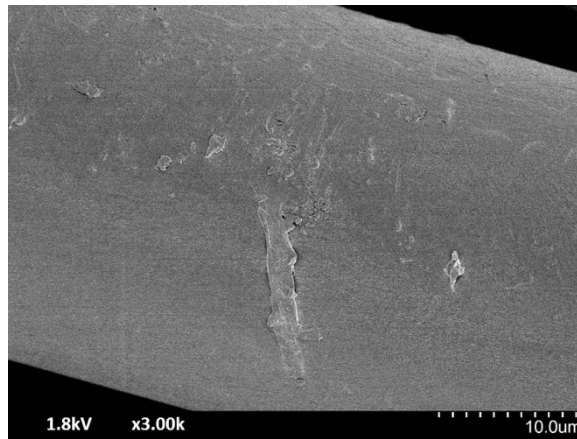


Figure 74: Representative SEM image of a bare commercial flow diverting device #1 wire. A device piece approximately 4.75 x 4 mm in size was incubated for three hours in 140 μ L static human blood plasma containing approximately 3.9×10^6 platelets. Neither intact platelets nor platelet fragments were observed on this device.

Observing no intact platelets or platelet fragments on the flow diverting device #1 piece was a surprising result, especially when a similar plasma incubation volume and platelet concentration was found to promote platelet surface adhesion and aggregation on a p-doped silicon wafer. This experiment should be repeated with varying plasma incubation volumes and platelet concentrations to ascertain the optimal conditions for platelet surface adhesion to the flow diverting device #1; additionally, it is acknowledged that incubating plasma age and device orientation within the incubating plasma volume may play a part in platelet adhesion, so these parameters should be investigated as well.

CHAPTER 6

Discussion

The primary motivation for developing a nanometer-scale hemocompatible and antithrombotic coating for intracranial stents and flow diverting devices is the fact that thromboembolic complications are not insignificant in intracranial aneurysm patients treated endovascularly. In fact, the literature suggests that approximately 5% of patients treated with the Pipeline™ flow diverting device and dual anti-platelet therapy (DAPT), and 7% of patients treated with intracranial stents for stent-assisted coiling and DAPT experience thromboembolic complications.^{7, 10} Furthermore DAPT is associated with increased patient risk, despite being the current standard of care.¹³ Therefore such a coating would at least minimize or at best eliminate the need for endovascularly treated intracranial aneurysm patients to receive DAPT, decreasing or eliminating the associated patient risks; such a coating would also increase intracranial device indications for use to include patients suffering from acute SAH – in short, a coating technology like this has the potential to revolutionize the endovascular treatment of intracranial aneurysms.

Several research groups have recognized the revolutionizing impact surface-modified intracranial stents, in particular, could have on aneurysm patients and have published promising results using the Cordis Bx Velocity™ coronary stent with Hepacoat™ in the human cerebral circulation, or else on the improved in-vitro thrombogenicity of heparin and human serum albumin surface coatings for the Acandis Acclino® stent-assisted coiling device.^{26, 28} Likewise, medical device companies have also recognized the large societal and market impact a hemocompatible and antithrombotic coating technology holds. In 2015 medical device giant Medtronic Inc. published on a nanometer-scale coating they developed for their intracranial Pipeline™ Flex flow diverting device called Shield Technology™ that could be an effective coating technology to mitigate thrombogenic complications.²⁰ Since then other medical device companies have become interested in developing a competitive nanometer-scale antithrombotic coating.

Given the potential for great societal impact, and given the healthy commercial interest in technologies like these, a novel nanometer-scale hemocompatible and

antithrombotic coating chemistry and deposition technique suitable for commercially available intracranial stents and flow diverting devices was developed. Similar to Medtronic's Shield Technology™, the developed coating technology is a nano-scale chemical formulation that is covalently bound to the underlying intracranial device. However, it is unique in the sense that its hemocompatible and antithrombotic functionality is derived from the sequential, covalent attachment of multiple chemical layers, the terminal layer of which contains the naturally derived bioactive and antithrombotic agent human glycoprotein thrombomodulin (hTM), as shown in Figure 2. Inclusion of hTM in this coating chemistry was a targeted effort to actively disrupt the human coagulation cascade; hTM is an integral membrane protein expressed in-vivo on the human endothelial cell surface and actively disrupts coagulation since it acts as a protein cofactor in the thrombin-catalyzed activation of protein C.⁴⁹ Furthermore, the developed coating technology can be modified for use as a platform to covalently attach methoxy-poly(ethylene glycol) amine (or mPEG), a derivative of phosphorylcholine (or PC) called o-phosphorylethanolamine (o-PA), and heparin – which are FDA-approved molecules – in place of the hTM. The ability to include FDA-approved alternatives to hTM in the developed coating technology lessens the amount of verification and validation testing required by the FDA for market approval.

It should be noted that the composition of the chemical layers in the developed coating technology are not novel. In 2014 Zhong et al. published work that used ALD to bond Al₂O₃ to a stainless steel cardiovascular stent surface.⁵⁰ Zhong et al. further modified the Al₂O₃ layer with APTES, which is also done in the developed coating technology; however, the group sequentially attached 2-metacryloyloxyethyl phosphorylcholine to the APTES layer.⁵⁰ Instead, the developed coating technology attaches TCT to the APTES layer, though using TCT as a means to attach hTM was an idea taken from work reported by Yeh and Lin in 2009.⁵¹ Even surface immobilization of hTM is not novel and was first described in 1992 Dr. M. Akashi; thereafter, hTM surface modifications have been proposed by many other research groups.^{21, 44, 52, 112} In spite of the fact that the composition of each individual chemical layer in the developed technology is not novel, their sequential deposition and application to intracranial stents and flow diverting devices is, and is unique to this technology.

To develop the coating technology, and ultimately optimize its hemocompatible and antithrombotic functionality, the individual chemical layers (outlined in Figure 2) were

probed to assess composition and uniformity using a combination of qualitative and quantitative chemical characterization techniques; specifically, scanning electron microscopy (SEM) imaging, X-Ray Photoelectron Spectroscopy (XPS), focused-ion beam (FIB) milling, and confocal microscopy imaging were used. The XPS survey scan shown as Figure 13 indicates that the technology's initial PE-ALD deposited Al_2O_3 layer can be covalently attached to a commercially available intracranial flow diverting device; likewise the SEM images of this layer, shown as Figure 9, suggest that it provides a smooth and a macroscopically conformal coating for further functionalization, even for mesh-dense commercially available flow diverters. These SEM images, together with the XPS elemental maps shown in Figure 14 and the FIB/SEM images shown in Figure 15, corroborate that this PE-ALD deposited Al_2O_3 layer is uniform. The sequential functionalization of this layer with 3-aminopropyl-triethoxy-silane (APTES) on a commercially available flow diverter is indicated by the XPS survey scan shown as Figure 16; in addition, the associated XPS elemental maps in Figure 17 suggest uniform coverage of the APTES molecule on the coated device surface. Likewise, the XPS survey scan shown in Figure 18 suggests that an APTES layer bonded to a commercial flow diverting device can be further functionalized with 2,4,6-trichloro-1,3,5-triazine (TCT); nevertheless, the corresponding XPS elemental maps, shown in Figure 19, as well as the acquired SEM images together indicate that the TCT layer may not be free of defects and can likely be optimized. Despite the potential for defects in a TCT layer bonded to a commercial flow diverting device, the glycoprotein hTM can still be covalently bound to such a layer, as indicated by the XPS survey and nitrogen core level scans, shown as Figures 21 and 22 respectively; furthermore, confocal images of fluorophore labeled TCT and hTM coated flow diverting devices, shown in Figure 23, suggest substantive immobilization of hTM on both the interior and exterior coated device surfaces.

The thicknesses of the technology's individual chemical layers were measured optically by spectroscopic ellipsometry on coated p-doped silicon wafers. This was done using sequential Cauchy models and associated constants determined in consultation with J.A. Woollam engineers and from work published by Gunda et al.¹¹³; the combined thickness of the Al_2O_3 , APTES, and TCT layers was found to be 33.45 ± 0.40 nm. This thickness is corroborated by the associated XPS spectral data (Figures 13, 16, and 18) and FIB/SEM images of coated commercial flow diverting devices (Figure 15).

Furthermore, the thickness of the hTM layer bound to a commercial flow diverting device was estimated by both XPS spectral data (Figure 21) and the molecular weight of the recombinant protein to be less than 3 nm. Thus, the developed coating technology has an overall coating thickness of approximately 40 nm. Putting this in perspective, the thickness of the smallest microwire used to fabricate commercial intracranial devices is approximately 25 μm . With this in mind, the developed technology changes the thickness of any given commercial microwire very minimally (by 0.16%), meaning the technology is unlikely to change the stiffness of potentially malleable device microwires and therefore is unlikely to change the mechanics of the underlying intracranial device. While the mechanics of intracranial devices coated with the technology has not been explicitly explored, a methodology to uniaxially stretch commercially available intracranial flow diverting devices and measure the associated device diameter change is outlined in Appendix A. Appendix A also outlines a methodology developed to assess the pushability of coated commercial flow diverters through their device microsheaths.

In terms of conjugated hTM functionality, both the in-house CAT assay results (Figure 32) and the results of CAT assay testing done by the third-party commercial vendor indicate that hTM is functionally able to reduce thrombin generation in-vitro soon after surface immobilization on commercial #1 flow diverting devices when the associated devices are stored on ice (Figure 33) and when stored at room temperature (Figure 34); furthermore, Figure 34 suggests that the thrombin generating capacity of #1 devices coated with the developed technology in a static, in-vitro environment is comparable to similar flow diverting devices coated with a competitive technology. In addition, TCT coated #1 devices show improved thrombogenicity in static, in-vitro environments compared to uncoated #1 devices, as suggested by both the in-house CAT assay results (Figure 32) and the results of a CAT assay done by the third-party vendor. (Figure 35).

The longitudinal functionality of conjugated hTM is less clear and was assessed via the Shelf Life Study; this study design consisted of coating pieces of commercial flow diverting device #3 with the developed coating technology and assessing the immediate thrombogenicity via the CAT assay at the University of Iowa. The remaining hTM coated #3 device pieces were stored on the shelf at ambient temperature and pressure; their thrombogenicity was assessed via the CAT assay at five time points throughout a 33 week period. The most striking observation from this study, the results of which are

shown as Figure 38, is that bare #3 flow diverting device pieces exhibit large variation in the amount of thrombin they generate; furthermore, bare #3 device pieces are not particularly thrombogenic since in every CAT assay in this study at least some bare device pieces generate as much thrombin as blank wells, save for Week 5 (Figure 38D). This variability is likely impacting the longitudinal thrombin generating capacity of hTM coated #3 flow diverting devices, making it difficult to parse out the individual contribution of conjugated hTM on thrombin generation. More testing is required to evaluate the thrombin generating capacity of bare and hTM coated #3 flow diverting devices, though the trend indicated by this study is that the thrombin generating capacity of the developed coating technology on #3 flow diverting devices in a static, in-vitro environment does not significantly increase longitudinally. The observed variability in thrombin generating capacity of bare and hTM coated #3 devices in this study is likely only minimally impacted by surface area effects caused by testing devices of inconsistent lengths; this is because all devices tested in each shelf life CAT assay were carefully placed in the respective U-bottom microplate well such that, upon visual inspection, one device end was adjacent with the top of the U-bend while the other end was left unsubmerged – in other words, untouched by PRP and CAT assay reagents.

Nevertheless, the developed coating technology was found to have both hemocompatible and antithrombotic properties in-vivo. Results of an initial in-vivo survival study, performed by bilaterally-inserting hTM coated commercial stent-assisted coiling #4 devices into the carotid arteries of porcine models at the University of Iowa, were that all five animals were alive at the study end point (five days) and none exhibited neurological deficits on exam throughout the study, or else at euthanasia. A gross inspection of the excised #4 devices, done by a practicing neurosurgeon, indicated that eight devices were patent upon excision, while two devices exhibited major thrombosis thought to be caused by crimping of the device ends. Due to the age of the digital fluoroscopic x-ray used during surgery to position and deploy each device, it is unknown whether the device crimping occurred during deployment or during the excision procedure. However, the associated MRI head and neck scans just prior to euthanasia indicated no brain lesions or strokes in any of the animals; likewise, the time-of-flight MRA head and neck scans just prior to euthanasia indicated good blood flow distal to the device implantation sites in each animal. Since the hTM coated #4 devices in this study were sterilized with a commercial electron beam sterilization technique prior to implantation, observing no brain lesions or stroke in the animals suggests that the

developed coating technology may be commercially feasible. Additionally, two ex-vivo studies, using an established primate arteriovenous (AV) model⁷⁹⁻⁸⁴, were performed at the Oregon National Primate Research Center (ONPRC) to give insight into the platelet and fibrin deposition associated with coated commercially available flow diverting devices (#2 and #5) deployed alone, in combination with systemic aspirin, and in combination with DAPT (refer to Figure 39). The primary findings of these two ex-vivo primate shunt studies are: 1) the developed coating technology is functional on relatively short #2 devices without combined systemic anticoagulant use; in other words, short hTM coated #2 devices deployed alone accumulate fewer platelets (Figure 39C) and have decreased fibrin deposition (Figure 39A) ex-vivo when compared to bare #2 devices; however, short coated #2 devices deployed alone still accumulate more platelets and fibrin over time than bare #2 devices deployed in combination with DAPT and 2) the functionality of the developed coating technology is enhanced for relatively long #5 devices by combining their deployment with the administration of systemic aspirin; long hTM coated #5 devices deployed in combination with aspirin accumulate fewer platelets (Figure 39D) and fibrin (Figure 39B) over time than bare #5 devices and show similar platelet accumulation and fibrin deposition as bare #5 devices deployed in combination with DAPT. Since the hTM coated flow diverting devices in this study were sterilized with commercial electron beam sterilization techniques prior to implantation, observing no particularly deleterious effects in the animals further suggests that the developed coating technology may be commercially feasible.

Furthermore, the developed coating technology can be modified for use as a platform to covalently attach methoxy-poly(ethylene glycol) amine (or mPEG), a derivative of phosphorylcholine (PC) called o-phosphorylethanolamine (o-PA), and heparin – which are FDA-approved molecules – in place of the hTM. The ability to include FDA-approved alternatives to hTM in the developed coating technology lessens the amount of verification and validation testing required by the FDA for market approval, making the pathway to commercialization easier. XPS spectral data acquired on a commercial #5 flow diverting device coated with the developed technology platform and mPEG indicate covalent attachment of the FDA-approved molecule when a TCT coated #5 device is incubated in solutions of 60 mg/mL mPEG (Figures 58 and 59) and 100 mg/mL mPEG (Figures 60 and 61). Likewise XPS spectral data acquired on a #5 device coated with the developed technology platform and heparin indicate covalent attachment of the FDA-approved molecule when an APTES coated #5 device is incubated in MES

buffer containing heparin sodium salt (Figure 44); incubation in a more basic reaction containing sodium carbonate-bicarbonate buffer and heparin sodium salt does not yield covalent attachment of heparin to the device surface and was actually found to degrade the underlying APTES and Al₂O₃ layers (refer to XPS spectral data in Figure 47). Finally, XPS spectral data acquired on a #5 flow diverting device coated with the developed technology platform and o-PA indicate covalent attachment of the FDA-approved molecule when a TCT coated #5 device is incubated in a solution of deionized water and o-PA (Figures 55 and 56).

Moreover, the developed platform technology possesses favorable hemocompatible and antithrombotic properties in-vitro when mPEG and heparin are individually conjugated to commercial #5 flow diverting devices. To assess this, CAT assay testing was performed by Haematologic Technologies Incorporated (HTI), a third-party ISO 9001:2015 certified company with experience using the assay to test the in-vitro thrombogenicity of intravenous immune globulin (IVIG) therapy pharmaceuticals. Through collaboration with HTI hematologists, the in-house CAT assay protocol was adapted for use at the HTI facility for coated and control #5 devices. The associated HTI CAT assay results are shown in Figure 65 and indicate that the hTM, TCT, and o-PA-DI coating chemistries do little to improve the thrombogenicity inherent to the bare #5 flow diverting device. In contrast, the heparin-MES, PEG-60, and PEG-100 coating chemistries provide some improvement in #5 device thrombogenicity. This experiment also reveals that there seems to be large variability in the thrombin generating capacity of commercially available #1 and #5 flow diverting devices; in fact, both inter- and intra-device related differences in thrombin generating capacity exist. Despite the small sample size in this study, which does not lend itself to statistical analyses, the observation that the Heparin-MES, PEG-60, and PEG-100 coated #5 devices have the least amount of intra-device variability in thrombin generation, and the smallest peak thrombin concentrations overall, suggest that they are the most promising coating formulations and should be selected for further optimization and testing.

Despite the promising nature of the developed technology as a nanometer-scale hemocompatible and antithrombotic coating suitable for commercially available intracranial stents and flow diverting devices, the studies described herein are not without limitations, chief among them is the fact that this was not a hypothesis driven endeavor, but rather an exploratory and developmental pursuit. As a result, every study

discussed herein possessed small sample sizes not conducive to statistical testing. This was in part due to a lack of large numbers of identical commercial intracranial devices for testing, and in part due to high experimental costs – most notably associated with the in-vivo tests, but also in purchasing the necessary CAT assay reagents from Thrombinoscope; to compensate, we chose to perform multiple in-vitro and in-vivo studies complete with testing by third-party vendors (like ONPRC and HTI). Likewise, we chose to utilize multiple qualitative and quantitative chemical characterization techniques to assess composition, uniformity, and thickness of the individual coating layers. Nevertheless, the sample sizes for the comparisons discussed herein should be increased for a more conclusive assessment of the developed coating technology. Additionally, there is no good animal model for acute stroke ⁷⁸; as a result, the thrombogenicity of the developed coating technology was evaluated via an established primate model ⁷⁹⁻⁸⁴, as well as a porcine model whose vascular dimensions roughly matched that of an adult human. Another limitation is that the in-vivo porcine study lacked a control; likewise, the ex-vivo primate shunt experiment with commercial flow diverting #2 devices did not test hTM coated devices deployed in combination with aspirin – such a test would have given more insight into whether devices coated with the developed technology could minimize the must-use adjunctive therapy of DAPT to aspirin only in the clinical setting.

Both the initial and longitudinal functionality of the conjugated hTM in the developed technology requires further evaluation. While the in-house CAT assay results, as well as those performed by the third-party commercial vendor, on hTM coated #1 devices suggested favorable decreases in the associated in-vitro thrombin generating capacity, similar CAT assay results performed at the University of Iowa on hTM coated #3 flow diverting devices as part of the shelf life study show no improvement in the associated in-vitro thrombin generating capacity at many of the study time points. Likewise, the CAT assay performed by HTI suggests the same for hTM coated #5 flow diverting devices. The sensitivity of the CAT assay to coated and control intracranial devices should be rigorously and independently assessed. Additionally, the variability in the in-vitro thrombin generation capacity of different commercial intracranial devices suggests that each device requires its own independent evaluation. Given the high cost associated with in-vivo thrombogenicity testing, other in-vitro thrombogenicity tests should be explored. The Protein C Activation assay and the static platelet seeding and incubation experiments discussed in Chapter 5 are both promising in-vitro testing

alternatives. Nevertheless, it is acknowledged that testing this technology in human subjects is the only way to conclusively assess its functionality; therefore, the findings discussed herein should be taken only as evidence for the potential of this technology to minimize the adjunctive use of dual-antiplatelet therapy in the endovascular treatment of intracranial aneurysms.

Conclusion

The developed coating technology is a multilayer, nanometer-scale chemical formulation that can be covalently bound to commercially available intracranial stents and flow diverters in a conformal manner, with some demonstrated hemocompatible and antithrombotic properties in-vitro and in-vivo. In addition, it can be used as a platform technology for the attachment of FDA-approved molecules including heparin and derivatives of polyethylene glycol and phosphorylcholine. With further optimization and testing this technology has the potential to minimize the adjunctive use of dual-antiplatelet therapy in the endovascular treatment of intracranial aneurysms.

REFERENCES

1. Weir B. Unruptured Intracranial Aneurysms: A Review. *J Neurosurg* 2002;96:3-42
2. Juvela S, Porras M, Poussa K. Natural History of Unruptured Intracranial Aneurysms: Probability of and Risk Factors for Aneurysm Rupture. *J Neurosurg* 2000;93:379-387
3. Johnston SC. Effect of Endovascular Services and Hospital Volume on Cerebral Aneurysm Treatment Outcomes. *Stroke* 2000;31
4. Molyneux A, Group ISATIC. International Subarachnoid Aneurysm Trial (ISAT) of Neurosurgical Clipping Versus Endovascular Coiling in 2143 Patients with Ruptured Intracranial Aneurysms: A Randomized Trial. *Lancet Neurol* 2002;360:1267-1274
5. Administration USFaD. Neuroform Microdelivery Stent System - H020002. 2013
6. Bodily KD, Cloft HJ, Lanzino G, et al. Stent-Assisted Coiling in Acutely Ruptured Intracranial Aneurysms: A Qualitative, Systematic Review of the Literature. *AJNR* 2011;32:1232-1236
7. Shapiro M, Becske T, Sahlein D, et al. Stent-Supported Aneurysm Coiling: A Literature Survey of Treatment and Follow-up. *AJNR* 2012;33:159-163
8. Administration USFaD. Pipeline Embolization Device - P100018. 2013
9. Fischer S, Vajda Z, Perez MA, et al. Pipeline Embolization Device (PED) for Neurovascular Reconstruction: Initial Experience in the Treatment of 101 Intracranial Aneurysms and Dissections. *Neuroradiology* 2012;54:369-382
10. Kallmes DF, Hanel R, Lopes D, et al. International Retrospective Study of the Pipeline Embolization Device: A Multicenter Aneurysm Treatment Study. *AJNR* 2015;36:108-115
11. Alderazi Y, Shastri D, Kass-Hout T, et al. Flow Diverters for Intracranial Aneurysms. *Stroke Res Treat* 2014;2014:415653-415653
12. Fiorella D. Anti-Thrombotic Medications for the Neurointerventionist: Aspirin and Clopidogrel. *J NeuroIntervent Surg* 2010;2:44-49
13. ACC/AHA 2002 Guideline Update for the Management of Patients with Unstable Angina and Non-ST-Segment Elevation Myocardial Infarction—Summary Article: A Report of the American College of Cardiology/American Heart Association Task Force on Practice Guidelines

(Committee on the Management of Patients With Unstable Angina).
Journal of the American College of Cardiology 2002;40:1366 - 1374

14. Nazneen F, Herzog G, Arrigan D, et al. Surface Chemical and Physical Modification in Stent Technology for the Treatment of Coronary Artery Disease. *J Biomed Mater Res Part B* 2012;100B:1989-2014
15. Hoffman R, Benz E, Silberstein L, et al. *Hematology: Basic Principles and Practice*. Elsevier Inc.; 2013
16. Pallister CJ, Watson MS. *Haematology*. Scion Publishing Ltd.; 2009
17. Hemker HC, Beguin S. Thrombin Generation in Plasma: Its Assessment Via the Endogenous Thrombin Potential. *Thromb Haemo* 1995;74:134-138
18. Hemker HC, Giesen P, Al Dieri R, et al. Calibrated Automated Thrombin Generation Measurement in Clotting Plasma. *Pathophysiol Haemost Thromb* 2003;33:4-15
19. *Transfusion Medicine and Hemostasis: Clinical and Laboratory Aspects*. Elsevier Inc.; 2013
20. Girdhar G, Li J, Kostousov L, et al. In-Vitro Thrombogenicity Assessment of Flow Diversion and Aneurysm Bridging Devices. *J Thromb Thrombolysis* 2015;40:437-443
21. Qi P, Maitz M, Huang N. Surface Modification of Cardiovascular Materials and Implants. *Surf Coat Tech* 2013;233:80-90
22. Werner C, Maitz M, Sperling C. Current Strategies Towards Hemocompatible Coatings. *J Mater Chem* 2007;17:3376-3384
23. Nishi S, Nakayama Y, Ishibashi-Ueda H, et al. Occlusion of Experimental Aneurysms with Heparin-Loaded, Microporous Stent Grafts. *Neurosurgery* 2003;53:1397-1405
24. Rangwala HS, Ionita CN, Rudin S, et al. Partially Polyurethane-Covered Stent for Cerebral Aneurysm Treatment. *J Biomed Mater Res Part B: App Biomater* 2008;415-429
25. Levy EI, Boulos AS, Hanel RA, et al. In Vivo Model of Intracranial Stent Implantation: A Pilot Study to Examine the Histological Response of Cerebral Vessels After Randomized Implantation of Heparin-Coated and Uncoated Endoluminal Stents in a Blinded Fashion. *J Neurosurg* 2003;98:544-553

26. Parkinson RJ, Demers CP, Adel JG, et al. Use of Heparin-Coated Stents in Neurovascular Interventional Procedures: Preliminary Experience with 10 Patients. *Neurosurgery* 2006;59:812-821
27. Levy EI, Hanel RA, Tio FO, et al. Safety and Pharmacokinetics of Sirolimus-Eluting Stents in the Canine Cerebral Vasculature: 180 Day Assessment. *Neurosurgery* 2006;59:925-934
28. Krajewski S, Neumann B, Kurz J, et al. Preclinical Evaluation of the Thrombogenicity and Endothelialization of Bare Metal and Surface-Coated Neurovascular Stents. *AJNR* 2015;36:133-139
29. Hynninen V, Vuori L, Hannula M, et al. Improved Antifouling Properties and Selective Biofunctionalization of Stainless Steel by Employing Heterobifunctional Silane-Polyethylene Glycol Overlayers and Avidin-Biotin Technology. *Sci Rep* 2016;6:1-12
30. Santos M, Filipe EC, Michael PL, et al. Mechanically Robust Plasma-Activated Interfaces Optimized for Vascular Stent Applications. *ACS Appl Mater Interfaces* 2016;8:9635-9650
31. Leslie DC, Waterhouse A, Berthet JB, et al. A Bioinspired Omniphobic Surface Coating on Medical Devices Prevents Thrombosis and Biofouling. *Nature Biotech* 2014;32:1134-1140
32. Hoppe A. A Review of Hemocompatible Surface Modification and Coating Strategies for Intravascular Stents. *Surfaces in Biomaterials Foundation SurFACTS in Biomaterials Newsletter*, Winter 2015
33. Sydow-Plum G, Tabrizian M. Review of Stent Coating Strategies: Clinical Insights. *Mater Sci Tech* 2008;24:1127-1143
34. Tahtinen O, Vanninen R, Manninen H, et al. Wide-Necked Intracranial Aneurysms: Treatment with Stent-Assisted Coil Embolization During Acute (<72 Hours) Subarachnoid Hemorrhage - Experience in 61 Consecutive Patients. *Radiology* 2009;253:199-208
35. Higashida R, Meyers P, Connors J, et al. Intracranial Angioplasty & Stenting for Cerebral Atherosclerosis: A Position Statement of the American Society of Interventional and Therapeutic Neuroradiology, Society of Interventional Radiology, and the American Society of Neuroradiology. *Am J Neuroradiol* 2005;26:2323
36. Hauert R. A Review of Modified DLC Coatings for Biological Applications. *Diam Relat Mater* 2003;12:583-589
37. Trigwell S, Hayden R, Nelson K, et al. Effects of Surface Treatment on the Surface Chemistry of NiTi Alloy for Biomedical Applications. *Surf Interface Anal* 1998;26:483-489

38. Gutensohn K, Beythien C, Bau J, et al. In Vitro Analyses of Diamond-like Carbon Coated Stents: Reduction of Metal Ion Release, Platelet Activation, and Thrombogenicity. *Thromb Res* 2000;99:577-585
39. Bertrand O, Sipehia R, Mongrain R, et al. Biocompatibility Aspects of New Stent Technology. *J Am Coll Cardiol* 1998;32:562-571
40. Phaneuf M, Berceci S, Bide M, et al. Covalent Linkage of Recombinant Hirudin to Poly(ethylene terephthalate) (Dacron): Creation of a Novel Antithrombin Surface. *Biomaterials* 1997;18:755-765
41. Maitz M, Sperling C, Werner C. Immobilization of the Irreversible Thrombin Inhibitor D-Phe-Pro-Arg-Chloromethylketone: A Concept for Hemocompatible Surfaces? *J Biomed Mater Res A* 2010;94A:905-912
42. Gouzy M, Sperling C, Salchert K, et al. In Vitro Blood Compatibility of Polymeric Biomaterials Through Covalent Immobilization of an Amidine Derivative. *Biomaterials* 2004;25:3493-3501
43. Dittman W, Majerus P. Structure and Function of Thrombomodulin: A Natural Anticoagulant. *J Am Soc Hematol* 1990;75:329-336
44. Akashi M, Maruyama I, Fukudome N, et al. Immobilization of Human Thrombomodulin on Glass Beads and its Anticoagulant Activity. *Bioconjug Chem* 1992;3:363-365
45. Sperling C, Salchert K, Streller U, et al. Covalently Immobilized Thrombomodulin Inhibits Coagulation and Complement Activation of Artificial Surfaces In Vitro. *Biomaterials* 2003;25:5101-5113
46. Jen M, Serrano M, van Lith R, et al. Polymer-Based Nitric Oxide Therapies: Recent Insights for Biomedical Applications. *Adv Funct Mater* 2012;22:239-260
47. Weng Y, Song Q, Zhou Y, et al. Immobilization of Selenocystamine on TiO₂ Surfaces for In Situ Catalytic Generation of Nitric Oxide and Potential Application in Intravascular Stents. *Biomaterials* 2011;32:1253-1263
48. Affairs MNC. Pipeline™ Flex Embolization Device With Shield Technology™ Clinical Study (PFLEX). In: Health USNIo, ed.: ClinicalTrials.gov; 2015
49. Suzuki K, Kusumoto H, Deyashiki Y, et al. Structure and Expression of Human Thrombomodulin, A Thrombin Receptor on Endothelium Acting as a Cofactor for Protein C Activation. *EMBO J* 1987;6:1891-1897
50. Zhong Q, Yan J, Qian X, et al. Atomic Layer Deposition Enhanced Grafting of Phosphorylcholine on Stainless Steel for Intravascular Stents. *Colloids and Surfaces B:Biointerfaces* 2014;121:238-247

51. Yeh H-Y, Lin J-C. Bioactivity and Platelet Adhesion Study of a Human Thrombomodulin-Immobilized Nitinol Surface. *J Biomater Sci* 2009;20:807-819
52. Wong G, Li J-m, Hendricks G, et al. Inhibition of Experimental Neointimal Hyperplasia by Recombinant Human Thrombomodulin Coated ePTFE Stent Grafts. *J Vasc Surg* 2007;47:608-615
53. Foroughi-Abari A, Cadien K. Atomic Layer Deposition for Nanotechnology. *Nanofabrication: Vienna* : Springer Vienna 2012
54. Jugessur A. UIMF Training Module 2: Plasma Etching and Thin-Film Technologies. University of Iowa Microfabrication Facility,; 2014
55. George S. Atomic Layer Deposition: An Overview. *Chem Rev* 2010;110:111-131
56. Instruments O. Atomic Layer Deposition Systems: ALD Process Solutions using FlexAL and OpAL. 2011
57. Rai V, Vandalon V, Agarwal S. Surface Reaction Mechanisms During Ozone and Oxygen Plasma Assisted Atomic Layer Deposition of Aluminum Oxide. *Langmuir* 2010;26:13732-13735
58. Heil SBS, van Hemmen JL, van de Sanden MCM, et al. Reaction Mechanisms During Plasma-Assisted Atomic Layer Deposition of Metal Oxides: A Case Study for Al₂O₃. *J Appl Physics* 2008;103:103302-103301-103314
59. Ensminger D, Foster B. *Ultrasonics: Data, Equations, and their Practical Uses*. CRC Press; 2008
60. Jellison Jr. GE. Spectroscopic Ellipsometry Data Analysis: Measured versus Calculated Quantities. *Thin Solid Films* 1998;313-314:33-39
61. Ploetz E, Visser B, Slingenbergh W, et al. Selective Functionalization of Patterned Glass Surfaces. *J Mater Chem B* 2014;2:2606-2615
62. Niimi S, Oshizawa T, Naotsuka M, et al. Establishment of a Standard Assay Method for Human Thrombomodulin and Determination of the Activity of the Japanese Reference Standard. *Biologicals* 2002;30:69-76
63. Goldstein J, Newbury DE, Joy DC, et al. *Scanning Electron Microscopy and X-ray Microanalysis* Third ed. New York: Springer; 2003:21-60
64. Moulder J, Stickle W, Sobol P, et al. *Handbook of X-ray Photoelectron Spectroscopy*. Eden Prairie, MN: Perkin-Elmer Corporation; 1992
65. Medtronic-Covidien. The Pipeline Embolization Device. 2011:1-4

66. Drobne D, Milani M, Leser V, et al. Surface Damage Induced by FIB Milling and Imaging of Biological Samples is Controllable. *Microscopy Research and Technique* 2007;70:895-903
67. Yao N. *Focused Ion Beam Systems: Basics and Applications*. Cambridge University Press; 2007:1-409
68. *Basic Confocal Microscopy*. Springer Science+Business Media, LLC; 2011
69. Hemker HC, Kremers R. Data Management in Thrombin Generation. *Thromb Res* 2013;131:3-11
70. Giesen P. The Thrombogram Guide. In: S.A.S. DS, ed.; 2012
71. Berry L, Chan A. Methods in Molecular Biology. In: Monagle P, ed. *Haemostasis Methods and Protocols*. New York: Springer Science+Business Media; 2013:139-154
72. Key N, Makris M, O'Shaughnessy D, et al. *Practical Hemostasis and Thrombosis*. Wiley-Blackwell; 2009
73. Hoffbrand V, Moss P. *Essential Haematology*. Wiley-Blackwell; 2011
74. Chandler W, Roshal M. Optimization of Plasma Fluorogenic Thrombin-Generation Assays. *Am J Clin Pathol* 2009;132:169-179
75. Hemker HC, Hemker PW, Al Dieri R. The Technique of Measuring Thrombin Generation with Fluorescent Substrates: 4. The H-Transform, A Mathematical Procedure to Obtain Thrombin Concentrations Without External Calibration. *Thromb Haemost* 2009;101:1-7
76. Chapra SC. *Applied Numerical Methods with Matlab: For Engineers and Scientists*. McGraw-Hill; 2012
77. Wagenvoort R, Hemker PW, Hemker HC. The Limits of Simulation of the Clotting System. *J Thromb Haemost* 2006;4:1331-1338
78. Culp W, Erdem E, Roberson P, et al. Microbubble Potentiated Ultrasound as a Method of Stroke Therapy in a Pig Model: Preliminary Findings. *J Vasc Interv Radiol* 2003;14:1433-1436
79. Larsen K, Cheng C, Tempel D, et al. Capture of Circulatory Endothelial Progenitor Cells and Accelerated Re-Endothelialization of a Bio-Engineered Stent in Human Ex-Vivo Shunt and Rabbit Denudation Model. *Eur Heart J* 2012;33:120-128
80. Verheye S, Markou CP, Salame MY, et al. Reduced Thrombosis Formation by Hyaluronic Acid Coating of Endovascular Devices. *Arterio Thromb Vasc Biol* 2000;20:1168-1172

81. Harker LA, Marzec UM, Kelly AB, et al. Clopidogrel Inhibition of Stent, Graft, and Vascular Thrombogenesis with Antithrombotic Enhancement by Aspirin in Nonhuman Primates. *Circulation* 1998;98:2461-2469
82. Sundell IB, Marzec UM, Kelly AB, et al. Reduction in Stent and Vascular Graft Thrombosis and Enhancement of Thrombolysis by Recombinant Lys-plasminogen in Nonhuman Primates. *Circulation* 1997;96:941-948
83. Krupski WC, Bass A, Kelly AB, et al. Heparin-Resistant Thrombus Formation by Endovascular Stents in Baboons: Interruption by a Synthetic Antithrombin. *Circulation* 1990;82:570-577
84. Krupski WC, Bass A, Kelly AB, et al. Reduction in Thrombus Formation by Placement of Endovascular Stents at Endarterectomy Sites in Baboon Carotid Arteries. *Circulation* 1991;84:1749-1757
85. Tucker EI, Marzec UM, White TC, et al. Prevention of Vascular Graft Occlusion and Thrombus-Associated Thrombin Generation by Inhibition of Factor XI. *Blood* 2009;113:936-944
86. Tucker EI, Marzec UM, Berny MA, et al. Hemostatic Safety and Antithrombotic Efficacy of Moderate Platelet Count Reduction by Thrombopoietin Inhibition in Primates. *Sci Transl Med* 2010;2
87. Gruber A, Marzec UM, Bush L, et al. Relative Antithrombotic and Antihemostatic Effects of Protein C Activator Versus Low-Molecular-Weight Heparin in Primates. *Blood* 2007;109:3733-3740
88. Gruber A, Hanson SR. Factor XI-Dependence of Surface- and Tissue Factor-Initiated Thrombus Propagation in Primates. *Blood* 2003;102:953-955
89. Hanson SR, Kotze HF, Savage B, et al. Platelet Interactions with Dacron Vascular Grafts: A Model of Acute Thrombosis in Baboons. *Arteriosclerosis* 1985;5:595-603
90. Administration USFaD. FDA Approved Drug Products:Argatroban. In: Administration USFaD, ed.; 2000
91. Administration USFaD. FDA Approved Drug Products: REFLUDAN (LEPIRUDIN RECOMBINANT). In: Administration USFaD, ed.; 1998
92. Services VPBM, Panel MA, Executives VP. Drug Class Review: Target Specific Oral Anticoagulants Dabigatran (Pradaxa), Rivaroxaban (Xarelto), and Apixaban (Eliquis). In: Affairs USDoV, ed.; 2013
93. Mero A, Clementi C, Veronese FM, et al. Covalent Conjugation of Poly(Ethylene Glycol) to Proteins and Peptides: Strategies and Methods. In: Mark SS, ed. *Bioconjugation Protocols: Strategies and Methods*,

Methods in Molecular Biology: Springer Science+Business Media, LLC; 2011

94. Michel R, Pasche S, Textor M, et al. Influence of PEG Architecture on Protein Adsorption and Conformation. *Langmuir* 2005;21:12327-12332
95. Administration USFaD. FDA Approved Drug Products: MIRCERA (METHOXY POLYETHYLENE GLYCOL-EPOETIN BETA). In: Administration USFaD, ed.; 2007
96. Lewis AL, Stratford PW. Phosphorylcholine-Coated Stents. *J Long Term Eff Med Implants* 2002;12:231-250
97. Whelan DM, van der Giessen WJ, Krabbendam SC, et al. Biocompatibility of Phosphorylcholine Coated Stents in Normal Porcine Coronary Arteries. *Heart* 2000;83:338-345
98. Kuiper KK, Robinson KA, Chronos NA, et al. Phosphorylcholine-Coated Metallic Stents in Rabbit Iliac and Porcine Coronary Arteries. *Scand Cardiovasc J* 1998;32:261-268
99. Chen C, Lumsden AB, Ofenloch JC, et al. Phosphorylcholine Coating of ePTFE Grafts Reduces Neointimal Hyperplasia in Canine Model. *Ann Vasc Surg* 1997;11:74-79
100. Administration USFaD. Premarket Approval: BIODIVYSIO AS PS (PHOSPHORYLCHOLINE)COATED STENT DELIVERY SYSTEM. In: Administration USFaD, ed.; 2000
101. Gore S, Andersson J, Biran R, et al. Heparin Surfaces: Impact of Immobilization Chemistry on Hemocompatibility and Protein Adsorption. *J Biomed Mat Res B: App Biomat* 2014;102B:1817-1824
102. Administration USFaD. Safety Communications: Medical Devices and Diagnostic Products that May Contain or Be Coated with Heparin. In: Administration USFaD, ed.; 2013
103. Segev A, Aviezer D, Safran M, et al. Inhibition of Vascular Smooth Muscle Cell Proliferation by a Novel Fibroblast Growth Factor Receptor Antagonist. *Cardiovasc Res* 2002;53:232-241
104. Tebbe D, Thull R, Gbureck U. Influence of Spacer Length on Heparin Coupling Efficiency and Fibrinogen Adsorption of Modified Titanium Surfaces. *Biomed Engin Online* 2007;6
105. Abuchowski A, van Es T, Palczuk NC, et al. Alteration of Immunological Properties of Bovine Serum Albumin by Covalent Attachment of Polyethylene Glycol. *J Biol Chem* 1977;252:3578-3581

106. Han H-S, Wu H-L, Lin B-T, et al. Effect of Thrombomodulin on Plasminogen Activation. *Fibrin Proteol* 2000;14:221-228
107. Tepe G, Wendel H, Khorchidi S, et al. Thrombogenicity of Various Endovascular Stent Types: An In Vitro Evaluation. *J Vasc Interv Radiol* 2002;13:1029-1035
108. Chandler AB. In Vitro Thrombotic Coagulation of Blood: A Method for Producing a Thrombus. *Lab Invest* 1958;7:110-116
109. Smith Jr. DM, Summers SH. *Platelets*. Arlington, Virginia: American Association of Blood Banks; 1988
110. Okpalugo TIT, Ogwu AA, Maguire PD, et al. Platelet Adhesion on Silicon Modified Hydrogenated Amorphous Carbon Films. *Biomaterials* 2004;25:239-245
111. Qi R, Yatomi Y, Ozaki Y. Effects of Incubation Time, Temperature, and Anticoagulants on Platelet Aggregation in Whole Blood. *Thromb Res* 2001;101:139-144
112. Sperling C, Salchert K, Streller U, et al. Covalently Immobilized Thrombomodulin Inhibits Coagulation and Complement Activation of Artificial Surfaces In Vitro. *Biomaterials* 2004;25:5101-5113
113. Gunda NSK, Singh M, Norman L, et al. Optimization and Characterization of Biomolecule Immobilization on Silicon Substrates Using (3-aminopropyl)triethoxysilane (APTES) and Glutaraldehyde Linker. *App Surf Sci* 2014;305:522-530
114. ASTM International Subcommittee F04.15 MTM. Standard Test Method for Tension Testing of Nickel-Titanium Superelastic Materials F2516. *Annual Book of ASTM Standards*. West Conshohocken, PA; 2014
115. Jedwab MR, Clerc CO. A Study of the Geometrical and Mechanical Properties of a Self-Expanding Metallic Stent - Theory and Experiment. *J Appl Biomat* 1993;4:77-85
116. Nuutinen J-P, Clerc C, Reinikainen R, et al. Mechanical Properties and In Vitro Degradation of Bioabsorbable Self-Expanding Braided Stents. *J Biomater Sci Polymer Ed* 2003;14:255-266
117. Heller RS, Malek AM. Parent Vessel Size and Curvature Strongly Influence Risk of Incomplete Stent Apposition in Enterprise Intracranial Aneurysm Stent Coiling. *AJNR* 2011;32:1714-1720

APPENDIX A

Methodology for Evaluating Intracranial Flow Diverting Device Stiffness: Uniaxial Extension

One way to assess the stiffness of an intracranial stent or flow diverting device is to uniaxially stretch the device and measure the force required to hold the stretch.¹¹⁴⁻¹¹⁶ Stiff devices will require more force to stretch, while flexible devices will stretch easily with small applied forces. Such uniaxial tensile testing can be done to assess stiffness of both intracranial stents and flow diverting devices; however, for flow diverting devices alone the respective change in device diameter in response to a uniaxial force is another metric of physical importance, since these devices are first stretched uniaxially and then loaded into their respective deployment microcatheters. It is therefore the capability of commercially available flow diverting devices to decrease in diameter when stretched that determines the ease in which these devices can be placed in their microcatheters. This means that the stiffness of commercial flow diverting devices can be determined by measuring the respective device diameter change in response to a uniaxially applied force. The stiffness of both types of intracranial devices is important because the cerebral blood vessels can be highly tortuous and if said devices are too stiff they will not be able to conform to the vessel geometry, ultimately leading to adverse complications for the patient.^{9, 117}

Given the importance of intracranial device stiffness, a uniaxial tensile testing methodology was developed to assess the stiffness of commercial intracranial devices. This method was developed specifically for commercial flow diverting devices, since the test measures the respective device diameter change in response to a uniaxially applied force. The developed tensile testing methodology uses a uniaxial extension tester (manufactured by MTS Systems Corporation, Eden Prairie, MN) to extend a commercial flow diverting device at a fixed rate and measures the corresponding extension force. In this methodology, a digital camera is used to film the tensile test; subsequently, ImageJ image processing software is used to measure the diameter of the device from the film. To assess the repeatability of the developed testing methodology, a single commercial flow diverting device #1 was extended 12 times in the uniaxial extension tester and the force-device diameter data was measured following the testing methodology. A photo of

the device clamped into the uniaxial extension tester prior to extension is shown as Figure A1.

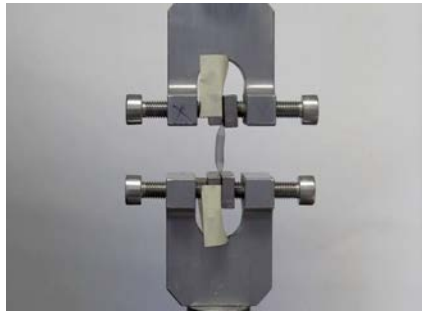


Figure A1: A commercial flow diverting device #1 clamped in the MTS uniaxial extension tester

Initially testing was done with this single flow diverting device to assess the repeatability of deformation. To do this the device was stretched by approximately 170% (from an initial compressed position) in the uniaxial tester and the corresponding force-device diameter data was measured following the testing methodology (n=3). Next to assess whether the device placement in the clamps affected the force or diameter measurements, the device was taken out of the clamps, re-positioned in them, then extended by 170% from the same initially compressed position (n=3).

In order to make the developed testing methodology easier to execute given a broad range of flow diverting device sizes, the same #1 device was again extended in the extension tester, but this time the extension was done from an initial position whereby the measured force was zero (i.e. a zero position). From this zero position the device was compressed by 7% and then extended by approximately 134% (n=3). Again these tests were filmed with a digital camera and the corresponding device diameter was measured via ImageJ. To assess whether the device placement in the clamps affected the force or diameter measurements, the device was taken out of the clamps, re-positioned in them, and then extended by 134% from the zero position (n=3). The force-device diameter data measured from these six tests, as well as the six tests performed from the initially compressed position, is shown as Figure A2.

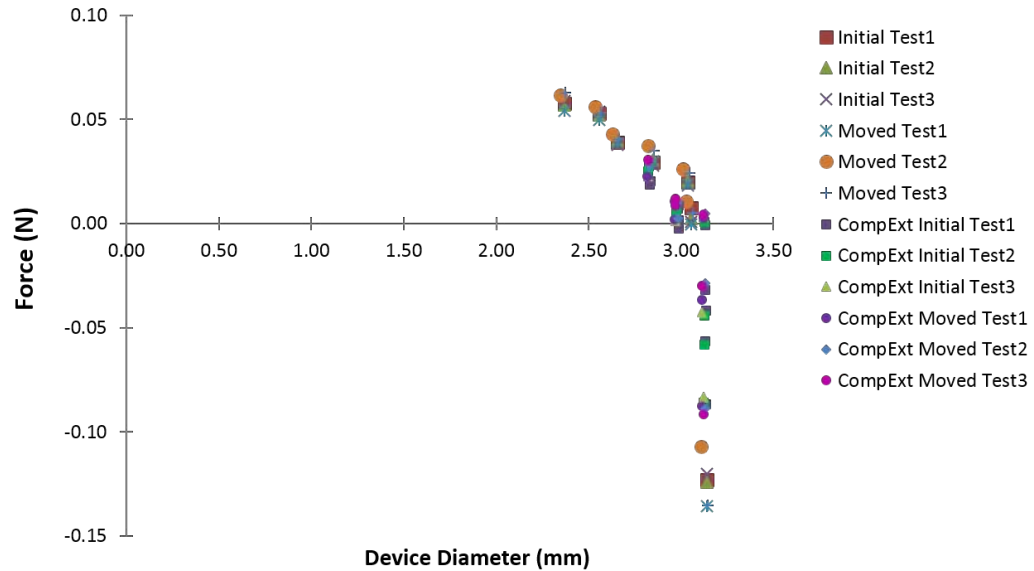


Figure A2: The force-device diameter data from a commercial flow diverting device #1 stretched by approximately 170% in the MTS extension tester ($n=3$, Initial Test1-Test3) then re-positioned in the clamps and stretched by approximately 170% again ($n=3$, Moved Test1-Test3). The force-diameter data from the same device first compressed from an initial zero position and then stretched by the MTS extension tester ($n=3$, CompExt Initial Test1-Test3) and re-positioned in the clamps, compressed, then stretched is also shown ($n=3$, CompExt Moved Test1-Test3)

As can be seen from Figure A2, regardless of whether a #1 flow diverting device is extended from an initially compressed position or first compressed then extended from an initial zero position the measured extension forces and device diameters are similar. Likewise the position of the device in the uniaxial extension tester clamps does not affect the measured extension forces and device diameters. In other words, the force-diameter data gleaned from extending a #1 device from an initially compressed position or first compressing then extending the device from an initial zero position is equivalent and independent of clamp position.

Methodology for Computing Intracranial Device-Associated Friction in Microsheath

The friction associated with pushing an intracranial stent or flow diverting device through its microsheath is an important clinical metric since it influences a neuroradiologist's decision regarding what brand of device to use in his or her clinic. Devices that are easier to push through their microsheath, or are more pushable, are more attractive to neuroradiologists. In addition to clinical importance, Medtronic has reported that their Shield Technology™ offers increased pushability through the

microsheath as compared to bare devices. Therefore, because device pushability is clinically importance and is a metric intracranial stent and flow diverter manufacturers use to market their devices, we sought to develop a methodology for assessing intracranial device-associated friction. The developed friction testing methodology uses a uniaxial extension tester (manufactured by MTS Systems Corporation, Eden Prairie, MN) to pull a commercial flow diverting device at a fixed rate through its microsheath. The MTS extension tester measures the force required to pull the device through the microsheath; this extension force is equal in magnitude but opposite in direction to the device-associated frictional force. Specifically, in this testing methodology both the device guidewire and deployment microsheath are clamped into the uniaxial extension tester. The clamp holding the sheath is kept fixed while the clamp holding the guidewire is allowed to move at a fixed extension rate, effectively pulling the device through sheath; the load cell within the uniaxial extension tester measures the associated pulling force. To assess the sensitivity of the extension tester load cell to measure small changes in device friction, a single commercial flow diverting device #2 was pulled by the uniaxial extension tester through six inches of its microsheath oriented in three different configurations shown in Figure A3; the idea being that device-associated friction should increase when pulled through a highly tortuous sheath configuration, and the load cell used in testing should capture this increase.

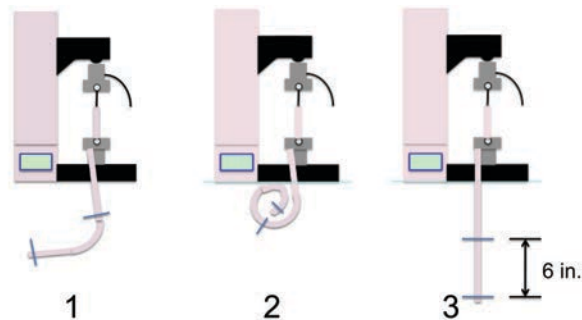


Figure A3: The configuration of the commercial microsheathe used in assessing the MTS extension tester load cell sensitivity. Configuration 1 allows for the device to be pulled through a single bend in the sheath. Configuration 2 allows for the device to be pulled through a highly tortuous sheath. Configuration 3 allows for the device to be pulled through a straight sheath. The device is pulled a total of six inches in all configurations.

Furthermore in each microsheath configuration shown in Figure A3 the flow diverting device was pulled at several different pulling speeds, ranging from 0.5 mm/s to 16 mm/s. Ultimately the pulling force was measured by the load cell for each microsheath configuration and pulling speed. The repeatability of the developed friction testing

methodology was assessed by dismantling each microsheath configuration, re-assembling it, and re-measuring the pulling force required to maintain each of the tested pulling speeds (n=3).

The force-extension data associated with pulling the #2 flow diverting device through a total of six inches (152.4 mm) in each of the three microsheath configurations at slow (0.5 mm/s), medium (4 mm/s), and fast (16 mm/s) speeds is shown as Figure A4.

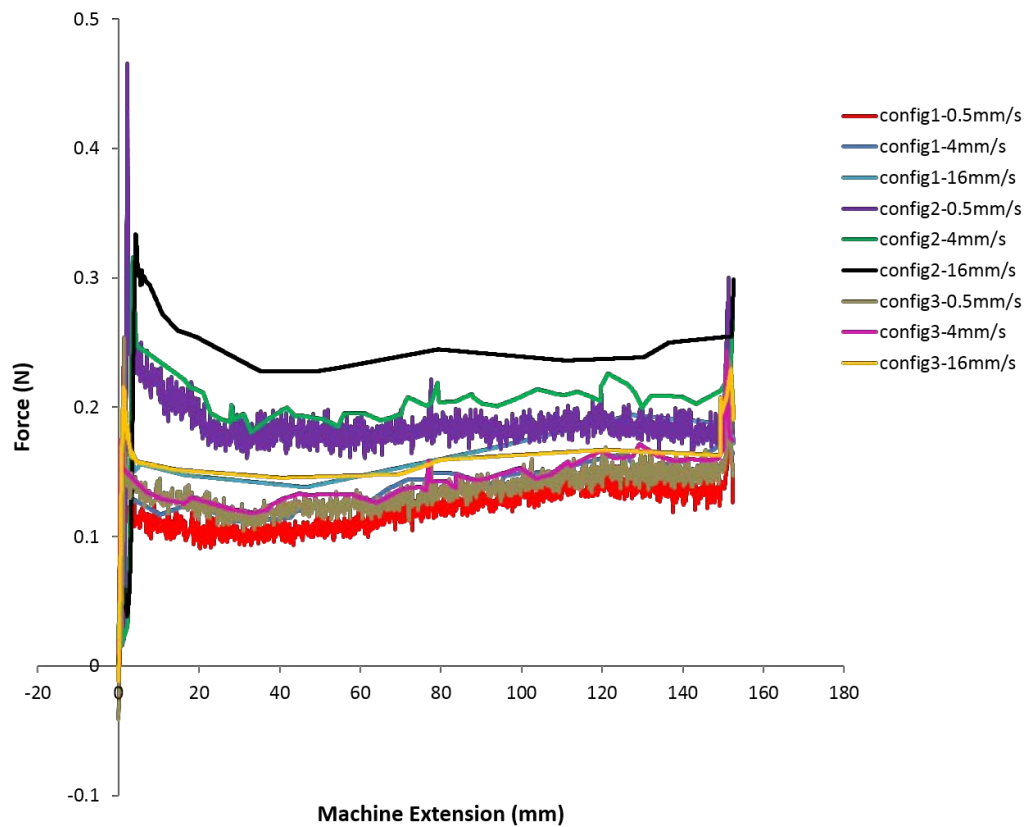


Figure A4: The force-machine extension data associated with pulling a commercial flow diverting device #2 through six inches of each of the three microsheath configurations shown in Figure A3. Data for pulling the device at slow (0.5 mm/s), medium (4 mm/s), and fast (16 mm/s) speeds is shown.

Figure A4 indicates that the extension tester load cell is able to resolve the increased device-associated friction brought about by moving through a highly tortuous microsheath configuration (or configuration 2 in Figure A3). As expected, the microsheath configuration with the single bend (configuration 1 in Figure A3) and the straight microsheath configuration (configuration 3 in Figure A3) offer less resistance to a moving device; thus, the pulling force required to maintain each pulling speed in these

configurations is less than the pulling force required for the highly tortuous configuration 2. Additionally, the pulling speed affects the measured pulling force. In all configurations, pulling the device at a slow speed requires less pulling force than pulling the device at the medium and fast speeds; pulling the device at slow speeds yielded high-frequency force-machine extension data in all configurations because the device slips against the microsheath at such low pulling speeds. Upon dismantling each microsheath configuration, re-assembling it, and re-measuring the pulling force required to maintain each of the tested pulling speeds (n=3), it was found that the pulling forces measured in each configuration were consistent between trials.